Experimental Aero-Acoustic Assessment of Swirling Flows for Drag Applications

by

Darius Darayes Mobed

B.S., Aerospace Engineering (2005)
Georgia Institute of Technology

Submitted to the Department of Aeronautics and Astronautics
in Partial Fulfillment of the Requirements for the Degree of

Master of Science in Aeronautics and Astronautics

at the

MASSACHUSETTS INSTITUTE OF TECHNOLOGY

February 2007

Signature of Author.....
Department of Aeronautics and Astronautics
January 19, 2007

Certified by.....
Zoltan S. Spakovszky
Associate Professor
Thesis Supervisor

Accepted by.....
Jaime Peraire
Professor of Aeronautics and Astronautics
Chair, Committee on Graduate Students

Experimental Aero-Acoustic Assessment of Swirling Flows for Drag Applications

by

Darius Darayes Mobed

Submitted to the Department of Aeronautics and Astronautics on January 19, 2007 in partial fulfillment of the requirements for the degree of Master of Science in Aeronautics and Astronautics

ABSTRACT

The need for quiet drag technologies stems from stricter requirements for and growing demand of low-noise aircraft. The research presented in this thesis regards the use of swirling exhaust flows capable of generating pressure drag quietly by establishing a steady streamwise vortex. The simple concept of a so called swirl tube, a ducted set of stationary turning vanes, was implemented to experimentally assess the aerodynamic and aero-acoustic behavior of swirling flows. A modular design was chosen for the model-scale wind-tunnel test article based on a full-scale diameter of 1.2 m to allow for the wind-tunnel testing of different swirl angles, including both stable swirling configurations and cases exhibiting vortex breakdown. Analyses of both aerodynamic and aero-acoustic test results indicate that highly swirling stable flows obtain maximum drag coefficients greater than 0.8 ±0.04 referenced to inlet area with full-scale overall sound pressure level (OASPL) of 42 dBA ±2 dBA, validating the working hypothesis that swirling flows can generate drag quietly. An advanced deconvolution approach for the mapping of acoustic sources (DAMAS), previously developed at the NASA Langley Research Center, was used to identify and to quantify quadrupole- and turbulent scattering-type noise sources in stable swirling flow cases, radiating from the downstream exhaust core and nacelle trailing edge regions, respectively. Cases exhibiting vortex breakdown, found to occur at swirl angle settings exceeding ~50°, demonstrated noise signatures 10 to 15 dB louder than the stable swirling flows, attributable to the increased scattering noise due to the turbulence of the burst vortex near swirl tube rear surfaces and edges. The practical integration of swirl tubes into aircraft design was assessed based on the conceptual silent aircraft design SAX-40. Integrating swirl vanes into the fan bypass or mixing ducts of aircraft engines is suggested to be capable of generating effective drag at minimal weight cost, benefiting from increased mass flow through the device due to fan pumping. The effects of non-uniform inlet flows on the generation of drag and noise were assessed experimentally and showed a reduction in drag by less than 17% with virtually no noise penalty. The experimental assessment of the swirl tube combined with theoretical engine and airframe integration studies suggest that swirling exhaust flows are capable of generating drag for quiet transport aircraft.

Thesis Supervisor: Zoltan S. Spakovszky
Title: Associate Professor

Acknowledgements

On the afternoon of the first day on-site at the Quiet Flow Facility of the NASA Langley Research Center, the first swirl tube shakedown test configuration was mounted in position over the air supply jet in the immense, silent anechoic chamber of the QFF. The tunnel air was turned on to full-speed, passing through the swirl tube with nothing more than a quiet "hiss". Standing at the open door of the chamber, the sight reminded me of a computer rendering of our device we cropped into an earlier image of the QFF months back to understand how the model might look when tested. Now, the picture was real—I could see it and, for the first time, I could *hear* it. The concept had been realized, and, for one of the first times, I felt like a true engineer. For that and all the help along the way, I have many to thank.

My greatest thanks go to my fellow members of the swirl tube team, Professor Zoltan Spakovszky and Dr. Parthiv Shah. I thank Professor Spakovszky for pairing me with this very special research effort, which has taught me more than any textbook or class. His guidance, leadership, and talent were key to both my success and the success of the project. The success of the project was also due to the impressive knowledge and thorough engineering know-how of Dr. Parthiv Shah. He provided technical aid and advice at almost every stage of the project, and for this I owe him great thanks. I learned immensely from these two gentlemen in many ways during our insightful conferences in Professor Spakovszky's office as well as our equally important late-night conferences at IHOP.

For his inspiration to use swirl, a special thanks is extended to Professor Jack Kerrebrock on behalf of the entire swirl tube team. Appreciation is also extended to Professor Edward Greitzer, Professor Mark Drela, and the students and faculty of the Silent Aircraft Initiative, who all provided constructive feedback throughout the swirl tube design process. Additional thanks go to Dr. Jim Hileman for his kind and patient aid as well as his always-helpful graduate student life advice.

Sincere gratitude goes out to all those involved in the fabrication of the swirl tube, including James Letendre, Dave Robertson, Todd Billings, and representatives at the MIT Central Machine Shop and Solid Concepts, Inc. A very special thanks is extended to Richard Perdichizzi for his great help with testing the swirl tube in the Wright Brothers Wind Tunnel.

The swirl tube research was funded by the NASA Langley Research Center, and I am grateful to Dr. Russell Thomas for his efforts as contract monitor. The swirl tube team had the extraordinary privilege of testing the swirl tube in one of the world's premier aero-acoustic test facilities, the Quiet Flow Facility, and our greatest appreciation goes to those involved in making the test a success. I learned much from the wisdom of Dr. Thomas Brooks accrued from years of experience in experimental acoustics, and thank him for the kind use of his impressive facility. Thanks are also extended to the staff of the QFF involved in the aero-acoustic testing, including Tony Humphreys, Dan Stead, Larry Becker, Dennis Kuchta, Jaye Moen, and, especially, Ronnie Geouge. Ronnie's extensive technical talents were critical to the success of the swirl tube tests at the QFF and his personality made every day at the QFF enjoyable. The month spent at the QFF was truly a dream-come-true for a graduate student like myself, though the experience left me never wanting to eat at McDonald's again.

I am thankful for the help, advice, and good times from everyone at the MIT Gas Turbine Lab. Thanks to Lori Martinez and Holly Anderson for their help with all the nitty-grtitty of life in the GTL. Very special thanks go out to fellow partner in crime, Barbara Botros (the sole Survivor), for always stopping by to discuss the latest TV gossip.

If I am to truly thank *all* those who helped me along the way, I must recognize the extraordinary work of the Boston and Allston Fire Departments and Boston Police. Five days prior to the thesis due date, my apartment building caught fire; the brave and amazingly fast efforts of these forces saved many things that morning, my latest thesis work being the least of my concern. To all those reading this thesis: please go home and check your smoke detectors.

I can't thank my family enough for all they've done for me over the years. Sincere thanks and love go to my parents and grandmother for their constant support and to my two sisters for keeping me (relatively) sane all the while.

I give my deepest thanks and love to Jamie. At times, I'd turn into a bit of a grad school monster, and you were always there to somehow provide the antidote. I thank you for helping make me who I am today and for teaching me more than I ever learned in school (no offense to my professors). For all you've done for me while I've been here, MIT should really print you a diploma, too. I love you, you know.

Table of Contents

Acknowledgments 5

List of Figures 11

List of Tables 19

Nomenclature 21

Chapter 1

Introduction

1.1 Background and Motivation 25

1.2 Swirling Flows as Quiet Drag Generators 26

1.2.1 Hypotheses 26

1.2.2 The Swirl Tube: A Simple Concept for Quiet Drag 27

1.2.3 Swirl Tube-Aircraft Integration Considerations 28

1.3 Research Questions and Objectives 28

1.4 Previous Work 29

1.5 Technical Roadmap 31

1.6 Outline of Thesis 33

Chapter 2

Wind Tunnel Facilities and Test Programs

2.1 Overview of Wind Tunnel Test Facilities 35

2.2 Swirl Tube Test Model Configurations 35

2.2.1 Standard Swirl Tube Configurations 36

2.2.2 Alternate Swirl Tube Configurations 36

2.2.3 Swirl Tube Configurations with Inlet Flow Non-Uniformity 37

2.3 Wright Brothers Wind Tunnel (WBWT) Facility Description and Test Program 38

2.3.1 WBWT Instrumentation 38

2.3.2 WBWT Data Reduction 41

2.3.2.1 Force Balance Data Reduction 41

2.3.2.2 Hotwire Data Reduction 42

2.3.3 WBWT Test Program 42

2.4 Quiet Flow Facility (QFF) Facility Description and Test Program 43

2.4.1 QFF Instrumentation 44

2.4.2 Post-Processing Technique for Phased Array (MADA) Data 46

2.4.3 QFF Test Program 50

2.5 Error Analysis of Measurements 50

2.5.1 Aerodynamic Measurement Error 51

2.5.2 Aero-Acoustic Measurement Error 53

Chapter 3

Mechanical Design of Wind-Tunnel Test Articles

3.1 Overview of Swirl Tube Mechanical Design 55

3.2 Swirl Vane Aerodynamic Design 56

3.3 Test Model Design Requirements 57

3.3.1 Model Versatility 57

3.3.2 Sizing 62

3.4 Part Fabrication 65

3.4.1 Material Selection and Fabrication Method of Visks 66
3.4.2 Material Selection and Fabrication Method of Nacelles, Center Bodies, and Pylons 66
3.5 Structural Integrity of Test Model 68
3.5.1 Forces and Moments 68
3.5.2 Critical Structural Locations with Stress Concentrations 70
3.5.2.1 Stress Analyses at Turning Vane-Shroud Junctions 72
3.5.2.2 Stress Analyses at Visk-Nacelle Joints 74
3.5.2.3 Stress Analyses at Pylon Tab 75
3.5.2.4 Stress Analyses at Pylon-Wall Junction 79
3.6 Boundary Layer Trip 82
3.7 Summary of Swirl Tube Mechanical Design 83

Chapter 4

Experimental Aerodynamic and Aero-Acoustic Assessment of Swirling Exhaust Flows

4.1 Overview of Swirling Flow Aerodynamics and Aero-Acoustics 85
4.2 Aerodynamic Assessment of Swirling Exhaust Flows 86
4.2.1 Characteristics of Stable Swirling Flows 86
4.2.2 Swirling Flow Stability Limit and Vortex Breakdown 89
4.3 Aero-Acoustic Assessment of Swirling Exhaust Flows 93
4.3.1 Trailing Edge Noise 95
4.3.2 Noise Mechanisms of Stable Swirling Flows 98
4.3.2.1 Scattering Noise from Turbulent Eddies at Nacelle Exit 100
4.3.2.2 Quadrupole-type Mixing Noise of Swirling Flows 104
4.3.3 Acoustic Signature of Swirling Flows with Vortex Breakdown 105
4.4 Outcomes of Swirling Flow Aerodynamic and Aero-Acoustic Assessment 106

Chapter 5

Aircraft Integration Considerations

5.1 Requirements for Aircraft Integration 109

5.2 Full-Scale Swirl Tube Drag and Acoustic Performance 110

5.2.1 Centerbody-Mounted Swirl Tubes 111

5.2.2 Winglet-Mounted Swirl Tubes 113

5.3 Swirl Tubes as Engine Air Brakes 115

5.3.1 Engine Air Brakes for SAX-40 Applications 115

5.3.2 Engine Air Brake Applications for Conventional Aircraft 118

5.4 Swirl Tube Performance with Upstream Flow Non-Uniformity 119

5.4.1 Inlet Distortion 119

5.4.2 Angle of Attack 121

5.5 Quiet Drag Solution 122

Chapter 6

Conclusions and Recommendations for Future Work

6.1 Summary and Conclusions 123

6.2 Recommendations for Future Work 124

Appendix A

Approximation of Turning Vane Load Distribution 127

Appendix B

Sizing of Fillet Radii for Local Stress Concentrations 129

Bibliography 131

List of Figures

1.1 Cambridge-MIT Silent Aircraft eXperimental design SAX-40, calculated to have a potential fuel burn of 125 passenger miles per gallon and an overall noise level of 63 dBA outside the airport perimeter [15]. 26

1.2 3-D computer rendering of swirl tube concept consisting of stationary turning vanes inside an aerodynamically contoured nacelle. 27

1.3 Pressure coefficient distributions for 47° (a) and 57° (b) swirl vane angle settings obtained from 2-D inviscid streamline curvature code. Steady 47° swirl case in (a) shows the radial pressure gradient and low-pressure central core. Unconverged 57° swirl case in (b) shows standing pressure waves on core line, indicative of vortex breakdown [29]. ...30

1.4 Mach number distributions for 47° (a) and 57° (b) swirl vane angle settings from full-scale 3-D RANS CFD [29]. Steady 47° swirl case shows the high velocities associated with the low-pressure central core; 57° swirl case shows vortex breakdown and separation bubble at nacelle exit, suggesting increased noise level due to scattering of turbulent flow structures at nearby nacelle surfaces and edges. 31

2.1 Alternate and distortion swirl tube configurations. 37

2.2 Schematic of MIT Wright Brothers Wind Tunnel (WBWT) facility. Test section is highlighted in red. Inset gives cross-sectional dimensions of the elliptic test section [18]. 39

2.3 Instrumentation setup for WBWT aerodynamic tests. Dual stepper motors on the traverse mechanism control the longitudinal and vertical positioning of the hotwire probe. 40

2.4 Streamwise and radial locations of steady and unsteady velocity measurements with hotwire probe. 41

2.5 Swirl tube aero-acoustic test setup in anechoic test chamber of QFF. Phased microphone array (MADA) shown in 107° forward angle position relative to swirl tube axis of symmetry....45

2.6 Instrumentation and wiring schematic for QFF acoustic data acquisition....46

2.7 B&K 4138 correction curves for various incidence angles. Since all array and pole microphones were pointed directly at swirl tube trailing edge, the 0° curve was used for all microphone corrections [6]....46

2.8 Computational "NASA" noise source location maps processed with standard beamforming (upper left) and DAMAS techniques of various iterations [3]....48

2.9 Standard array beamforming (a) and DAMAS-processed (b) one-third octave noise source maps of 47° swirl case at 16 kHz with $M = 0.17$. While standard beamforming correctly highlights the general region of noise sources, the DAMAS-processed result clearly shows distinct noise sources at the nacelle trailing edge and downstream....49

2.10 Drag coefficient versus swirl vane angle setting taken in March 2006 (blue) and August 2006 (red). Experimental error in drag coefficient, taken from the largest discrepancy of the repeated measurements, is 0.032....52

2.11 Conversion of hotwire-measured voltage to velocity by calibration. Four (overlapping) curves represent hotwire calibrations from four separate test days. Experimental error of measured voltages, taken from the largest discrepancy of hotwire calibrations, is 0.017 mV....53

2.12 Comparisons of experimentally-measured narrowband (17.45 Hz) microphone autospectra for 47° swirl case taken at free stream Mach numbers of 0.11 and 0.17 on two different test days. Experimental error of noise results, taken from the largest discrepancy in OASPL of repeated measurements, is 0.52 dBA....54

3.1 Airfoil sections stacked to generate a 3-D vane design. Turning angle varies from zero at the vane hub to higher angles at the vane tip according to the circulation distribution of a Burger vortex. Figure adopted from [29]....56

3.2 Exploded view of swirl tube test model assembly. The six components of the modular assembly are depicted with the central visk in blue. Renderings of pylon and nacelle mechanical fasteners are also included....59

3.3 Nacelle and center body cross sectional profiles. Nacelle contour is a cambered airfoil constructed with a 3-to-1 leading edge semi-ellipse and semi-circular trailing edge. Flow area ratio relative to nacelle exit, shown by red dashed line, is close to unity at all locations downstream of vanes (actuator disk) to prevent unnecessary acceleration/ deceleration of exit flow [29]....59

3.4 Nine visks used in the experimental testing of the swirl tube. Visual differences between low swirl cases (i.e. 34°, 41°) and high swirl cases (i.e. 57°, 64°) are most apparent at vane hubs. 60

3.5 Estimated and experimentally measured noise signatures of nacelle, NACA 0022 pylon, and NACA 0012 profiles [5] presented in one-third octave bandwidth. Pylon and nacelle spectra peaks are distinct in terms of peak frequency and amplitude, suggesting pylon noise will not mask the experimentally measured noise signatures of the empty nacelle and swirl cases. 62

3.6 Swirl tube position relative to estimated QFF free jet potential core. Zone of considerate streamline displacement perpendicular to undisturbed tunnel flow direction is contained fully within potential core given a 20.3 cm (8.0 in) swirl tube maximum diameter, suggesting most of the swirl tube spilled flow will not coincide with the free jet shear layer. 63

3.7 Computed spectra of nacelle profiles of various chord lengths relative to QFF background noise. Good signal-to-noise for swirling cases is assumed for nacelle chords between 15.24 cm (6 in) and 29.2 cm (11.5 in) in length since these cases yield spectral peaks above background noise level. 64

3.8 Dimensioned three-view layout of swirl tube test model. Primary dimensions are given in centimeters outside parenthesis with inch equivalents inside parenthesis. 65

3.9 Nacelle, centerbody, support pylons, and accessory swirl tube equipment. Parts shown are fabricated from aluminum alloy T6061 via CNC lathe, CNC mill, or conventional metal machining methods. 67

3.10 Loading diagrams and reaction forces and moments for the swirl tube mounted in QFF (top left and right) and WBWT (bottom left and right). Pylon drag, negligible in both cases, is not included in the figures. 70

3.11 Normalized radial loading distribution (blue) and constant loading distribution (red) on a single swirl vane. Swirl moment, M_S, is calculated using the constant loading distribution (red) for simplicity. 70

3.12 Subdivision of loads on a statically indeterminate turning vane (a) through the method of superposition of cantilevered beams with (b) a distributed load, (c) a tip load, and (d) a tip moment. Solutions to the three cantilevered cases sum to represent that of the original clamped-clamped case (a) by setting the sum of tip deflections for cases (b), (c), and (d) equal to zero. 72

3.13 Turning vane hub fillet geometry. Increasing the fillet radius further would significantly reduce the flow area of the vane passages at the hub, thus limiting the vane hub stress concentration safety factor to 1.5. 74

3.14 Shear and compression forces acting at forward nacelle-visk lap joint.....75

3.15 Aerodynamic and structural loads contributing to reaction moments and shear forces at pylon tab.....75

3.16 3-D view of bending moments and shear forces acting on pylon tab. Moments M_y and M_z along with shear force V_y stress the pylon tab as both a beam-like and plate-like structure.....76

3.17 Dimensioned cross section of pylon tab. Centroid is located at axis origin. Primary dimensions are given in centimeters outside parenthesis with inch equivalents inside parenthesis.....77

3.18 Mohr's circle for pylon tab stresses. Total bending stress, σ_x, and maximum shear stress, τ_{xy}, are used to construct the circle, from which the principle stresses σ_1, and σ_2 are found.....78

3.19 Shear and compression forces acting on pylon tab screw. Because screw passes through pylon tab completely, shearing occurs at two locations (pylon-pylon tab interfaces).....79

3.20 Swirl tube load diagrams for QFF test with pylon-wall junction reaction forces and moments. Moment M_{xo}, not shown, is equal to zero since there is no applied moment in the x-direction to counteract.....80

3.21 Bending moment (dark blue) and shear force (magenta) diagram for QFF pylon in bending. Maximum bending moment occurs at $x = 0$ cm, indicating the cross section at the pylon-wall junction contains the point of maximum bending stress.....80

3.22 Dimensioned cross section of QFF pylon. Centroid is located at axis origin. Primary dimensions are given in centimeters outside parenthesis with inch equivalents inside parenthesis. Locations of pylon tab and pylon tab screws are indicated by green and light blue boxes, respectively.....81

3.23 Mohr's circle for QFF pylon stresses. Total bending stress, σ_x, and maximum shear stress, τ_{xy}, are used to construct the circle, from which the principle stresses σ_1, and σ_2 are found.....82

4.1 Full-scale (D = 1.2 m) drag coefficient and OASPL for swirling flows of various swirl vane angle settings. Stable swirling flows (white background) are capable of generating drag coefficients over 0.8 ±0.04 at full scale OASPL less than 42 dBA ± 2 dBA. For swirl angles exceeding ~50° (gray box), breakdown of the steady vortex causes drag generation to decrease while scattering noise from turbulent eddies of the burst vortex structure near sharp nacelle edges leads to a distinct increase in noise level.....86

4.2 Axial velocity, tangential velocity, and swirl angle radial profiles for 34° swirl case at various locations downstream of nacelle exit. Good agreement is observed between

experimental measurements and CFD predictions while slight overturning in experimental data suggests higher drag levels compared to CFD [29]. 87

4.3 Smoke visualization of swirling exhaust flows for various swirl angle settings with sketches of helical wavelengths. Swirl cases less than or equal to 47° each show a stable streamwise vortex with a clear, low-pressure, high-velocity axial core, which generates pressure drag. Smoke visualization of swirl cases greater than or equal to 53° show a turbulent separation bubble on the core close to the nacelle exit associated with the vortex breakdown. 90

4.4 Power spectral density of unsteady axial (z) and circumferential (θ) velocities for (a) stable 47° swirl case and (b) 57° swirl case exhibiting vortex breakdown measured on centerline at downstream location $z/D = 0.5$. Collapse of broadband spectra for 57° swirl case indicates separation bubble characteristic of vortex breakdown. 91

4.5 Axial velocity, tangential velocity, and swirl angle radial profiles for 47° and 57° swirl cases at $z/D = 1.0$ downstream of nacelle exit. Radial profiles of 57° case indicate presence of turbulent bubble of burst vortex with diameter roughly equal to nacelle exit diameter. 92

4.6 Axial velocity profiles for 34° swirl case at various z/D locations downstream of nacelle exit. Swirl tube exhaust flow mixes out as it moves downstream, approaching a uniform distribution equal to free stream velocity. 93

4.7 Narrowband (17.44 Hz) autospectra of standard swirl tube configurations. Three distinctly different groups of noise-generating configurations are seen: (1) trailing-edge noise-dominated non-swirl cases, (2) stable swirling cases, and (3) swirling cases exhibiting vortex breakdown. 94

4.8 Noise spectra of pylon with and without trailing-edge serration. Trailing edge serration 1.27 cm (0.5 in) in length attenuates trailing edge noise spectrum by as much as ~3 dB/St 96

4.9 Scaled one-third octave noise spectra of (a) nacelle trailing edge and (b) pylon regions of empty nacelle configuration (magenta diamonds). For comparison, noise signatures of NACA 0012 (a) 30.48-cm-chord airfoil (12 in, approximate nacelle chord) and (b) 10.16-cm-chord airfoil (4 in, approximate pylon chord) are presented from Brooks et al. [5]... 97

4.10 DAMAS noise source mapping of empty nacelle and pylon configuration shown for the 4 kHz one-third octave band. Central black solid lines indicate position of swirl tube and support pylon (horizontal lines to the right of the pylon). Noise sources are clearly distributed at nacelle and pylon trailing edges. Each grid box is 2.54 cm x 2.54 cm (1 in x 1 in) 97

4.11 DAMAS noise source mapping of (a) 34°, (b) 41°, and (c) 47° stable swirl configurations shown for the 20 kHz one-third-octave band. Dominant noise source in all cases is

turbulent scattering noise at nacelle exit. Noise level of downstream quadrupole source approaches that of the turbulent scattering source as swirl angle increases and the low-pressure core strengthens. Each grid box is 2.54 cm x 2.54 cm (1 in x 1 in).....100

4.12 Lower aft region DAMAS noise source integrated one-third octave spectra of 47° stable swirl configuration at various free stream Mach numbers (a) without and (b) with Mach number scaling. Collapse of data in (b) using n = 5 indicates turbulent scattering. Integration region depicted by orange box in map inset. 102

4.13 Nacelle exit region integrated one-third octave spectra of 0°, 34°, 41°, and 47° stable swirl configurations at free stream M = 0.17 (a) without and (b) with core Mach number scaling with n = 5. Collapse of data in (b) using core Mach numbers suggests spectral peaks are related to swirl angle via nacelle exit velocities. Source noise integration region depicted by orange box in map inset.....103

4.14 Free field source integrated one-third octave spectra of 47° stable swirl configuration at various free stream Mach numbers (a) without and (b) with Mach number scaling. Collapse of data in (b) using n = 8 indicates quadrupole-type mixing noise. Source integration region depicted by orange box in map inset.....104

4.15 DAMAS noise source mapping of (a) 53°, (b) 57°, and (c) 64° swirl configurations with vortex breakdown shown for the 20 kHz one-third-octave band. Dominant noise source in all cases is burst vortex turbulence and quadrupole scattering noise radiating efficiently as a compact source at the nacelle exit. Each grid box is 2.54 cm x 2.54 cm (1 in x 1 in). 105

4.16 Aft region DAMAS noise source integrated one-third octave spectra of 57° swirl configuration with vortex breakdown at various Mach numbers (a) without and (b) with Mach number scaling. Collapse of data in (b) using n = 7.5 suggests presence of scattering and open-flow quadrupole-type noise mechanisms. Source integration region depicted by orange lines in map inset. 106

5.1 Three-view layout of SAX-40 with six centerbody-mounted swirl tubes (green). In top view (b), additional ducting for inlet and exhaust streams are shown as dashed red lines. Actuated inlet doors and split trailing edge doors for ducting are shown in (a). As seen in (c), fuel tank placement and decreasing wing thickness limit the size and number of swirl tubes for the configuration. Figure adopted from [15].....112

5.2 Front-view of SAX-40 with winglet-mounted swirl tubes of various diameter (green). Circumferences were approximated by "rolling" the length of the existing 4.01 m (13.16 ft) winglets.....113

5.3 Aviation Partners Gulfstream II test aircraft with looped "spiroid" winglets. Flight testing of spiroid winglets showed a 10 percent reduction in cruise fuel consumption, achieved by eliminating concentrated wingtip vortices responsible for nearly half of the induced drag experienced in cruise [12].....114

5.4 Axial Mach numbers for (a) ram pressure driven and (b) fan-stage pumped 47° swirl cases. Pumped case assumes upstream fan pressure ratio of 1.08. Pumping doubles maximum core Mach number, increasing both drag and noise generation [29]. 116

5.5 Concept drawings of swirl vanes deployed aft of turbofan engine in (a) swirl mode and (b) thrust reverser mode. In thrust reverser mode, exhaust doors open in nacelle to expel flow radially [29].....117

5.6 Measured drag coefficient of swirl tube with 47° vanes with various inlet distortions. Under the most significant inlet distortion, the 120° solid plate, the swirl tube is still capable of generating a drag coefficient of ~0.7. 120

5.7 Narrowband (17.44 Hz) noise spectra of swirl tube with 47° vanes and various inlet distortions. Overall, baseline case is relatively unaltered by inlet distortion. Strong edge tone in 120° screen case is due to sharp plate hole edges. 121

5.8 Narrowband (17.44 Hz) noise spectra of swirl tube with 47° vanes at small angles of attack. Small angles of attack have little influence on the noise spectrum. 122

A.1 Loading on an infinitesimal element of a turning vane at distance r from the swirl tube axis of symmetry. Loading is caused by the change in angular momentum of flow through the vane passages due to turning.....128

B.1 Definition of geometric parameters used in empirical estimation of fillet sizing for local stress concentrations. Note: figure is not to scale. 129

List of Tables

1.1 Full-scale drag coefficient for 2-D MTFlow and 3-D CFD computations for various swirl vane angle settings, α. Drag coefficients from 3-D CFD computations are decomposed into pressure and viscous drag components (adopted from [29]). 31

2.1 Swirl tube aerodynamic test program for MIT WBWT experiments. All configurations except those indicated with * include boundary layer trips on nacelle and vanes. 44

2.2 Summary of swirl tube aerodynamic and aero-acoustic error. All quantified measurement errors are less than 10% of reference measurements. 51

3.1 Drag coefficients referenced to inlet area estimated by 2-D inviscid streamline curvature calculations for various maximum turning vane angles [29]. See Table 1.1 for 3-D CFD drag estimates 57

3.2 Material properties of various swirl tube components 66

3.3 Fillet radii, nominal stresses, and safety factors of critical structural locations. Minimum QFF-required safety factor of 4.0 is met at all critical structural locations with the exception of turning vane hubs. Nominal stresses at all critical locations are well below material yield stresses. 71

4.1 Experimentally measured and CFD predicted model-scale and full-scale swirl tube drag coefficients for various swirl angles. 88

4.2 Scaling powers of various noise mechanisms based theories by Lighthill and Ffowcs Williams and Hall [9, 17, 20]. 101

4.3 Maximum core velocities normalized to free stream of non-swirl and stable swirl configurations. 103

5.1 Calculated full-scale swirl tube properties for various SAX-40 integration configurations. For each parameter (row), best value is indicated in green; worst value is indicated in red.

The propulsion system-integrated configurations are favored for their high drag to weight ratio.....111

5.2 Full-scale winglet swirl tube skin friction drag counts for SAX-40 cruise conditions. Data in last column presents estimated cruise skin friction of swirl tube nacelle and 20 straight vanes above that generated by the 4.01 m (13.16 ft) winglet, approximately 1.22 counts. All drag counts are shown for two devices, one on each wing tip.....115

5.3 Reduction of approach noise for various civil aircraft due to integration of engine-scale ram-air swirl tubes and/or engine air brakes. Results indicate approach noise level reductions of 2+ dB and 6+ dB, respectively, for these two integration methods [28]...119

Nomenclature

Roman

A	Area
$\hat{A}$	DAMAS matrix of beamforming characteristics
c	Chord length, speed of sound
C_D	Drag coefficient
C_f	Skin friction coefficient
C_p	Pressure coefficient
D	Diameter; Drag
$\overline{D}$	Directivity factor
e	Error
$\hat{e}$	Matrix of steering vectors
E	Voltage; Young's modulus
f	Frequency
F	Force
F_S	Inlet suction force
$\hat{G}$	Cross-spectral matrix
I	Moment of inertia, acoustic intensity
k	Wave number
K	Stress concentration factor
L	Length

$\dot{m}$	Mass flow rate
m_0	Number of array microphones
M	Mach number, moment
M_S	Swirl moment
n	Scaling power
N	Number of swirl vanes; number of test Mach numbers
p	Pressure
q	Distributed load, dynamic pressure
Q	First moment of area
r	Radial coordinate
R	Radius
Re	Reynolds number
St	Strouhal number
t	Thickness, time
T_{ij}	Lighthill's stress tensor
v	Velocity
$\boldsymbol{v}$	Total velocity
$\overline{v}$	Mean velocity
v'	Velocity perturbation
V	Shear force
W	Weight
$\hat{X}$	Noise source matrix
$\hat{Y}$	DAMAS output acoustic power response
z	Axial coordinate

Greek

α	Swirl angle
δ	Deflection, radius of turbulent eddy, thickness
λ	Wavelength, noise propagation distance
ν	Kinematic viscosity

ρ	Density
σ	Axial coordinate
τ	Noise source matrix

Subscripts

∞	Free stream value
0	Root
act	Actual
BL	Boundary layer
c/s	Cross section
comp	Compression
D	Drag
D,press	Pressure drag
D,visc	Viscous drag
FN	Forward nacelle
Full	Full scale
max	Maximum
model	Model scale
n	Nacelle
PL	Plate
PT	Pylon tab
py	Pylon
θ	Tangential
ref	Reference
rms	Root mean square
RN	Rear nacelle

	Reaction
rxn	
	Swirl tube
st	
	Axial
z	

Acronyms

AoA	Angle of attack
B&K	Brüel and Kjær
BM	Bending moment
CAD	Computer aided design
CFD	Computational fluid dynamics
CNC	Computer numeric controlled
DAMAS	Deconvolution approach for the mapping of acoustic sources
DAQ	Data acquisition unit
MADA	Medium aperture directional array
OASPL	Overall sound pressure level
QFF	Quiet flow facility
RANS	Reynolds-averaged Navier Stokes
SAX	Silent aircraft eXperimental
SF	Safety factor; shear force
SLA	Stereolithography apparatus
SPL	Sound pressure level
WBWT	Wright brothers wind tunnel

Chapter 1

Introduction

1.1 Background and Motivation

Noise reduction is becoming increasingly important to modern aircraft design. Quiet aircraft provide increased revenue opportunities to airlines from night operations with the ability to meet stricter noise ordinances typically imposed at urban airports during night hours. Airport noise restrictions are becoming more popular to promote the development of areas surrounding airport properties and enhance real-estate values, further driving aircraft design to include noise-reduction efforts.

From an operational perspective, aircraft noise, as perceived by a ground observer, is dictated by the distance between the aircraft (source) and observer as well as the velocity at which the aircraft is flying. Approach noise propagated to the ground, for example, can be attenuated significantly by flying slower and steeper approach profiles to reduce the airframe source noise and to increase the source-observer distance. In this, quiet drag devices are key enablers to flying such approach paths.

Current aircraft employ drag devices such as flaps, slats, and spoilers that have a strong correlation between drag and noise. Wakes shed from these devices generate fluctuating forces, giving rise to both drag as well as noise in the form of acoustic dipoles. To meet the noise reduction goals, future quiet aircraft will see an even greater need for high-drag, low-noise devices for approach. One such aircraft, the Silent Aircraft[1] eXperimental design SAX-40 shown in Figure 1.1 uses an all-lifting airframe to eliminate the need for trailing edge flaps [15]. Though the airframe provides sufficient lift capabilities, a quiet drag solution is needed to fly a slow and steep approach path. Thus for both current and future aircraft applications, it is the

[1] The term "silent" is defined here as being no louder than the background noise observed in a well-populated area.

goal of this thesis to assess one such quiet drag concept: the generation of quiet drag from swirling exhaust flows.

Figure 1.1. Cambridge-MIT Silent Aircraft eXperimental design SAX-40, calculated to have a potential fuel burn of 125 passenger miles per gallon and an overall noise level of 63 dBA outside the airport perimeter [15].

1.2 Swirling Flows as Quiet Drag Generators

Swirling flows are involved in numerous aerospace applications, including combustion chamber mixing in aircraft engines and turbomachinery duct aerodynamics [13]. Exploiting swirling flows for quiet drag applications, however, is a novel concept. Section 1.2.1 presents the hypotheses associated with generating quiet drag from ducted streamwise swirling flows while Section 1.2.2 describes a simple device concept with which the hypotheses can be experimentally validated. Finally, Section 1.2.3 extends the simple device concept and assesses practical aircraft integration issues.

1.2.1 Hypotheses

The essence of obtaining quiet drag from a steady swirling exhaust flow derives from the characteristic streamwise vortex that is supported by a radial pressure gradient. For the purpose of this discussion, a simplified situation is that of a swirling flow in simple radial equilibrium [13]. In this case, the radial pressure gradient is balanced by the centripetal acceleration of the swirling fluid particles such that

$$\frac{\partial p}{\partial r} = \frac{\rho u_\theta^2}{r}. \tag{1.1}$$

Since the boundary condition at the outer radius of the exhaust duct requires the local pressure to equal atmospheric pressure, the core region of the vortex is at sub-atmospheric pressures. With this, a net axial pressure differential across the device is created, which gives rise to a pressure drag force. A key hypothesis is that the generation of pressure drag is relatively quiet provided the streamwise vortex is steady. Since unsteady flow structures, such as those prevalent in turbulent boundary layers or turbulent mixing of flow streams, are typically noisy it is postulated that steady swirling flows are a quiet means of producing pressure drag.

The working hypothesis is that the noise mechanisms of steady swirling flows are comprised of a dominant scattering noise source caused by turbulent flow structures at device edges and a weaker quadrupole-type source radiating in the open field. It is also hypothesized that there exists an upper stability limit for swirling flows at which point the steady streamwise vortex bursts. This transition to vortex breakdown is detrimental to the formation of the low-pressure core region, leading to a decreased capacity to generate drag. The additional scattering noise of the turbulence associated with the vortex burst is expected to increase the noise levels over quieter, steady swirling flows. Thus it is hypothesized that the upper stability limit for swirl also limits both drag generation and noise reduction.

1.2.2 The Swirl Tube: A Simple Concept for Quiet Drag

To experimentally assess the hypotheses presented in the previous subsection, a device must be conceived that can convert free stream, axial flow to swirling exhaust flow. The simplest concept is a duct with stationary turning vanes, from here on defined as a "swirl tube". Shown in Figure 1.2, the swirl tube contains turning vanes attached at their roots to an aerodynamically shaped centerbody and attached at their tips to an outer shroud. The experimental assessments described in the following chapters employ variations of the simple swirl tube concept to characterize the drag generation capabilities and noise mechanisms in dependent of swirl angle and inflow non-uniformity.

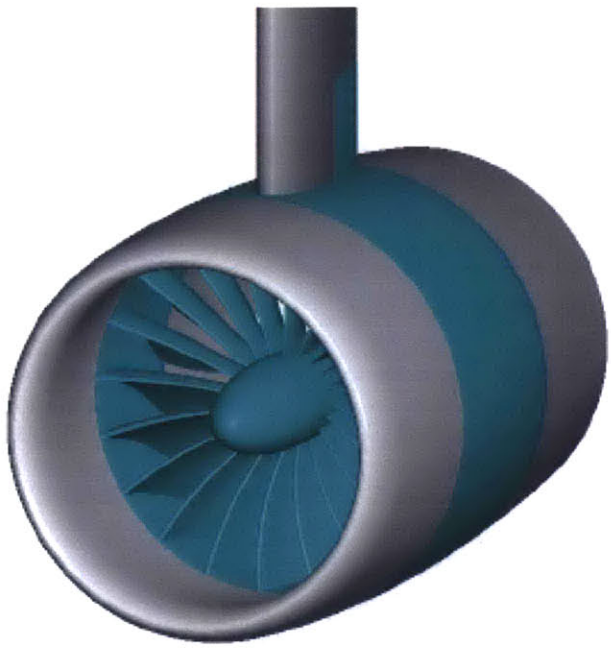

Figure 1.2. 3-D computer rendering of swirl tube concept consisting of stationary turning vanes inside an aerodynamically contoured nacelle.

1.2.3 Swirl Tube-Aircraft Integration Considerations

One of the objectives of the research presented in this thesis is to investigate concepts that are conceived from the experimental assessment of swirling exhaust flows and potentially installable in real-world aircraft as a solution for quiet drag. Given that the streamwise swirling flows under considerations are axisymmetric, it is postulated that practical installations of devices capable of generating such flows would be most appropriate in axisymmetric structural members of an aircraft, such as an engine nacelle or other internal or external ducting. Assessed in detail in Chapter 5, aircraft integration of a quiet drag device such as the swirl tube presents a number of engineering challenges, including design, installation, and performance considerations.

1.3 Research Questions and Objectives

The following research questions and objectives are addressed in this thesis in the light of the hypotheses presented in Section 1.2.1:

- Does swirling exhaust flow present a high-drag, low-noise solution for aeronautical applications? If so, what are the relationships between swirl angle, drag generation, and noise?

- For what swirl vane angle setting does the swirling exhaust flow become unstable and exhibit vortex breakdown? When this limit is exceeded, how does the exhaust flow field change and what are the corresponding repercussions in terms of drag and noise generation?

- What is the acoustic signature of swirling exhaust flows? What are the underlying noise mechanisms and how are these altered for vortex breakdown?

- Is the swirl tube a practical quiet drag device for current and future aircraft? What are the technological barriers and potential installation concerns?

To address these research questions, a series of aerodynamic and aero-acoustic wind tunnel experiments, outlined in Section 1.5 and described in detail in Chapter 2 were carried out. These experiments carried the following test objectives in order to fully assess the aerodynamic and aero-acoustic capabilities of the swirl tube:

- To demonstrate a maximum drag coefficient of 0.8 from stable swirling exhaust flow,

- To validate that steady swirling flow is quiet (well below the background noise of a well-populated area),

- To identify the swirl stability limit that is the condition under which a stable swirling flow transitions to vortex breakdown,

- To identify and quantify the noise mechanisms governing the acoustics of both steady swirling and flows with vortex breakdown,

- To assess the aerodynamic and aero-acoustic effects of upstream flow non-uniformities on swirl tube drag performance and noise signature.

1.4 Previous Work

Research by Shah [29] details the aerodynamic turning vane design and computational assessment of the swirl tube as a quiet drag device. An overview of his procedures and results is presented in this section to provide a background to CFD-predicted swirling flow aerodynamics from the given swirl tube design used in the series of wind tunnel experiments conducted in the present research.

The goal of the aerodynamic performance of the swirl tube was to achieve a drag coefficient of 1.0 based on inlet flow area for steady swirling flow without vortex breakdown. A variety of swirl vanes of different swirl angle settings were thus designed using a Burger vortex distribution [13] model with this drag target in mind [29]. First, turning vane angles, drag coefficient, and upper swirl stability limit were estimated using a 2-D inviscid streamline curvature code developed by Drela [8] for swirl vane angle settings of ~50°. Empirical methods were then used to determine appropriate vane solidity, defined as vane chord divided by vane spacing. Solidities of 3 at the vane tips to 4 at the vane hubs were chosen to reduce profile losses and vane loadings such that proper flow turning is ensured throughout the vane passages. Though the solidity is higher at the hubs due to the close spacing of vanes near the center of the swirl tube, it is kept to a reasonable value by shortening the chord length of the vanes at the hub. This, coupled with the radial distribution of tangential velocity, places the greatest need for flow turning at the vane tips. To accommodate high flow turning at outer radii, the vane designs are twisted to vary local turning vane angle from 0° at the hub to a given maximum turning angle at the tip. It is this maximum turning angle at the tip that is used in this thesis to define the swirl vane angle setting for a given configuration. As a basis for a parametric study including both stable swirling and vortex breakdown cases, swirl vane angle settings of 34°, 41°, 47°, 53°, 57°, and 64° were used to estimate drag coefficients of 0.4, 0.6, 0.8, 1.0, 1.1, and 1.31, respectively, using steady 3-D RANS CFD simulations. More on the vane design methodologies can be found in Chapter 3 and [29].

High fidelity computational results [29] corroborate the findings discussed above, suggesting that the transition to vortex breakdown occurs between swirl angle settings of 47° and 57°. Figure 1.3 shows pressure coefficient distributions for (a) the stable 47° swirl case, and (b) the 57° swirl case with vortex breakdown. The radial pressure gradient for stable swirling flows is clear in the pressure contours of Figure 1.3a while the standing pressure waves on the core shown in Figure 1.3b suggest the streamwise vortex has reached critical state. This critical state presents the opportunity for downstream perturbations to propagate upstream, leading to vortex breakdown. A more detailed discussion can be found in [29]. Thus the estimated upper swirl stability limit near ~50° suggests that the full-scale drag coefficient of 0.8 estimated for 47° swirl case is a

good approximation for the maximum drag coefficient attainable from steady swirling exhaust flows.

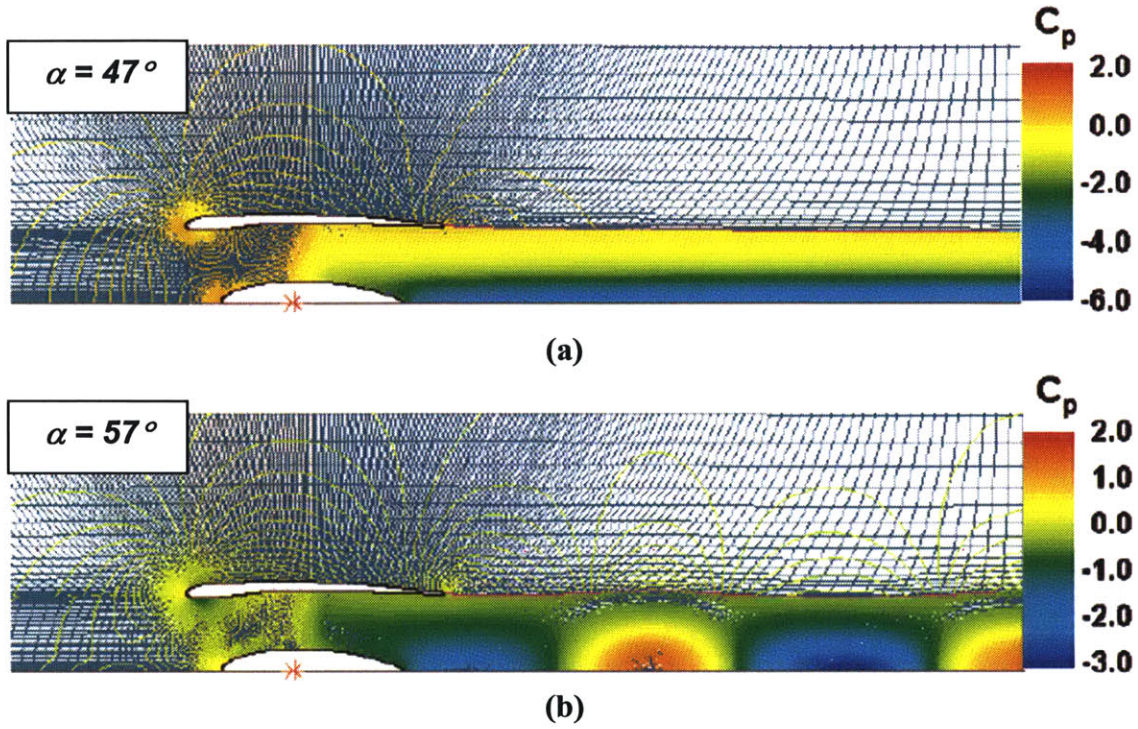

Figure 1.3. Pressure coefficient distributions for 47° (a) and 57° (b) swirl vane angle settings obtained from 2-D inviscid streamline curvature code. Steady 47° swirl case in (a) shows the radial pressure gradient and low-pressure central core. Unconverged 57° swirl case in (b) shows standing pressure waves on core line, indicative of vortex breakdown [29].

The axial Mach number distributions of Figure 1.4 from 3-D CFD again compare the exit flow fields of (a) the stable 47° swirl case, and (b) the 57° swirl case with vortex breakdown. The high velocities associated with the low-pressure core region are evident in Figure 1.4a. Figure 1.4b clearly shows the turbulent separation bubble of the burst vortex near the swirl tube nacelle exit. The proximity of this turbulent bubble to swirl tube rear nacelle surfaces and edges suggests increased scattering noise of turbulent flow structures associated with vortex breakdown.

Table 1.1 adopted from Shah [29] lists drag coefficients predicted by 2-D MTFlow and 3-D CFD computations for 34°, 47°, 53°, 57°, and 64° swirl vane angle setting cases. Though maximum CFD-predicted drag coefficients are shown to be close to 1.00 for the 57° and 64° swirl vane angle settings, it should be noted that these steady CFD results lack computational convergence due to the unsteady nature of the vortex breakdown phenomenon. Without experimental validation, it is uncertain whether highly swirling cases with vortex breakdown will continue to generate increased levels of drag or if the vortex breakdown is detrimental to drag generation. The key outcome of these results, however, is that a maximum full-scale drag coefficient of 0.84,

dominated by its pressure drag component, is achievable from stable swirl cases, validating the drag generating capabilities of this particular swirl tube design as a potential quiet drag solution.

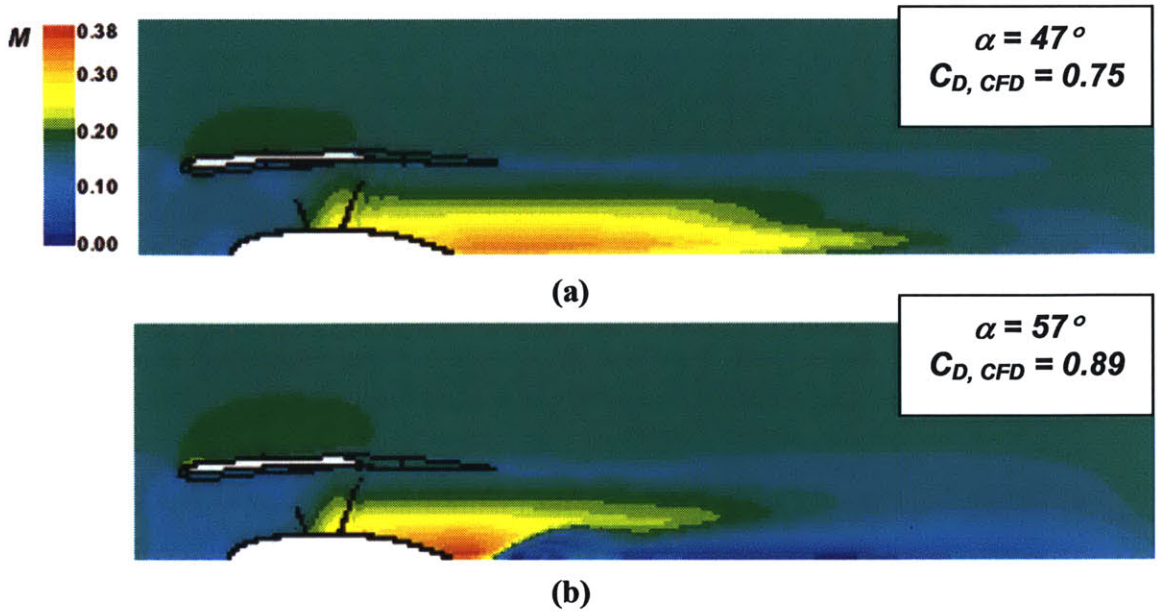

Figure 1.4. Mach number distributions for 47° (a) and 57° (b) swirl vane angle settings from full-scale 3-D RANS CFD [29]. Steady 47° swirl case shows the high velocities associated with the low-pressure central core; 57° swirl case shows vortex breakdown and separation bubble at nacelle exit, suggesting increased noise level due to scattering of turbulent flow structures at nearby nacelle surfaces and edges.

	MTFLOW	CFD				
α_{max}	C_D	C_D	$C_{D,\text{ press.}}$	$C_{D,\text{ visc.}}$	Vortex Breakdown	Convergence
34°	**0.40**	**0.39**	0.32	0.07	No	Yes
47°	**0.80**	**0.75**	0.68	0.07	No	Yes
53°	**1.00**	**0.84**	0.77	0.07	No	Yes
57°	**1.10**	**0.89**	0.82	0.07	Yes	No
64°	**1.31**	**0.94**	0.88	0.06	Yes	No

Table 1.1. Full-scale drag coefficient for 2-D MTFlow and 3-D CFD computations for various swirl vane angle settings, α. Drag coefficients from 3-D CFD computations are decomposed into pressure and viscous drag components (adopted from [29]).

1.5 Technical Roadmap

The following steps outline the technical approach used to answer the research questions posed in Section 1.3 through aero-acoustic wind tunnel experiments and post-test analyses of swirl tube performance for quiet drag applications.

1. Design of Test Equipment. Test articles were designed in accordance with Shah's computational swirl tube design and requirements of the wind-tunnel testing facilities. The $1/7^{th}$ scale[2] swirl tube models utilized modular designs to easily convert between test configurations of different swirl vane angle settings. Analysis of maximum loading conditions guided the design of key structural members of the model to ensure zero risk of structural failure during wind tunnel testing.

2. Aerodynamic Wind-Tunnel Testing. Wind tunnel testing of the swirl tube at the Wright Brothers Wind Tunnel (WBWT) at MIT provided an experimental assessment of swirl tube aerodynamics. Drag measurements were conducted for various swirl configurations to quantify the relationship between swirl vane angle settings and drag. Flow visualization techniques and wake traverses were employed to qualitatively and quantitatively examine the structures of swirling flows, including the transition from stable swirling flows to vortex breakdown. Special configurations introducing various upstream non-uniformities to the swirl tube were used to capture the aerodynamic effects of inlet flow non-uniformities on swirl tube performance.

3. Aero-acoustic Wind-Tunnel Testing. Open jet testing of the swirl tube at the Quiet Flow Facility (QFF) at the NASA Langley Research Center provided an experimental assessment of the swirl tube aero-acoustic behavior. Single microphone and array-based acoustic measurements were taken for swirl tube configurations at various Mach numbers to quantify the relationship between swirl vane angle setting and radiated noise levels. This, coupled with the drag assessments from the aerodynamic wind tunnel tests, provided a first means of identifying the plausibility of a high-drag, low-noise configuration of the swirl tube. Array-based measurements and a sophisticated post-processing technique developed by Brooks and Humphreys [3] were key instruments in identifying and quantifying noise mechanisms of stable swirling flows and those exhibiting vortex breakdown. Again, special configurations were employed to introduce upstream non-uniformities such that the aero-acoustic effect of inlet flow distortion could be quantified.

4. Assessment of Aircraft Integration. The feasibility of aircraft integration of swirl tubes for quiet drag was evaluated by assessing benefits and challenges of potential installation configurations to both current and future aircraft. The assessment also considered the effects of upstream flow non-uniformities on swirl tube performance using the experimental results from both wind tunnel facilities. Assessing the effects of such distortions on performance are critical given their common nature in real-world internal flow applications.

[2] In this thesis, the model is referred to a $1/7^{th}$ scale based on a 1.2 m engine diameter of the SAX 40 propulsion system. Although the same physical model is considered in Shah [29], he quotes a $1/12^{th}$ scale model based on an earlier engine design with a 2 m diameter.

1.6 Outline of Thesis

The research described in this thesis is presented in much the same order as the technical approach outlined in the previous section. The thesis is organized as follows.

Chapter 2 provides an overview of the WBWT and QFF wind tunnel test facilities used to experimentally assess swirl tube aerodynamics and aero-acoustics, respectively. A full listing of swirl tube configurations is given. Wind tunnel testing procedures, instrumentation, post-processing methods, and error considerations are each discussed as well.

Chapter 3 details the mechanical design of the swirl tube wind tunnel test model. Criteria for successful aerodynamic, acoustic, and structural design for testing in two wind-tunnel test facilities are presented. The chapter also includes model sizing considerations, component material selections, part fabrication techniques, and full test model structural analysis. Given these design considerations, a modular $1/7^{th}$ scale model was devised and implemented with safety factors of at least 1.5 as to avoid risk of structural failure during wind tunnel testing.

Chapter 4 contains an experimental assessment of swirling exhaust flow aerodynamics and aero-acoustics. Swirling flow aerodynamics are assessed both qualitatively and quantitatively in terms of drag generation capabilities and exhaust wake velocity and swirl characteristics with the result that swirling exhaust flows are capable of generating device-scale drag coefficients of 0.8. Noise mechanisms were located, identified, and quantified to confirm that stable swirling flows are quiet and that a high-drag, low-noise solution exists for swirl angles less than 50°. Comparisons are made between the fundamentally different aerodynamic and aero-acoustic behaviors of stable swirling flows and swirling flows exhibiting vortex breakdown, confirming that the exhaust flow patterns and noise mechanisms associated with vortex breakdown inhibit drag generation while increasing noise level 10-15 dB over noise spectra of stable swirl configurations.

Chapter 5 addresses the feasibility of swirl tube integration into aircraft design to meet specific approach drag and noise requirements. The SAX-40 aircraft provided a basis for assessing three installation configuration concepts. Full-scale drag coefficients, noise levels, and configuration weights are estimated for each swirl tube installation to provide a means of evaluating benefits and challenges of the integration options. The analysis suggests that the greatest performance benefit is obtained from propulsion system-integrated swirl tubes, so-called engine air brakes, which show a potential for a 6+ dB overall approach noise reduction for various standard tube-and-wing aircraft of today. Experimental drag and noise test results of the swirl tube subjected to various inlet distortions show that upstream flow non-uniformities have minimal effects on swirl tube drag and noise performance. The installation and flow non-uniformity assessments supply grounds for evaluating the swirl tube as a plausible solution for quiet drag applications.

Chapter 6 summarizes the key points from Chapters 1 through 5. Recommendations for further studies are also included for future experimentation of swirling exhaust flows for quiet drag applications.

Chapter 2

Wind Tunnel Facilities and Test Programs

2.1 Overview of Wind Tunnel Test Facilities

The experimental assessment of the swirl tube aerodynamic performance and aero-acoustic characteristics took place in two separate venues: the Wright Brothers Wind Tunnel at MIT and the Quiet Flow Facility at the NASA Langley Research Center. Drag measurements and wake flow field surveys were conducted at the Wright Brothers Wind Tunnel (WBWT) to assess steady streamwise vortex flows and swirling flows exhibiting vortex breakdown as well as to rigorously quantify the drag generation capabilities of swirling exhaust flows. Acoustic measurements at the Quiet Flow Facility (QFF) were used to identify and locate noise source mechanisms of swirling flows and to quantify their noise levels. The test programs at both wind-tunnel facilities involved numerous measurement techniques, including force balance measurements, hotwire anemometry, flow visualization, and microphone array acoustic measurements. These techniques were applied to various swirl tube configurations, testing variations of free stream Mach number, turning vane angle, and inlet flow non-uniformity. This chapter provides descriptions of the various swirl tube configurations used in wind tunnel tests, overviews of both the WBWT and QFF facilities, and descriptions of the programs developed to test the swirl tube at each location. The final section of the chapter presents an analysis of experimental uncertainty and measurement errors.

2.2 Swirl Tube Test Model Configurations

The swirl tube configurations tested in both wind tunnel test facilities are divided into three categories: standard, alternate, and distortion configurations. This section provides detailed descriptions of each of these configuration categories and the specific configurations that comprise them. Aerodynamic and acoustic test results for the standard and alternate

configurations are discussed in Chapter 4 while results for the distortion cases are discussed in Chapter 5.

2.2.1 Standard Swirl Tube Configurations

Forming the heart of the experiments, eleven standard swirl tube configurations provided a means of comparing the aerodynamic and aero-acoustic behavior of non-swirling flows, stable swirling flows, and unsteady swirling flows exhibiting vortex breakdown. These standard configurations include five non-swirl cases and six swirl cases. The non-swirl cases were included to assess the drag and noise generated from swirl tube components in the absence of swirl, essentially establishing a baseline for nacelle and vane aerodynamic and aero-acoustic performance. These components include the support pylon, the swirl tube nacelle without vanes or centerbody, and the swirl tube with non-swirling straight vanes (vane angle setting of 0°). The empty nacelle and straight vanes were each tested with and without boundary layer trip to evaluate any differences in drag production or noise signature.

The six swirl cases consist of turning vane angles of 34°, 41°, 47°, 53°, 57°, and 64° to include cases yielding steady streamwise vortices (34°, 41°, and 47°) as well as cases exhibiting vortex breakdown (53°, 57°, and 64°). Turning vane angles for different configurations were changed by means of exchanging "visks", defined here as "vaned-disks" that are each comprised of one set of twenty turning vanes connected to a shroud at the vane tips and a center-body mount at the vane hubs. More on the specific choices of turning angles as well as the implementation of visks is covered in the description of the swirl tube mechanical design in Chapter 3.

2.2.2 Alternate Swirl Tube Configurations

Alternate configurations were included in both wind tunnel test programs to vary critical swirl tube parameters for means of comparison. For example, a visk identical to the standard 47° visk but with half the number of turning vanes was tested to assess the effects of lower solidity on the swirl vanes' ability to turn the flow and the self noise from the vanes. Similarly, the swirl tube with 47° turning vanes was outfitted with a blunt rear centerbody piece with a rounded, 4.76 mm (0.188 in) trailing edge radius as opposed to the extremely sharp standard rear centerbody to highlight features of the acoustic spectra associated with the centerbody trailing edge. Lastly, a fully blocked nacelle case was included to provide a comparison of bluff body drag to that generated by swirling flows for the same inlet area. For this configuration, solid blocker plates were mounted flush to the inlet leading edge and nacelle trailing edge of the swirl tube, completely preventing flow from passing through the nacelle. Figures 2.1a-c show photos of each alternate swirl tube configuration.

Results from the alternate configurations are not presented in this thesis. The fully-blocked case, intended to provide an assessment of bluff body drag and noise performance, is not an adequate comparison for the swirl tube. A more adequate assessment of the swirl tube's performance as compared to conventional devices would be the comparison of the noise generation from a wing with conventional drag devices deployed to that of a clean wing with swirl tubes sized and installed to provide the same amount of drag during approach.

While important to identifying the noise characteristics particular to the centerbody, results from the modified centerbody trailing edge geometry cases were not included either because the cases for which data were collected were insufficient for a complete analysis.

Although intended to distinguish characteristics of vane wake noise from the noise signature of swirling flows, results of the 47° reduced vane count visk design are not presented because the visk failed to achieve the same amount of flow turning as the 47° case with 20 vanes. The acoustic measurements suggested potential flow separation in the vane passages, eliminating the possibility of accurately extracting the vane self noise.

2.2.3 Swirl Tube Configurations with Inlet Flow Non-Uniformity

Three adaptations to standard swirl configurations, known as the distortion configurations, examined the changes in swirl tube performance when subjected to non-uniform inlet flows. Testing of these cases provided an assessment of the effects of flow distortions on swirl tube drag and noise performance. This assessment, detailed in Chapter 5, is an important consideration in the evaluation of the viability of the swirl tube as a plausible drag-generating device for aircraft given the common presence of flow non-uniformities in internal flow applications. The three distortion configurations discussed in this subsection are shown mounted on the swirl tube in Figure 2.1.

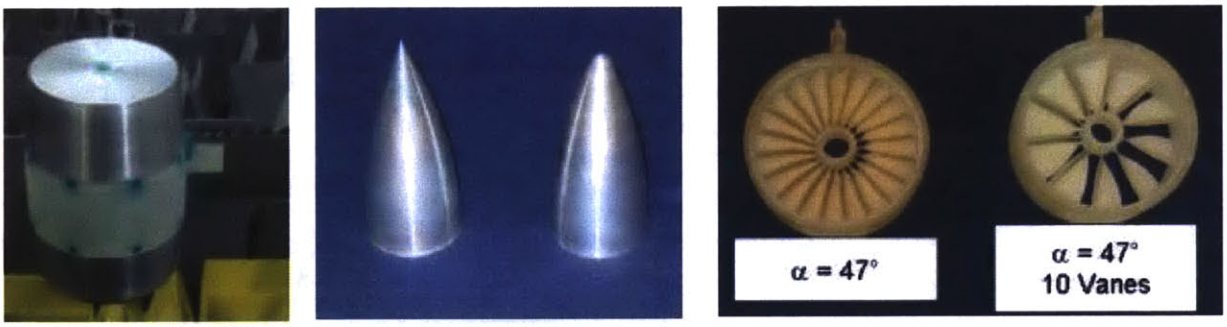

(a) Fully-Blocked Nacelle **(b)** Std. and Blunt Rear Center bodies **(c)** 47° visks with 20 and 10 vanes

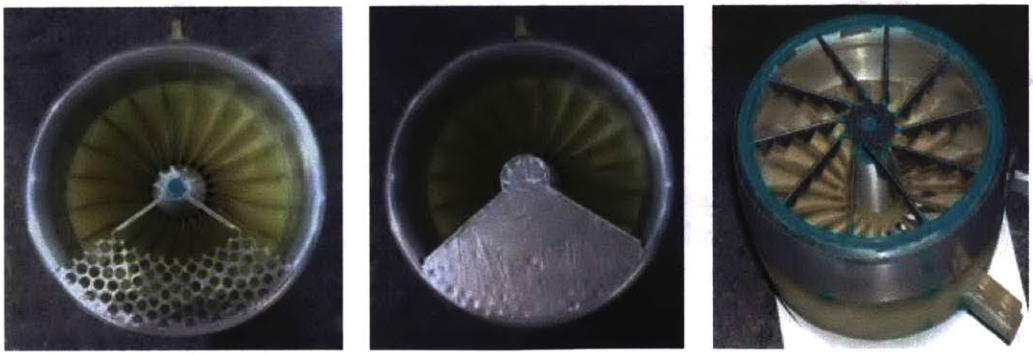

(d) 120° Perforated Plate **(e)** 120° Solid Plate **(f)** Blade Wake Simulator

Figure 2.1. Alternate and distortion swirl tube configurations.

Two distortion configurations introduced circumferentially-asymmetric flow non-uniformities in the form of local stagnation pressure deficits to the swirl tube inlet flow. The first of these cases was a perforated plate, constructed from 3.18 mm (0.13 in) thick aluminum sheet stock, creating a local stagnation pressure deficit approximately equal to four times the free stream dynamic pressure for a 120° sector of the nacelle inlet area. Over ninety 6.4 mm- (0.25 in) diameter holes were drilled in the outer portion ($r/R > 0.5$) of the plate, yielding a porosity of approximately 46%. The second asymmetric distortion case was generated by solid plate of 120°, created by sealing the holes of the perforated plate with aluminum tape.

The third distortion case introduced simulated blade wakes to the swirl tube inlet flow, as if the swirl vanes were installed in an aircraft engine duct aft of a row of fan outlet guide vanes. As discussed in Chapter 5, locating swirl vanes in an engine fan bypass or mixer duct is a suggested installation option for swirl tube integration onto aircraft, making the assessment of swirl tube drag and noise performance with upstream blade wakes critical. The ten blade wakes were simulated using a thin aluminum wheel with ten circumferentially swept spokes, each 3.18 mm (0.13 in) thick and 25.4 mm (1 in) in maximum length (chord). To emulate the aerodynamic shape of upstream blades, the spokes were shaped with rounded, semi-circular leading edges and sharp, serrated trailing edges made of aluminum tape. To ensure the wakes from the spokes were turbulent, grit particles were adhered generously to all surfaces of the spokes. The spokes were swept 60° circumferentially so that each wake would influence multiple turning vanes and vane passages.

2.3 Wright Brothers Wind Tunnel (WBWT) Facility Description and Test Program

The MIT Wright Brothers Wind Tunnel (WBWT) is a closed-loop return wind tunnel capable of generating test section free stream velocities exceeding 58.1 m/s (130 mph). The test section is a 2.3 m x 3.1 m (7.5 ft x 10 ft) ellipse, shown in the inset of Figure 2.2. Data for this experiment were collected through a series of wind-tunnel entries in the spring, early summer, and autumn of 2006. Test objectives of the swirl tube in the WBWT included a full assessment of the drag generation capabilities of swirling flows, identification of the upper swirl limit where vortex breakdown is first detectable, and surveys of wake characteristics such as velocity profiles and swirl angle profiles.

2.3.1 WBWT Instrumentation

The test objectives outlined in Chapter 1 were achieved using multiple measurement tools and techniques at the WBWT. A multi-axis force balance, traversable hotwire probe, and smoke visualization techniques were used to conduct drag measurements and flow field surveys. This section describes the setup and operation of the measurement instruments utilized for data acquisition at the WBWT during wind tunnel testing of the swirl tube.

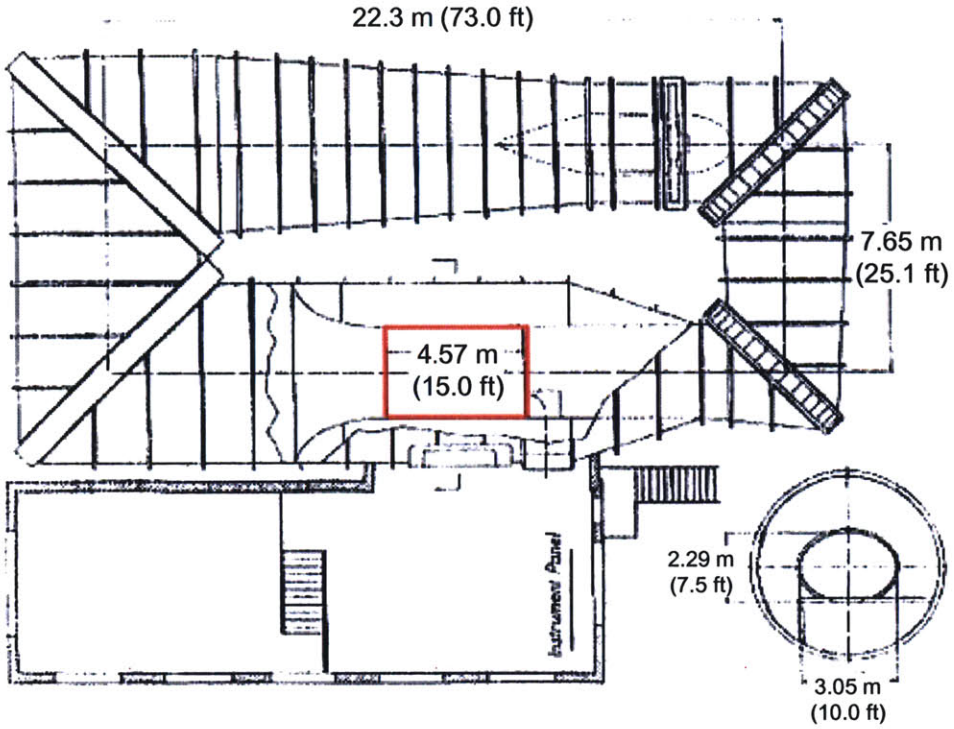

Figure 2.2. Schematic of MIT Wright Brothers Wind Tunnel (WBWT) facility. Test section is highlighted in red. Inset gives cross-sectional dimensions of the elliptic test section [18].

Drag measurements were conducted using a six-axis force balance. The force balance, located beneath the test section of the wind tunnel, was connected to the test model by means of a support beam, pictured in Figure 2.3. Each axis of the force balance used a strain gage to measure applied force in terms of a voltage. These voltages were converted into units of force by calibrating the device: applying known loads (weights) to the system and correlating the voltage outputs of the strain gages linearly to the magnitude of the specific loads. For a given test model configuration, drag data were acquired at Mach numbers of 0.03, 0.06, 0.09, 0.12, 0.15, and 0.17. Uncertainty of drag measurements is included in the error analysis in Section 2.5.

Wake surveys were conducted qualitatively through smoke visualization methods as well as quantitatively through hotwire anemometry to characterize the exhaust streams of swirling flows and to provide a basis for comparison between different swirl cases. Smoke visualization was utilized to provide general, visual impressions of the flow field. A heated, hand-held wand injected vaporized glycol at locations of interest. For example, injecting smoke into the swirl tube inlet near the core region of a stable swirling configuration produced visualizations of the low-pressure, high-velocity core plume exiting the swirl tube while positioning the smoke wand closer to the inlet perimeter near the shroud revealed the organized, stable, streamwise vortex exiting the nacelle. Photo stills of smoke visualizations for various configurations are presented and discussed in Chapter 4.

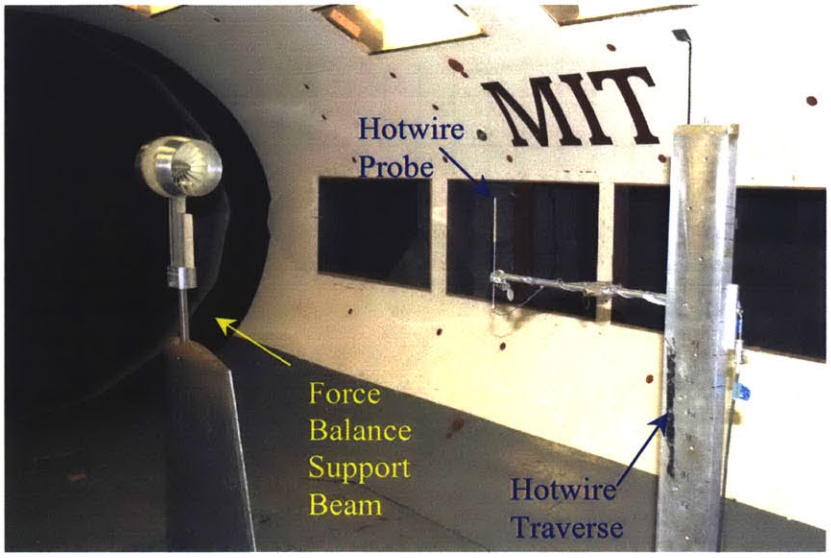

Figure 2.3. Instrumentation setup for WBWT aerodynamic tests. Dual stepper motors on the traverse mechanism control the longitudinal and vertical positioning of the hotwire probe.

A traversable hotwire probe, also pictured in Figure 2.3, was used to measure axial and tangential velocity profiles downstream of the swirl tube nacelle exit as well as unsteady velocity perturbations for various test model configurations. The hotwire probe was mounted on a dual-axis traverse system centered along the swirl tube's axis of symmetry. Stepper motors allowed the probe to traverse in the streamwise, horizontal direction (z direction) and in the vertical radial direction with a precision of 0.03 mm (0.001 in). Since hotwire calibrations were conducted for Mach numbers up to and including 0.17, the maximum free stream Mach number achievable at the WBWT, all hotwire measurements were taken at a free stream Mach number of 0.06 to account for the measurement of higher Mach numbers (up to twice that of free stream) experienced in the high-velocity core regions of steady swirling cases. Vibrations on the vertical tower of the hotwire traverse were minimized during data acquisition by connecting tension wires from the top of the traverse tower to the wind tunnel sidewalls.

Both steady and unsteady velocity measurements were taken using the hotwire traverse system, representing the mean velocity, $\overline{v}$, and velocity perturbation, v', terms, respectively, as given by

$$v(r,z,t) = \overline{v}(r,z) + v'(r,z,t). \tag{2.1}$$

Steady velocities were measured at locations one half-, one-, two-, and four-times the nacelle exit diameter downstream of the swirl tube exit. Figure 2.4 shows the radial distribution of the steady velocity measurements pictured as red lines, with the greatest concentration of measurements taken near the center (r/R = 0) and nacelle trailing edge (r/R = 1) regions to best capture the velocity changes of the core and nacelle shear layer. Half the number of points measured at downstream stations z/D = 0.5 and z/D = 1.0 were measured at axial locations z/D = 2.0 and z/D = 4.0 since the distinct core and shear layer profiles mix out by the time these outer locations are reached.

Unsteady velocities were sampled using the hotwire probe by extending the period in which data were acquired. For each point at which unsteady velocity data were taken, 16,384 samples were collected per window, sampled at 40 kHz using a bandwidth of 2.44 Hz. 100 windows were acquired for each unsteady velocity data collection location, thus data were sampled for 40.96 seconds. Four positions were sampled at each downstream axial location to capture unsteady velocity phenomena of the core, mid-radius, nacelle trailing edge, and free stream: r/R = 0.0, 0.5, 1.0, and 1.5, respectively. Steady velocity profiles and unsteady velocity results are presented and analyzed in Chapter 4.

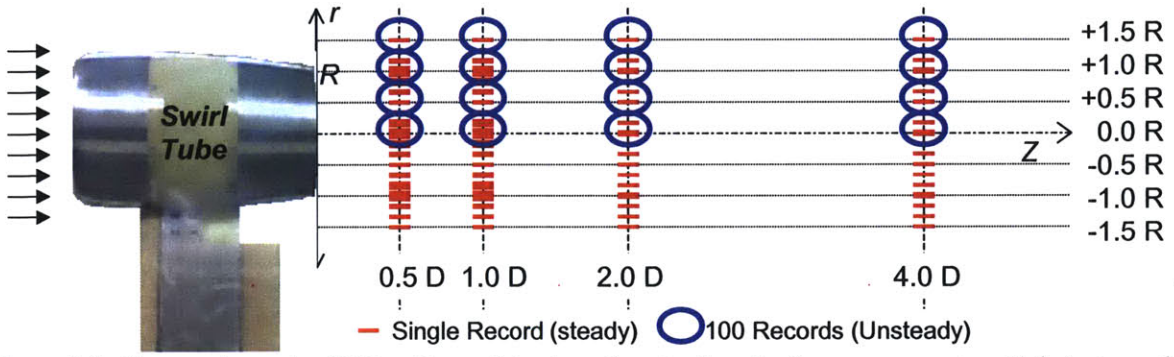

Figure 2.4. Streamwise and radial locations of steady and unsteady velocity measurements with hotwire probe.

2.3.2 WBWT Data Reduction

This section describes the methods used to reduce raw data acquired by force balance and hotwire measurements.

2.3.2.1 Force Balance Data Reduction

To compute the drag coefficient of a given configuration, drag measurements were conducted at free stream Mach numbers of 0.03, 0.06, 0.09, 0.12, 0.15, and 0.17. At each of these Mach numbers, the free stream dynamic pressure, defined as

$$q_{\infty,n} = \frac{1}{2}\rho V_n^2 = P_{Total,n} - P_{Static}, \tag{2.2}$$

was computed using free stream stagnation and static pressure data from a pitot-static probe. The drag coefficient for the given configuration was thus calculated as the average of the drag coefficients computed at each Mach number, M_n. For a given configuration,

$$C_D = \frac{1}{N}\sum_{n=1}^{N}\frac{D_n}{q_{\infty,n}A_{flow}}, \tag{2.3}$$

where N is the number of Mach numbers at which data were taken, n references a specific Mach number at which data were taken, D_n is the drag force measured at Mach number M_n, and A_{flow} is the swirl tube annular flow area at the turning vane leading edges.

2.3.2.2 Hotwire Data Reduction

Reduction of data from hotwire measurements required the conversion of measured voltage to velocity. To best understand the details of this conversion, a brief overview of hotwire anemometry is presented. A hotwire anemometer is a Wheatstone bridge circuit: a circuit that uses fixed and variable resistors of known values to calculate the resistance of a given element, defined as the unknown resistance. In the case of a hotwire probe, the unknown resistance is that of the thin, heated thermoelectric element (wire). The resistance of the element varies with the rate at which heat is convected from the element by the surrounding fluid, dictated by the local velocity perpendicular to the axis of the wire. This instantaneous variation in resistance of the element, or unknown resistor, manifests itself as variations in voltage within the structure of the Wheatstone bridge circuit. Thus, measuring changes in circuit voltage provides a means for measuring local velocity in the direction perpendicular to the axis of the wire. Voltage-velocity relation was determined by daily calibrations of the hotwire probe, which yielded best-fit calibration curves of the form

$$E^2 = C + Du^n, \tag{2.4}$$

where E is the measured voltage; u is the corresponding local velocity; and C, D, and n are constants. By properly orienting the axis of the hotwire probe, velocities were measured in both the axial direction, v_z, and tangential direction, v_θ, to generate axial and tangential velocity profiles as functions of swirl tube radius. Using these velocity profiles, swirl angle distribution, $\alpha(r)$, was calculated from the velocity triangle.

$$\alpha(r) = \arctan\left(\frac{v_\theta(r)}{v_z(r)}\right) \tag{2.5}$$

It is evident from the above description of hotwire instruments that there is uncertainty involved in hotwire flow measurements. The device's dependence on ambient temperature as well as the accuracy of alignment of the probe relative to the swirl tube are critical to the quantification of hotwire measurement error. Uncertainty in hotwire measurements is assessed in Section 2.5.

2.3.3 WBWT Test Program

Drag measurements via force balance were taken for each of the eleven standard swirl tube configurations. These measurements were taken at Mach numbers ranging between 0.03 and 0.17, the latter of which is typical of commercial aircraft on approach, a flight regime where swirl tube quiet drag technology is most likely to be applied, if feasible. Smoke visualization was implemented for the swirl cases to qualitatively compare stable swirling flow to flows

demonstrating vortex breakdown. Images resulting from the smoke visualization of stable swirling cases were also used to compare the geometries of the streamwise vortex structures for different vane turning angles, including axial spacing between successive rotations of the vortex helical motion and relative diameters of the high-velocity, low-pressure core streams. To make these same comparisons in a quantitative manner, steady and unsteady wake velocity data were gathered for the 34°, 47°, 53°, 57°, and 64° cases via traverses of a hotwire probe. For baseline comparisons of unsteady velocity phenomena stemming from the nacelle trailing edge and the turning vane wakes, unsteady velocity data were gathered for the empty nacelle and 0° visk cases.

The WBWT test program also included assessments of the alternate configurations described in Section 2.2.2. Hotwire traverses were conducted on the 47° swirl case with ten turning vanes as well as the 47° swirl case with blunt rear centerbody to extract differences in velocity profiles and/or unsteady velocity spectra caused by reducing the vane count and changing the rear centerbody geometry. Drag measurements were taken for the fully blocked case to provide a comparison of bluff body drag to that generated by swirling flows for the same inlet area.

Drag assessments of the three distortion configurations described in Section 2.2.3 were also included in the WBWT test program. The 120° perforated plate and solid plate distortion cases introduced significant asymmetries into the swirl tube inlet flow, interfering with the symmetry of the stable streamwise vortex which gives rise to pressure drag. Thus, drag measurements were conducted on the swirl tube with 47° turning vanes with the perforated inlet distortion plate as well as the solid 120° distortion wedge affixed to the nacelle leading edge for comparison with drag levels of the baseline 47° case. Drag as well as hotwire steady and unsteady wake velocity measurements were conducted on the 47° swirl case with inlet blade wake simulator to assess the effects of symmetric wake distortion at the nacelle inlet on the drag performance and swirl capabilities of the baseline 47° case.

Table 2.1 provides a summary of the aerodynamic wind tunnel tests of the swirl tube at the WBWT.

2.4 Quiet Flow Facility (QFF) Facility Description and Test Program

The NASA Langley Quiet Flow Facility (QFF) is a 9.1 m x 6.1 m x 7.6 m (30 ft x 20 ft x 25 ft) anechoic chamber, the air supply for which is introduced through a vertical 61 cm x 91 cm (2 ft x 3 ft) free jet centered in the floor of the chamber. The anechoic chamber, shown in Figure 2.5, is lined with acoustic foam wedges measuring 91 cm (3 ft) in height and 929 cm^2 (1 ft^2) in base area capable of absorbing sound waves at frequencies as low as 300 Hz, thus eliminating virtually all reflections of sound waves at higher frequencies. The exit of the vertical free jet is a 61 cm x 91 cm (2 ft x 3 ft) rectangular opening, bounded on its shorter sides by 1.83 m (6 ft) tall aluminum sidewalls. These sidewalls provide mounting points for test models and the rotating microphone array, discussed in the next subsection. Historically, the QFF has been used to measure dipole- and/or scattering-type noise sources, such as airfoil self-noise [5], leading edge slat noise [23, 24], flap side-edge noise [4, 22], wing tip vortex noise [2], turbulent vortex shedding noise from landing gear cylindrical struts [17], etc. Aero-acoustic testing of the swirl

tube, however, presented the facility's first opportunity to measure volume sources (i.e. quadrupoles) using microphone arrays.

2.4.1 QFF Instrumentation

Acoustic measurements were taken using data acquired from six fixed microphones and a traversable microphone array consisting of 41 microphones. The six fixed Brüel & Kjær (B&K) 4138 microphones were mounted to poles on either side of the vertical free jet at forward, sideline, and aft angles, 1.98 m (6.5 ft) from the center of the swirl tube's exit plane (see Figure 2.4). The medium aperture directional array (MADA) is a phased array of 41 B&K 4138 microphones spaced 1.52 m (5 ft) from the center of the swirl tube's exit plane, arranged in concentric circles beneath a blue cloth wind screen, used to reduce the wind noise of ambient flows near the array microphones. The MADA is affixed to a rotating arm, allowing the unit to measure noise sources from the test article at multiple forward, sideline, and aft angles. The data acquisition capabilities of the MADA coupled with advanced post-processing techniques made the location of noise sources in the flow field possible to within 2.54 cm (1 in), the details and methods of which are described in the next subsection.

	Measurements	**Steady Velocity**	**Unsteady Velocity**	**Drag**	**Smoke Visual.**
	Instrumentation	Hotwire	Hotwire	Force Balance	Smoke Wand
	Mach Number(s)	M = 0.06	M = 0.06	M = 0.03-0.17	M = 0.03
Standard Configurations	*Pylon Only, No BL Trip			X	
	*Empty Nacelle, No BL Trip			X	
	Empty Nacelle		X	X	
	*Straight (0°) Vanes, No BL Trip			X	
	Straight (0°) Vanes		X	X	
	34° Turning Vane Angle	X	X	X	X
	41° Turning Vane Angle			X	X
	47° Turning Vane Angle	X	X	X	X
	53° Turning Vane Angle	X	X	X	X
	57° Turning Vane Angle	X	X	X	X
	64° Turning Vane Angle	X	X	X	X
Alternate Configurations	47° Vanes with Blunt Rear Centerbody		X		
	47° Vanes, 10 Vanes	X	X	X	
	Full Blockage			X	
Distortion Configurations	47° with 120° Perforated Plate			X	
	47° with 120° Solid Wedge			X	
	47° with Blade Wake Simulator	X	X	X	

Table 2.1. Swirl tube aerodynamic test program for MIT WBWT experiments. All configurations except those indicated with * include boundary layer trips on nacelle and vanes.

Signals from all 47 microphones, six pole-mounted plus 41 array, were amplified using B&K 2670 pre-amplifiers and B&K 5935L power supplies, shown in the wiring schematic of Figure 2.6. Amplified signals passed through elliptic high and low-pass filters set at 50 Hz and 70 kHz, respectively, before recording in the data acquisition unit (DAQ). Gains introduced from the pre-amplifiers boosted signals by 30 to 50 dB while the high pass filter supplied an additional 2x, 4x, or 8x gain[3], depending on the strength of the original signal. Gain settings were recorded for each configuration and removed from data prior to data analysis. Three million samples were taken per data acquisition, sampling at a rate of 142 kHz. To correct for the increases in sound-pressure caused by the diffraction of sound waves around individual microphones, data from correction curves from Figure 2.7 are subtracted off raw noise spectra [6]. The corrections are more prominent at high frequencies as shorter acoustic wavelengths become increasingly comparable to the small outer dimensions of the microphones. The 0° incidence curve in Figure 2.7 was used for all microphone corrections since all array and pole microphones were oriented such that they pointed directly at swirl tube.

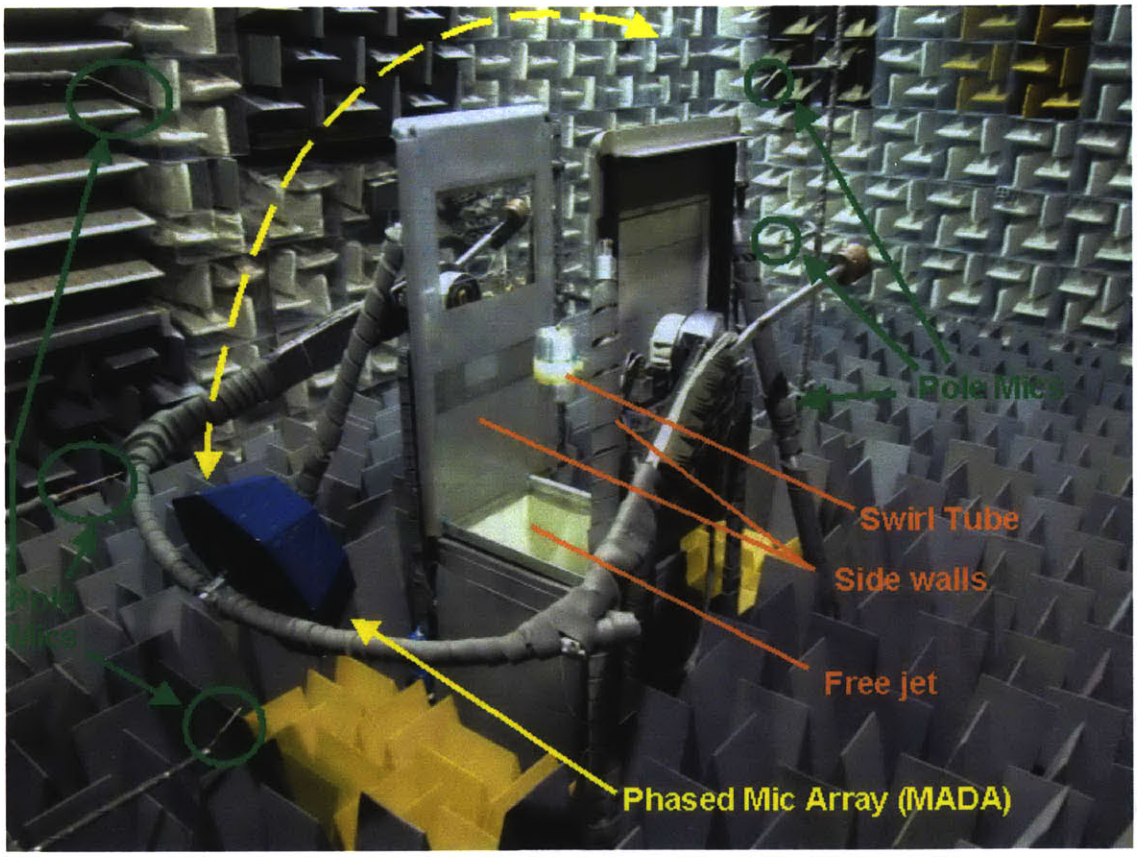

Figure 2.5. Swirl tube aero-acoustic test setup in anechoic test chamber of QFF. Phased microphone array (MADA) shown in 107° forward angle position relative to swirl tube axis of symmetry.

[3] A high-pass filter gain of Nx is equivalent to a signal increase of $20\log_{10}(N)$ dB.

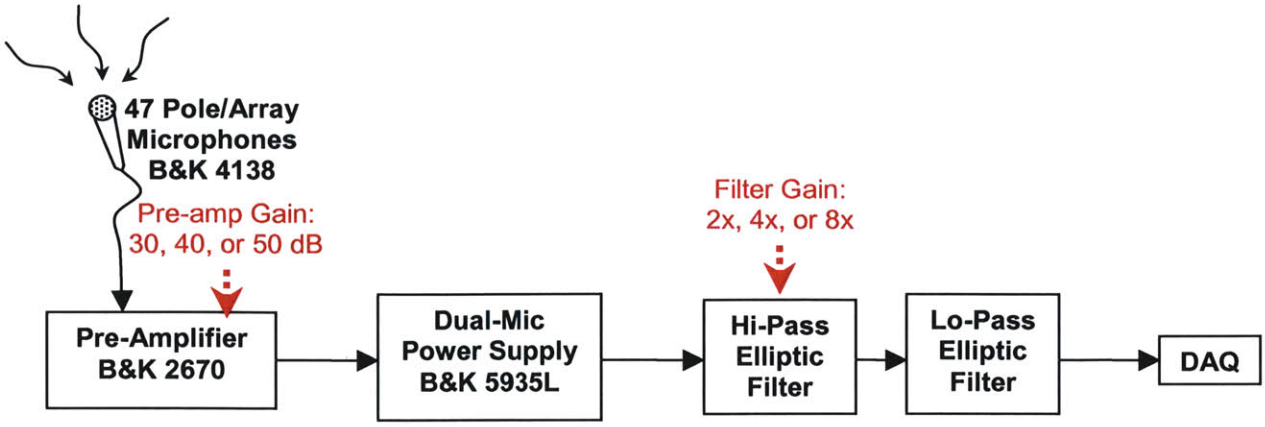

Figure 2.6. Instrumentation and wiring schematic for QFF acoustic data acquisition.

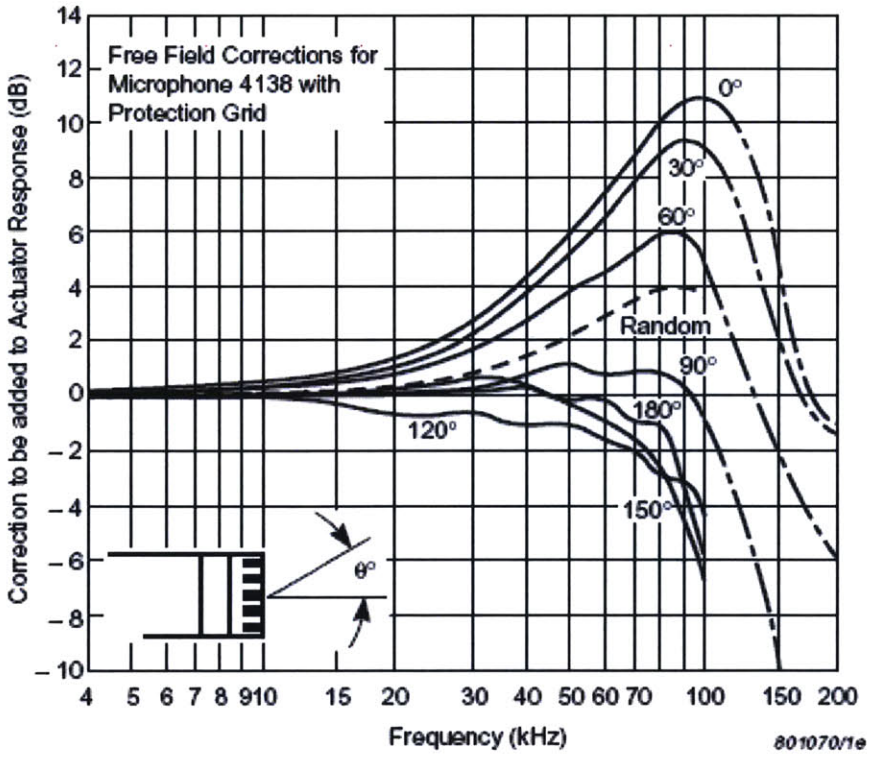

Figure 2.7 B&K 4138 correction curves for various incidence angles. Since all array and pole microphones were pointed directly at swirl tube trailing edge, the 0° curve was used for all microphone corrections [6].

2.4.2 Post-Processing Technique for Phased Array (MADA) Data

A revolutionary new approach to noise source spatial location and quantification has been developed by Brooks et al. [3] at the QFF that deconvolves traditional beamforming results to provide state-of-the-art mapping of noise mechanisms. This method, the Deconvolution

Approach for the Mapping of Acoustic Sources, or DAMAS, was the key enabler to identifying and quantifying noise sources associated with the rather quiet swirling flows. This section provides a brief overview of the technique, its advantages over standard array beamforming methods, and its application to the aero-acoustic wind tunnel testing of the swirl tube. For more information on the novel DAMAS approach, consult Brooks and Humphreys [3].

As discussed in Chapter 1, a critical test objective for model scale aero-acoustic testing of the swirl tube at the QFF is the identification and quantification of noise mechanisms of swirling flows and related vortex breakdown phenomena. While analysis of microphone autospectra can provide insight into the identification of noise sources via Mach number scaling techniques (see Chapter 4), this analysis lacks the capability to locate and quantify acoustic sources spatially. Previous aero-acoustic studies have thus turned to standard array beamforming techniques, which utilize delay and sum[4] processing to identify noise source distributions and generate cross-spectral matrices. The problem with standard array beamforming is the inherent complexity of the interpretation of results, which are typically convolved with array response function characteristics such as array size and geometry. This is evident in the governing equation for standard array beamforming, given as

$$Y(\hat{e}) = \frac{\hat{e}^T \hat{G} \hat{e}}{m_0^2} \tag{2.6}$$

from [3], where $\hat{e}$ is the matrix of steering vectors used to focus the array to a given point in space, $\hat{e}^T$ is the transpose of this matrix, $\hat{G}$ is the cross-spectral matrix, m_0 is the number of array microphones, and $Y(\hat{e})$ is the output acoustic power response of the array at the given point in space. The matrix of steering vectors, $\hat{e}$, contains references to array beamforming pattern characteristics, including the adjustments for shear layer refraction of acoustic ray paths in distance and time. Thus the DAMAS method seeks to clearly identify noise source strength distributions without reference to characteristics of array response functions.

The DAMAS approach uses an inverse problem solution of a system of linear equations to precisely extract the source strength distributions from the beamforming characteristics. These equations are derived by first computing a modified cross-spectral matrix, comprised of elements that are products of inverse array response functions, e^{-1}, and the Fast Fourier Transform (FFT) of pressure time records as measured by array microphones in the absence of array response characteristics. Modifying the cross-spectral matrix in such a way effectively separates the beamforming array characteristics from the acoustic source distributions and thus alters the governing equation. The output power responses obtained from the standard and modified governing equations, $Y(\hat{e})$ and $Y_{\text{mod}}(\hat{e})$, respectively, can be equated on a grid point-by-grid point basis to yield the following linear system of equations:

$$\hat{A}\hat{X} = \hat{Y} \tag{2.7}$$

[4] Delay and sum methods seek to focus acoustic signals from array microphones on individual points in space by delaying signals from each array microphone in time based on microphone position within the array. The delayed signals from all microphones are then summed and processed to form a cross-spectral matrix.

where $\hat{A}$ is the extracted DAMAS matrix accounting for reciprocal influences of array beamforming characteristics, $\hat{Y}$ is the output response matrix, and $\hat{X}$ is the matrix of noise sources expressed as mean square pressure per bandwidth. For acoustic problems of relevant interest in terms of spatial grid size and resolution, the matrix $\hat{A}$ is singular. Thus, an iterative method must be used to solve Equation 2.7 for sources $\hat{X}$. The governing assumption in the method, that all sources X_n are statistically independent, provides a positivity constraint that is gradually imposed to compute a converged solution.

The acoustic noise mapping capability of DAMAS methods was rigorously assessed by Brooks and Humphreys [3] using both computer-simulated and experimental noise sources. Figure 2.8, adapted from Brooks and Humphreys [3], compares the noise source mapping capabilities of conventional beamforming with DAMAS processing techniques using 1, 1,000, and 5,000 iterations of single component equations in an algorithm based on the expression given in Equation 2.7. In this example, the computationally-constructed noise source, spelling the acronym "NASA", is indiscernible through standard beamforming techniques while DAMAS processing of the same noise source maps the source with unparalleled clarity and resolution, improving with increasing iterations. The DAMAS technique has also been validated using physical noise sources, such as monopole point sources commonly used to calibrate acoustic instrumentation [3].

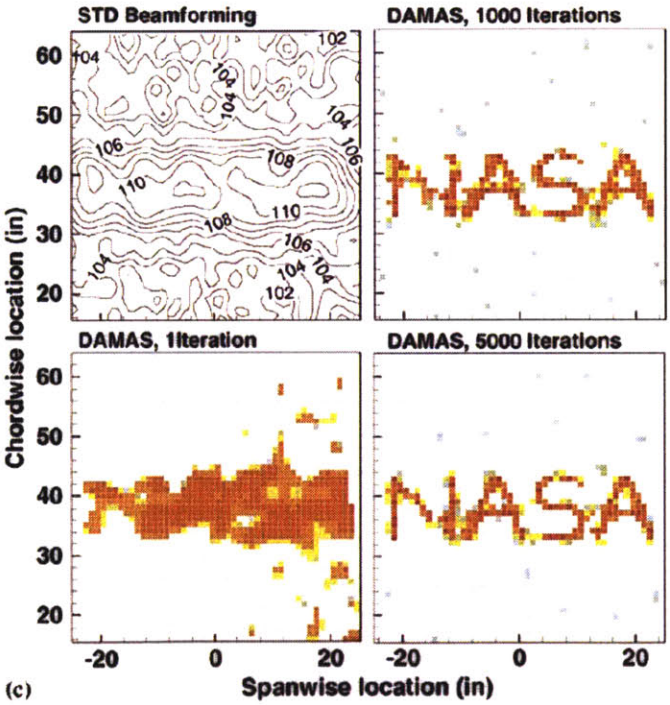

Figure 2.8. Computational "NASA" noise source location maps processed with standard beamforming (upper left) and DAMAS techniques of various iterations [3].

Data results from the DAMAS post-processing method supplied means for creating source location maps, or contour plots, of swirl tube acoustic sources in space. Figure 2.9 compares standard array beamforming and DAMAS-processed results for the 47° stable swirl case. Though standard beamforming correctly highlights the swirl tube aft region as the general location of dominant noise sources, the DAMAS-processed result clearly distinguishes between noise sources located at the nacelle trailing edge and those located approximately one nacelle exit diameter downstream of the nacelle exit. Noise sources identified in these locations in the DAMAS-processed result are indicative of turbulent scattering noise sources and open-flow quadrupoles, respectively, as would be expected from stable swirling flow with a high-velocity viscous core stream, detailed further in Chapter 4.

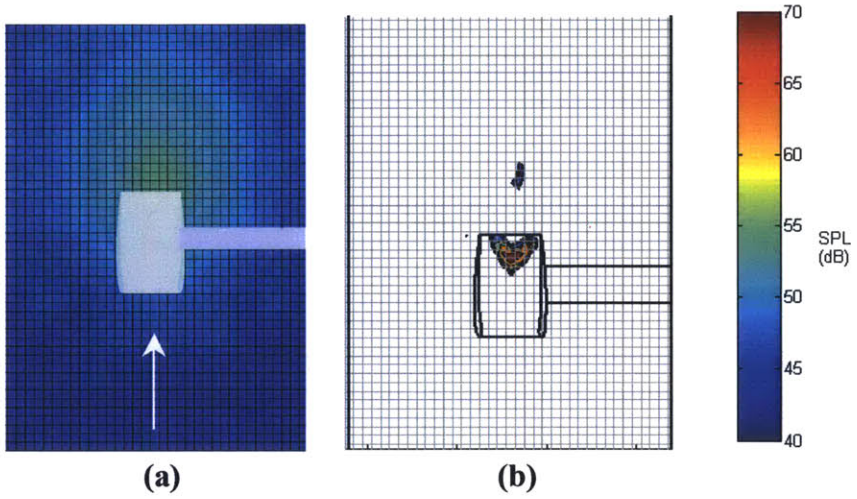

Figure 2.9. Standard array beamforming (a) and DAMAS-processed (b) one-third octave noise source maps of 47° swirl case at 16 kHz for free stream $M = 0.17$. While standard beamforming correctly highlights the general region of noise sources, the DAMAS-processed result clearly shows distinct noise sources at the nacelle trailing edge and downstream.

DAMAS processing also provides the ability to extract noise spectra from any user-defined region of interest. In its raw format, noise source distribution data that has been DAMAS-processed is given in terms of sound pressure level at each grid location, shown in Figure 2.9b, for all narrowband and one-third octave frequencies of interest. Each grid square represents a 2.54 cm x 2.54 cm (1 in x 1 in) spatial element, the resolution of the DAMAS source location technique. From this, acoustic spectra for can be selectively extracted for any user-defined region by summing SPLs of a set of grid points on a p^2 basis. Thus the spectra of SPL for a region R composed of individual grid points n is given as

$$SPL_R = 10\log\left[\sum_n p_n^2\right] = 10\log\left[\sum_n 10^{SPL_n/10}\right]. \tag{2.8}$$

This process was used extensively in particular regions in the flow field, such as nacelle and pylon trailing edges or downstream locations, to better characterize and quantify the acoustic

spectra of noise mechanisms inherent of the local region, as shown in the aero-acoustic assessment of Chapter 4. It should be noted, however, that the maximum resolution of grid points in all DAMAS-processed source location maps presented in this thesis is 2.54 cm x 2.54 cm (1 in x 1 in). Though the shape of the contours representing source strength spatial distributions may appear to be finer than this resolution scale, this is merely a consequence of the grid box center point-based method in which the grid box SPL magnitudes are represented (as opposed to the shading of individual grid boxes).

2.4.3 QFF Test Program

Swirl tube configurations tested in the QFF were the same as those tested in the WBWT with the exceptions of empty nacelle and 0° straight vane cases without boundary layer trip, which were not included in the QFF test program. Descriptions of the standard, alternate, and distortion configurations tested are included in Section 2.2.

Acoustic data were acquired for each configuration at six Mach numbers and six MADA array angles for a total of 36 total acquisitions per configuration. Mach numbers at which data were acquired included 0.07, 0.09, 0.11, 0.13, 0.15, and 0.17. Forward, sideline, and aft MADA array angles were included in the QFF test program to capture the directivity of swirl tube noise mechanisms. MADA array angles were measured relative to the swirl tube axis of symmetry with 0° located directly aft of the nacelle exit (above the model in Figure 2.5) and 90° located perpendicular to the swirl tube axis of symmetry, deemed the sideline angle. Array measurements were taken at two forward angles, 124° and 107°; the sideline angle, 90°; and three aft angles, 73°, 56°, and 45°. Measurements were not conducted at array angles further aft of 45° due to the increasing effects of the free-jet shear layer on the vibration of the MADA microphone array. The accuracy of these angles relative to the swirl tube was ensured by periodic calibrations using precise dual-beam laser alignment.

Aero-acoustic test results for the standard, alternate, and distortion configurations are discussed in Chapters 4 and 5.

2.5 Error Analysis of Measurements

This section discusses both bias and random errors of measurements and data reduction methods for both aerodynamic and aero-acoustic wind tunnel testing of the swirl tube. The total error for a given quantity is composed of the root-mean-square of the sum of the bias and random errors,

$$e_{total} = \sqrt{e_{bias}^2 + e_{random}^2} \,. \tag{2.9}$$

For convenience, the errors presented and discussed in this section are summarized in Table 2.2.

	Quantity	Bias Error	Random Error	Total Error	% of Reference Quantity
Aerodynamic	Drag Coefficient, C_D	0.006	0.037	0.037	4.5% of 47° C_D
	Flow Velocity, m/s (mph)	0.05 (0.11)	1.66 (3.71)	1.66 (3.71)	8.1% of V_∞ for hotwire data acquisition
Acoustic	OASPL, dBA	2.00	0.52	2.07	4.9% of 47° OASPL

Table 2.2. Summary of swirl tube aerodynamic and aero-acoustic measurement error. All quantified measurement errors are less than 10% of reference measurements.

2.5.1 Aerodynamic Measurement Errors

The random error involved in wind tunnel testing the swirl tube at the WBWT affects both the drag and hotwire results. As expressed in Equation 2.3, the drag coefficient for a given configuration is an average of the drag coefficients computed at each test Mach number, M_n. These individual drag coefficients, however, are derived by averaging instantaneous force balance readings over a given period at which the model is subjected to the test Mach number. This period fluctuated based on the response time of the WBWT operator, thus some human judgment was used in obtaining the drag coefficients C_D (M_n). To quantify this error, a typical drag data acquisition period in which 50 samples were read from the force balance was found to have a maximum deviation from average of 10 mV and a voltage range of 16 mV. Using the force balance calibrated voltage-drag conversion of 25.2 mV/N (112 mV/lb), the mean free stream dynamic pressure q_∞ of those at which drag measurements were taken, 900 Pa (18.8 psf), and the flow area of the swirl tube taken at the vane leading edges, 235 cm^2 (36.5 in^2), this error converts to a random error in drag coefficient of 0.019.

Similarly, the random error due to repeatability of measurements can be quantified by comparing drag measurements repeated for the standard configurations. Figure 2.10 shows drag coefficient as a function of swirl angle, the data for which was sampled five months apart. The maximum difference in drag coefficient for each repeated measurement is an estimate for the drag measurement repeatability error. This maximum difference occurs for the 0° straight vanes, amounting to an experimental error in drag coefficient of 0.032, small compared to the drag coefficients near 0.80 of the high swirl cases. Thus, combining the error in drag averaging with the repeatability error by the sum of root-mean-squares, the random error in drag coefficient is found to be 0.037.

The bias error in drag measurements is obtained from the WBWT industrial data record [18]. For the six-component pyramidal force balance, the bias error in drag is 0.13 N (0.03 lb). Using the same mean free stream dynamic pressure, q_∞, and flow area, A, stated above, the bias error in drag coefficient is 0.006. The total error in drag measurement, the combination of random and

bias errors as given by Equation 2.9, is thus 0.037, 4.5 percent of the drag coefficient of the 47° swirl case.

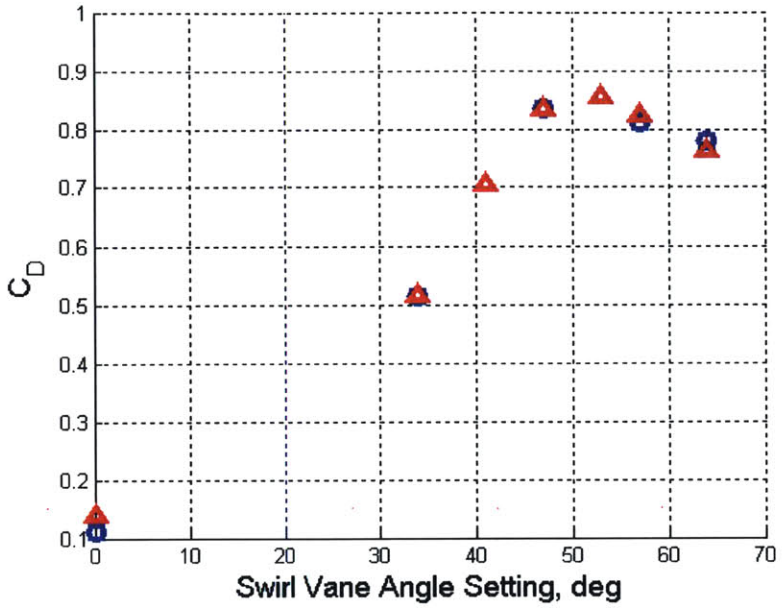

Figure 2.10. Drag coefficient versus swirl vane angle setting taken in March 2006 (blue) and August 2006 (red). Experimental error in drag coefficient, taken from the largest discrepancy of the repeated measurements, is 0.032.

Random error in hotwire measurements was due in part to slight variations in the alignment of the hotwire probe relative to the swirl tube and free stream flow. Alignments were performed by hand to both situate the wire exactly on the swirl tube axis of symmetry as well as orient the axis of the wire perpendicular or parallel to free stream flow direction for measurements of axial and tangential velocity, respectively. While a leveled laser beam was used to situate the hotwire exactly on the swirl tube axis of symmetry, orientation of the hotwire element axis was far less accurate, performed strictly by eye. It is assumed that variations of this orientation may have been as high as 5°, since angular variations of small axial objects, such as a hotwire element, that are smaller than 5° are difficult for the human eye to discern. An experimental study on the sensitivity of a hotwire anemometer to yaw angles conducted by Webster [31] states that velocity measured by at hotwire with yaw angle, ϕ, relates to the velocity measured with zero yaw angle by

$$U^2(\phi) = U^2(\phi)\left(\cos^2\phi + 0.04\sin^2\phi\right). \tag{2.10}$$

By this expression, a 5° yaw angle caused by incorrect positioning of the hotwire relative to an intended direction would yield a 1 percent error in measured velocity. For the free stream velocity at which hotwire measurements were conducted, 20.4 m/s (45.7 mph), this 1 percent error equates to 0.20 m/s (0.46 mph).

A second component of random error is determined by assessing the repeatability of hotwire measurements. Given a hotwire probe's dependence on free stream flow temperature, wind tunnel conditions on different test days will yield variations in hotwire calibration curves and, subsequently, variations in velocity results. Figure 2.11 shows hotwire calibration curves collected on four different test days. The maximum difference in voltage measured between the four calibrations, found to be 0.017 mV, is an estimate for the hotwire data repeatability error. This error in voltage corresponds to a 1.65 m/s (3.69 mph) maximum possible error in velocity based on an average of the calibration curves in Figure 2.11, equal to 8 percent of the free stream velocity at which hotwire measurements were conducted as given above. Thus the overall random error in hotwire measurements computed by the sum of root-mean-squares of alignment and repeatability errors is 1.66 m/s (3.71 mph).

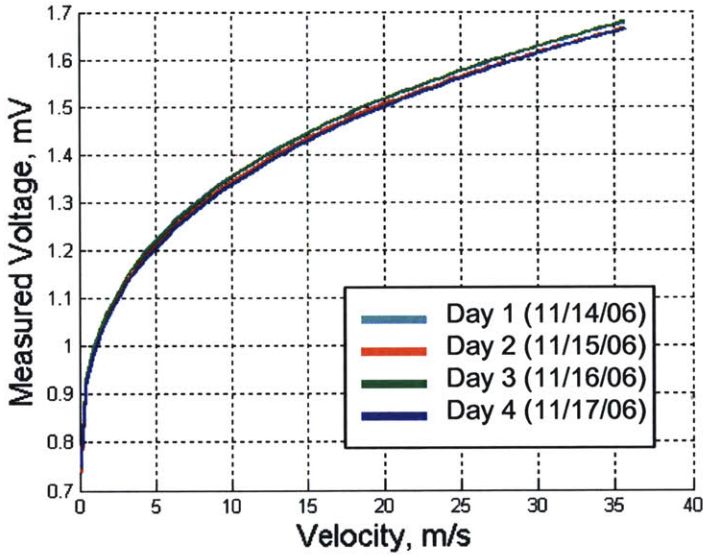

Figure 2.11. Conversion of hotwire-measured voltage to velocity by calibration. Four (overlapping) curves represent hotwire calibrations from four separate test days. Experimental error of measured voltages, taken from the largest discrepancy of hotwire calibrations, is 0.017 mV.

The bias error in hotwire measurements is obtained from product technical data on the website of the manufacturer, Dantec Dynamics, for single-sensor miniature wire probes [7]. This error is assumed equal to the minimum measurable velocity of 0.05 m/s (0.11 mph). Combining the random and bias errors in velocity measurement by summing root-mean-square quantities, the total error is found to be 1.66 m/s (3.71 mph), 8.1 percent of the free stream velocity at which hotwire measurements were conducted.

2.5.2 Aero-acoustic Measurement Error

The error in aero-acoustic swirl tube test results was also determined by the repeatability of experimental measurements. In all, eight swirl tube configurations were tested more than once

for the same free stream Mach number and MADA array angle settings. The discrepancies in noise signature for common cases are attributable to both human errors of setting identical wind tunnel test conditions as well as instrumentation error of the data acquisition system. Figure 2.12 shows narrowband noise spectra for the 47° stable swirl case taken at a free stream Mach numbers of 0.11 and 0.17 with the array situated at the 90° sideline angle on two different test days. The spectra show excellent repeatability between test days. To quantify the maximum repeatability error for acoustic measurements, differences in OASPLs were calculated for each of the eight repeated swirl tube cases. This maximum difference in OASPL was found to equal 0.52 dBA, a mere 1% compared to the 46 dBA OASPL of the 47° vane stable swirl case.

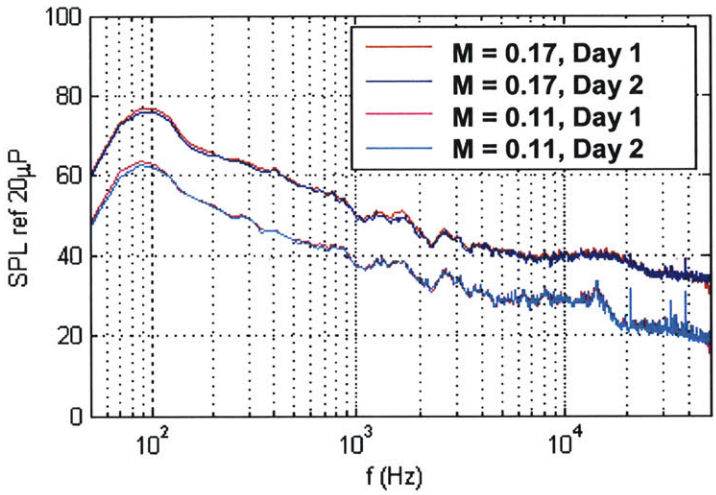

Figure 2.12. Comparisons of experimentally-measured narrowband (17.45 Hz) microphone autospectra for 47° swirl case taken at free stream Mach numbers of 0.11 and 0.17 on two different test days. Experimental error of noise results, taken from the largest discrepancy in OASPL of repeated measurements, is 0.52 dBA.

The bias error in acoustic measurements is obtained from product notes from the manufacturer, Brüel & Kjær, for the 4138 series of 1/8-inch pressure-field microphones [6]. The stated frequency response error is ± 2 dB for frequencies between 6.5 Hz and 140 kHz. Thus the total error in acoustic measurements, again estimated by the combination of random and bias errors as given by Equation 2.9, is 2.07 dBA, 4.9 percent of the full-scale OASPL of the 47° swirl case.

Chapter 3

Mechanical Design of Wind-Tunnel Test Articles

3.1 Overview of Swirl Tube Mechanical Design

The mechanical design of the swirl tube considered the test model's aerodynamic performance, compatibility with WBWT and QFF test facilities, construction material selection, and structural integrity. All of these design considerations were successfully implemented and the model scale swirl tube was manufactured and tested. This validates both the mechanical design and design choices leading to the final swirl tube test model configuration. Chapter 3 discusses the details of these key design considerations.

The $1/7^{th}$ scale swirl tube test model, 29.2 cm (11.5 in) in length and 20.3 cm (8 in) in maximum diameter, consists of a set of stationary turning vanes inside a straight nacelle duct. The aerodynamic design of the swirl tube is such that it creates a streamwise vortex to give rise to pressure drag. The mechanical design of the test model involved aerodynamic performance estimates of flow turning angles and drag coefficients as functions of turning vane geometry. The scale model was designed for testing in two wind-tunnel test facilities, the MIT WBWT and the NASA Langley QFF, both of which are described in detail in Chapter 2. This required appropriate sizing of the swirl tube model relative to the test facility dimensions as well as the design of structural members such as pylons necessary to support the model during testing. Proper selection of test model materials coupled with a structural analysis of the model under critical loading conditions factored into the mechanical design to remove any risk of structural failure of the swirl tube model in either wind-tunnel facility. The outcome of the structural analysis shows that nominal stress levels are well below material yield with safety factors greater than or equal to 1.5 employed at all critical structural locations.

3.2 Swirl Vane Aerodynamic Design

The swirl vanes utilized in this series of experiments derive from an extensive, computational parametric study on the aerodynamic performance of turning vanes conducted by Shah [29]. This section provides a brief overview of his methodologies used in the aerodynamic design of the swirl vanes and their integration into the experimental swirl tube model design to meet the aerodynamic performance requirements in terms of flow turning angle and drag coefficient.

The goal of the aerodynamic performance of the swirl tube was to achieve a drag coefficient of 1.0 based on inlet flow area. The computational study conducted by Shah thus sought to design appropriate swirl vane geometries to produce a steady, streamwise vortex capable of yielding this drag coefficient. The swirl vanes were designed according to the circulation distribution of a Burger vortex with zero turning angle at the vane hubs to higher turning angles at the vane tips. Figure 3.1 adopted from Shah [29] shows this distribution of turning angle through depictions of stacked airfoils.

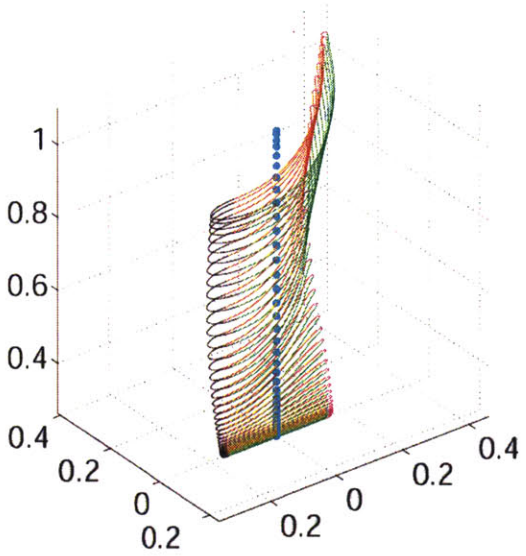

Figure 3.1. Airfoil sections stacked to generate a 3-D vane design. Turning angle varies from zero at the vane hub to higher angles at the vane tip according to the circulation distribution of a Burger vortex. Figure adopted from [29].

To assess the drag generation capability of swirling flows, a parametric study of vane designs producing drag coefficients close to 1.0 was conducted. Drag coefficients of 0.4, 0.6, 0.8, 1.1, and 1.31 were considered in the parametric study, the last two of which were predicted by Shah to exhibit vortex breakdown as described in Chapter 1. Both 2-D inviscid streamline curvature and 3-D RANS CFD computational tools were used iteratively to design sets of swirl vanes with the estimated drag coefficients given above. Empirical measures to determine vane solidity also entered the design process from which solidities of 3 at the tip to 4 at the hub were chosen to ensure proper flow turning through the vane passages (see Chapter 1). Based on swirl vane angle settings ranging between 34° and 64° applied to twenty evenly spaced vanes, drag coefficients were estimated to range from 0.4 to 1.31 using 2-D simulations, tabulated in Table

3.1. One of the goals of the swirl tube experiments is to assess the six vane designs listed in Table 3.1, identified by swirl vane angle setting, for the degree to which they satisfy the drag and noise requirements as well as experimentally assess the relationship between flow-turning angle, drag coefficient, and noise level of swirling flows.

Instead of variable geometry turning vanes, sets of fixed vanes were used to reduce the complexity of the mechanical design. The vane designs mentioned above are incorporated into the mechanical model of the swirl tube by means of visks, defined previously in Chapter 2. The rationale for utilizing visks to test different swirl vane angle settings is discussed in the next section.

Swirl Vane Angle Setting, α	C_D Estimate, MTFlow
34°	0.40
41°	0.60
47°	0.80
53°	1.00
57°	1.10
64°	1.31

Table 3.1. Drag coefficients referenced to inlet area estimated by 2-D inviscid streamline curvature calculations for various swirl vane angle settings [29]. See Table 1.1 for 3-D CFD drag estimates.

3.3 Test Model Design Requirements

The design of the swirl tube test model and its various accessories was largely framed by strict requirements on the versatility and sizing of the test articles. As the goal of the tests is to experimentally assess the aerodynamics and aero-acoustics of swirling flows for quiet drag applications, the model must be adaptable to wind-tunnel testing setup and operating conditions in both aerodynamic and aero-acoustic test facilities, namely the WBWT and QFF, respectively. The model design must also follow firm sizing constraints. That is to say, the model must be as large as possible for noise considerations and manufacturability while remaining small enough to fit in both test facilities. This section presents the requirements imposed on the swirl tube model design and the design choices by which the requirements were satisfied.

3.3.1 Model Versatility

Versatility of the test articles must be manifested in both test configuration and installation capabilities. To best utilize wind-tunnel test time in both the WBWT and QFF facilities for maximum data acquisition, model down time, needed to make configuration changes and/or other adjustments to the test articles, must be minimal. The key criterion for minimizing model down time is a simple mechanical design using few parts that can be quickly and easily

assembled and disassembled. The swirl tube assembly is thus comprised of only 6 parts, joined together using a total of twenty mechanical fasteners (screws):

- Visk: set of turning vanes encased in a revolved shroud with center body through-mount,
- Forward nacelle: revolved, contoured front portion of swirl tube nacelle,
- Rear nacelle: revolved, contoured rear portion of swirl tube nacelle,
- Forward center body: contoured, threaded piece that secures to the visk center through mount,
- Rear center body: contoured, threaded piece that secures to the visk center through mount,
- Support pylon: beam-like, contoured support for swirl tube assembly.

Figure 3.2 shows an exploded view of the swirl tube model, comprised of these six basic parts, discussed in more detail in this section.

As shown in Figure 3.2, the visk is the central component of the swirl tube design, providing connections to nacelle pieces, center body pieces, and the support pylon while housing the turning vanes. The shroud of each visk is designed to mate with both forward and rear nacelle modules by means of circumferential lap joints, each secured by eight flat-head machine screws spaced evenly around the circumference which thread through countersunk holes on the visk periphery into threaded holes on each nacelle lip. The shape of the visk's shroud is defined by the nacelle inner and outer contour: the 2-D cross section of the forward nacelle, aft nacelle, and visk outer shroud. This contour, shown in Figure 3.3 taken from Shah [29], is a carefully designed cambered airfoil 29.2 cm (11.5 in) in length with a 3-to-1 leading edge semi-ellipse and 0.5% thickness-to-chord semi-circular trailing edge. The forward nacelle portion of the airfoil, meant to diffuse incoming flow, has a droop of 5° to prevent separation off of the leading edge, determined by computationally analyzing streamline formations around such semi-elliptical inlets of swirl tubes with 0° of leading edge droop [29]. The rear section of the nacelle profile is slightly drooped such that the flow area from the vane leading edges through the nacelle trailing edge is constant, imposing neither accelerations nor decelerations on the swirling exit flows. The center body contour, also depicted in Figure 3.3, was designed using a 2.5-to-1 leading edge semi-ellipse, sharp pointed trailing edge, and polynomial spline contours between the leading and trailing edges shaped to preserve constant flow area throughout the duct. Both the center body and center section pressure side (underside) of the nacelle profile contain flat sections of constant radius between which the vanes are located, again, to preserve constant flow area throughout the duct.

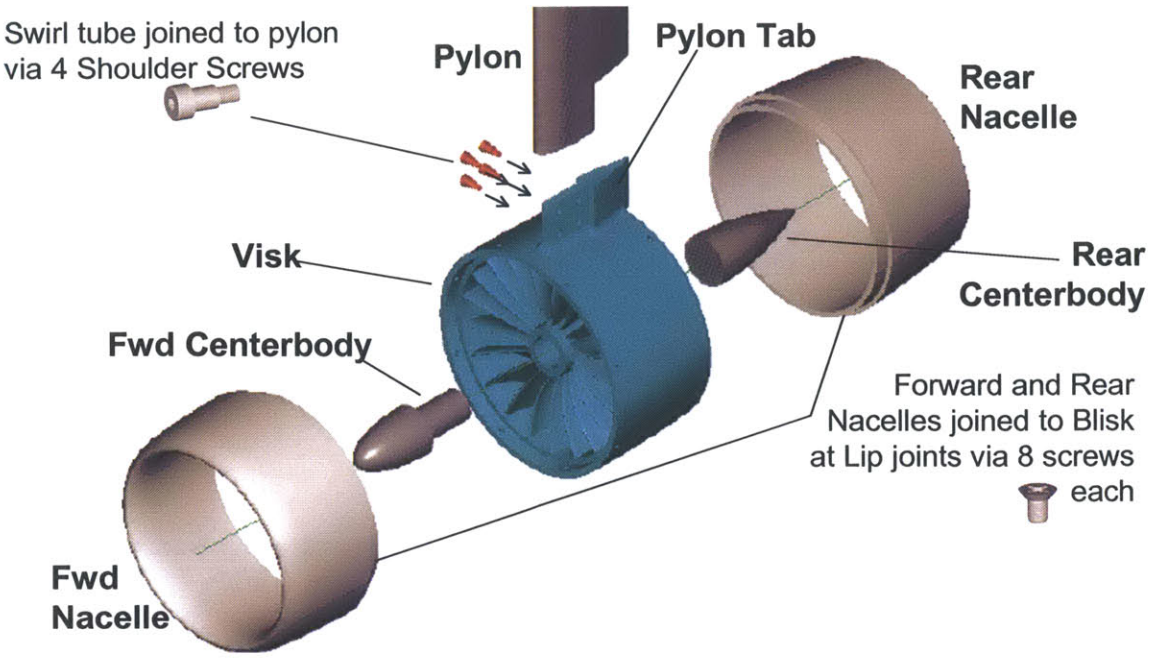

Figure 3.2. Exploded view of swirl tube test model assembly. The six components of the modular assembly are depicted with the central visk in blue. Renderings of pylon and nacelle mechanical fasteners are also included.

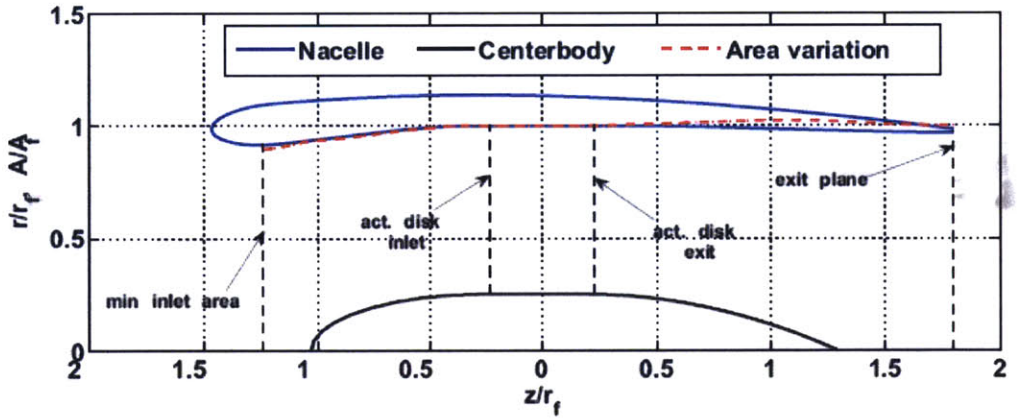

Figure 3.3. Nacelle and center body cross sectional profiles. Nacelle contour is a cambered airfoil constructed with a 3-to-1 leading edge semi-ellipse and semi-circular trailing edge. Flow area ratio relative to nacelle exit, shown by red dashed line, is close to unity at all locations downstream of vanes (actuator disk) to prevent unnecessary acceleration/deceleration of exit flow [29].

Nine visks were fabricated for the experiments. The empty visk (no vanes and thus no center body attachment) provided a means of measuring drag and noise contributions from a stand-alone nacelle with no effects from vanes or swirl. The straight vane visk (0° turning angle) provided a means of measuring drag and noise contributions from vanes (essentially flat plates) contained in a nacelle without the effects of swirl. Drag levels and noise signatures for these two cases could thus be compared against similar data of swirling cases to separate drag contributions

of the nacelle and vanes from those of swirling flows as well as to differentiate acoustic signature characteristics attributable to swirl from those which derive from the presence of nacelle and vane bodies. The remaining six visks, the swirl cases, yield swirl vane setting angles of 34°, 41°, 47°, 53°, 57°, and 64°, as discussed above. The range of turning angles was chosen to encompass both stable, steady vortex cases (max turning angles < ~50°) and vortex breakdown cases (max turning angles > ~50°) as predicted by Shah's computations, described in Section 1.3 [29]. Comparative photos of the visks are shown in Figure 3.4. The photos in Figure 3.4 show the visual differences between the visks, most evident near the vane hubs where the viewer can see through large, radial, wedge-shaped sections of lower swirl cases (i.e. 34°, 41°) but significantly smaller wedge sections of high swirl cases (i.e. 57°, 64°). By fabricating each of these nine visks as a single unit, changing swirl angles is a simple matter of exchanging visks within the full swirl tube assembly.

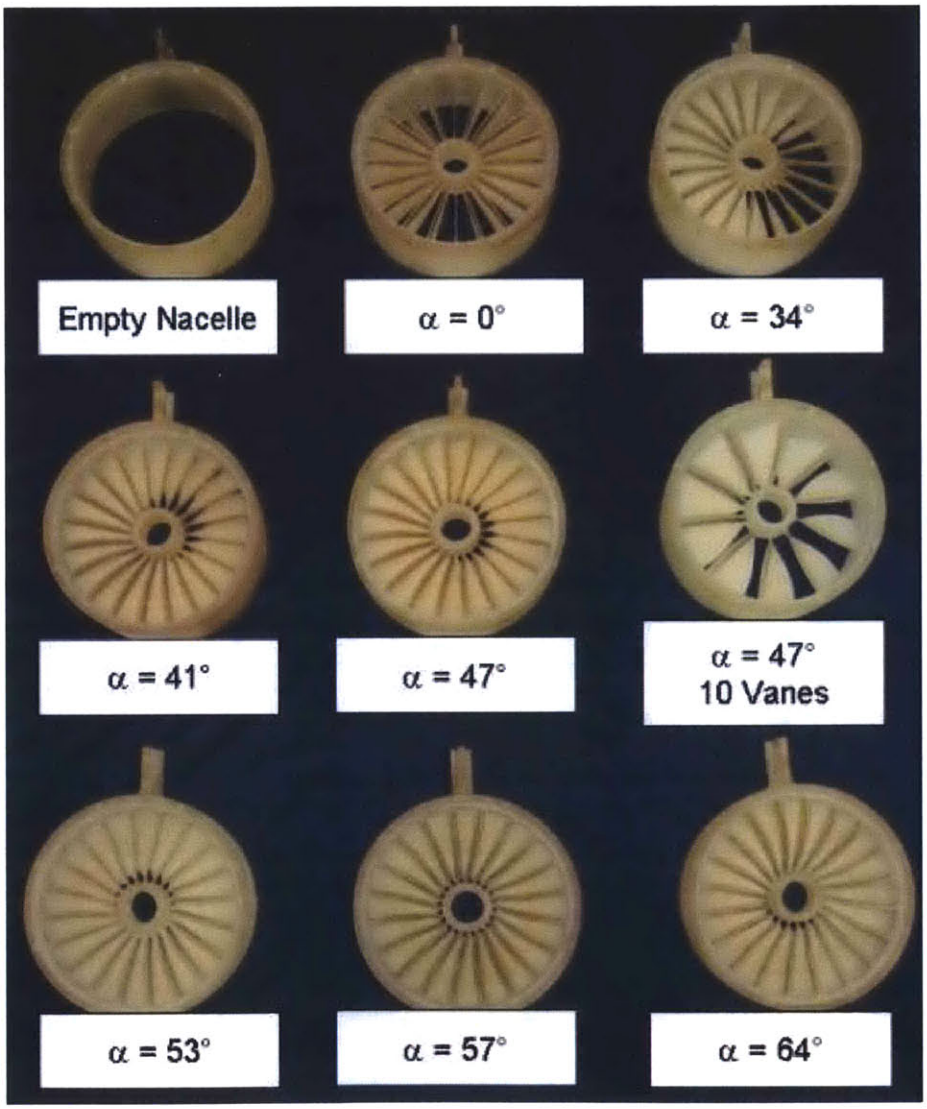

Figure 3.4. Nine visks used in the experimental testing of the swirl tube. Visual differences between low swirl cases (i.e. 34°, 41°) and high swirl cases (i.e. 57°, 64°) are most apparent at vane hubs.

For testing in the WBWT and QFF, the swirl tube model must be adaptable to wind tunnel testing setup and operation conditions in both test facilities. Given the stark differences in operations and setup between the WBWT and QFF (large closed loop tunnel versus vertical free jet in an anechoic chamber, respectively, see Chapter 2), the test articles were designed to adapt to installation and testing conditions at both wind tunnels. The exploded model view in Figure 3.2 shows each visk outfitted with a single attachment point: the pylon tab. This single tab allows each swirl tube configuration (visk) to connect to support pylons specific to the facility via a 4-screw, tab and pocket joint. For testing in the WBWT, the model was mounted horizontally, supported from its underside as shown in Figure 2.3. The requirements of the WBWT model pylon were to (1) avoid aerodynamic interference of flows around the bulky base of the model support shaft (depicted in Figure 2.3) and (2) safely transmit the loads experienced by the model. Aerodynamic interference from the support shaft base was determined to be negligible when separating this base from the swirl tube with a pylon length greater than the 20.3-cm swirl tube diameter (8 in). A fundamental structural analysis of loading conditions and part geometries as described later in Section 3.5 verified the pylon design's ability to safely transmit all critical loads on the swirl tube.

Testing at the QFF required a pylon capable of supporting the model in a vertical-mount position from its side (Figure 2.5). In addition to supporting the model structurally and preventing aerodynamic interference effects from other physical bodies (i.e. support wall), the QFF pylon was designed to not interfere acoustically with the swirl tube. That is to say, the acoustic signature generated by the pylon should have characteristics that are distinctly different in amplitude and frequency than those expected from swirling flow cases and other components of the assembly, such as the nacelle. This was ensured by shaping the pylon cross-section to match that of a standard NACA 0022 airfoil, the noise signature of which can be estimated using existing trailing edge noise correlations and has been experimentally estimated by previous testing of a similar symmetric airfoil, the NACA 0012, at the QFF [5]. Figure 3.5 shows experimentally measured NACA 0012 noise signature data with 30.48 cm (12 in) chord (similar to swirl tube nacelle chord) in one-third octave with acoustic signatures of the NACA 0022-based pylon and swirl tube nacelle profiles. These were computed using semi-empirical trailing-edge noise predictions based on Ffowcs Williams-Hall methods [9], which were derived by Goldstein [11] and adapted by Lockard and Lilley [21], all rooted by Lighthill's acoustic analogy [14, 19, 20]. The estimated nacelle profile and pylon NACA 0022 spectral peaks are separated by ~2.5 kHz in frequency and 7 to 8 dB in sound pressure level (SPL), distinctly different from each other (i.e. they do not overlap). Since the calculated acoustic signature of the pylon shows distinctly different spectral peaks than those estimated for the nacelle, it is inferred that the actual pylon noise signature will neither mask nor be masked by acoustic signatures of the swirling flow cases. The spectra of Figure 3.5 also imply that the trailing edge noise predicted for the pylon and nacelle components is very close to the background noise level of the QFF. Thus to extract acoustic spectral features that are potentially at or below the background noise level, microphone array measurement techniques are employed, as described in Chapter 2.

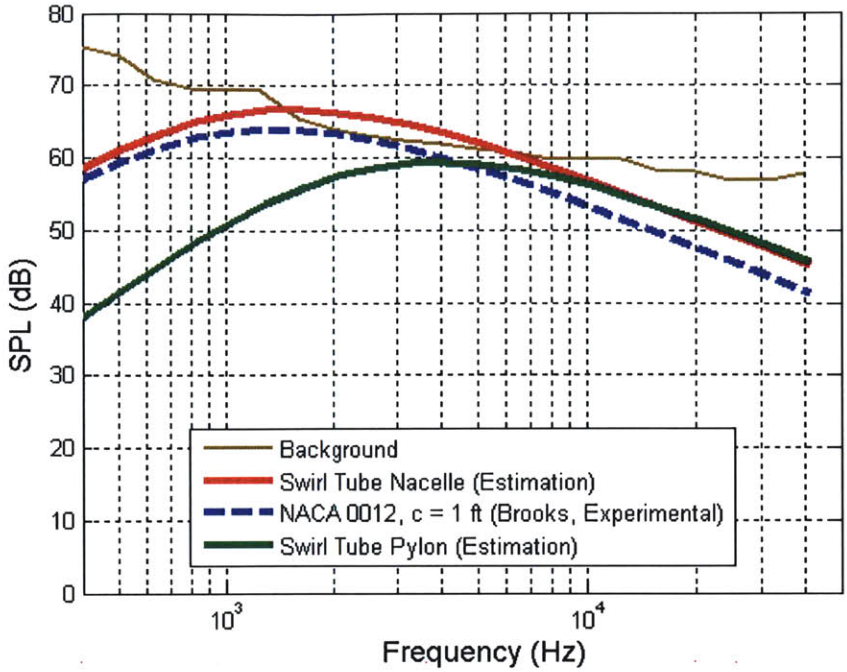

Figure 3.5. Estimated and experimentally measured noise signatures of nacelle, NACA 0022 pylon, and NACA 0012 profiles [5] presented in one-third octave bandwidth. Pylon and nacelle spectra peaks are distinct in terms of peak frequency and amplitude, suggesting pylon noise will not mask the experimentally measured noise signatures of the empty nacelle and swirl cases.

3.3.2 Sizing

The swirl tube model was sized to balance the requirements of the test facilities with the restrictions set by fabrication tolerances. Sizing constraints based on the test facilities focused only on requirements imposed by the QFF, since the dimensions of the free jet flow area in the QFF, 0.61 m x 0.91 m (2 ft x 3 ft), impose more constraint on model sizing in terms of model installation than the large 2.13 m x 3.05 m (7 ft x 10 ft) elliptical test-section area of the WBWT (see Chapter 2). Obtaining good signal-to-noise quality of the swirl tube noise signature to the background noise of the QFF during tunnel operation was also a determinant of model sizing, as larger test articles produce noise signatures at lower frequencies and higher noise levels than identical test articles constructed at smaller scale. The balance of these QFF-related sizing constraints along with those set by fabrication tolerances are discussed in detail below, the results of which became the final swirl tube dimensions: 29.2 cm (11.5 in) length, 20.3 cm (8 in) maximum diameter.

Constraints on the maximum dimensions of the swirl tube model design were determined such that the model, the flow around the nacelle (spillage), and as much of its exhaust as possible, the target of the QFF acoustic measurements, would remain within the free jet's potential core. Potential cores are zones of uniform flow bounded by turbulent shear layers at the interfaces of the jet flow and the surrounding stagnant or low-velocity flow. It is critical that flows entering the tube and surrounding both it and its exhaust reside within the potential core (i.e. they are uniform) in order to accurately simulate the effects of swirling flow generated in uniform free

stream conditions. At Mach numbers less than 0.2 [13], encompassing Mach numbers utilized in this series of experiments, the potential core length is typically 4 to 5 times the diameter of the jet. Thus for the QFF's 0.61 m x 0.91 m (2 ft x 3 ft) vertical free jet, a conservative estimate of the potential core length of 2.44 m (8 ft) was considered. Figure 3.6 shows the model positioned within the potential core of the QFF free jet. The swirl tube nacelle inlet sits 0.72 m (2.38 ft) downstream of the wind tunnel free-jet exit to avoid effects of upstream influence of the swirl tube inlet on free-jet exit flow while remaining far enough forward to keep a length of exit flow more than four times the nacelle exit diameter within the potential core bounds. Figure 3.5 also shows the resulting spillage estimation around the swirl tube nacelle in terms of exponentially decaying potential field. The potential field surrounding the nacelle is zoned according to the local streamline displacement perpendicular to undisturbed tunnel flow direction as a fraction of nacelle inlet radius, R_{in}, as computed by 2-D streamline curvature code. The zone denoted "Considerate," containing streamline displacements exceeding $0.15R_{in}$ and extending radially outward $1.67R_{in}$ from the swirl tube axis of symmetry, remains just inside the QFF free-jet potential core at the nacelle exit plane based on a nacelle diameter of 20.32 cm (8 in). Since the radial extent of this zone grows with increasing nacelle diameter, keeping this zone within the bounds of the potential core limits the maximum nacelle diameter to 20.32 cm (8 in).

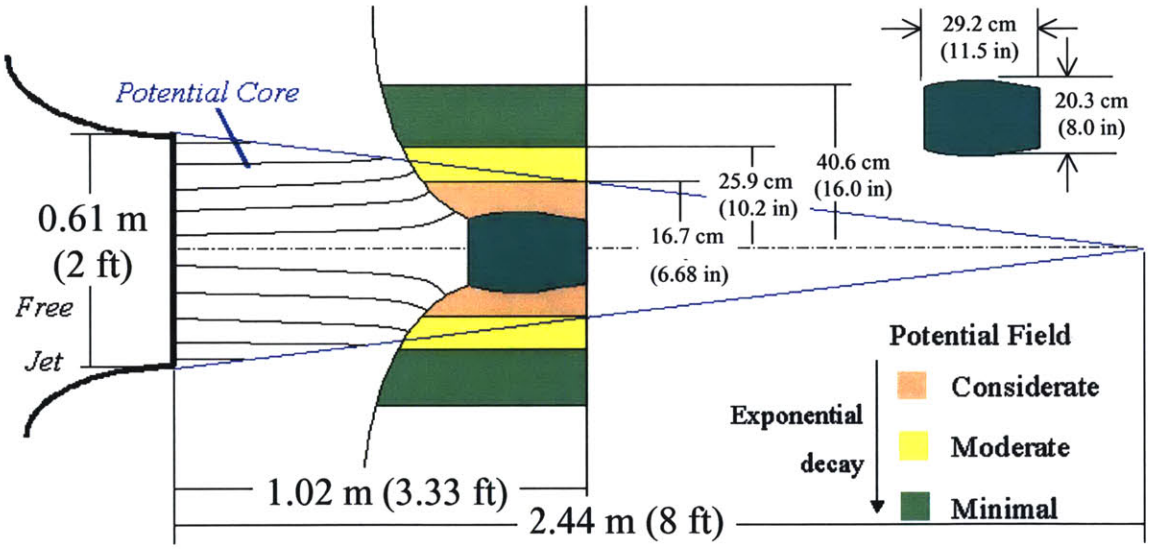

Figure 3.6. Swirl tube position relative to estimated QFF free jet potential core. Zone of considerate streamline displacement perpendicular to undisturbed tunnel flow direction is contained fully within potential core given a 20.3 cm (8.0 in) swirl tube maximum diameter, suggesting most of the swirl tube spilled flow will not coincide with the free jet shear layer.

The sizing of the model was also based on obtaining good signal-to-noise quality of the swirl tube noise levels relative to the background noise levels of the QFF during tunnel operation. Since empirical estimates for noise levels of swirling flows do not exist, it was assumed that good signal-to-noise quality for swirl cases would be obtained for a given set of swirl tube dimensions if the noise signature of the baseline empty nacelle case (no vanes, no center body, thus quieter than swirl cases) was measurable above QFF background noise levels. Though

phased microphone arrays, like the MADA array of the QFF discussed in Chapter 2, have the capability of detecting noise sources up to 10 dB below background noise level, good signal-to-noise quality of the empty nacelle relative to background noise level was still sought to maximize the noise source detection potential of the phased array. Utilizing the same empirical trailing edge noise predictions as used in Section 3.3.1 [14], Figure 3.7 shows that nacelle chords between 15.2 cm (6 in) and 29.2 cm (11.5 in) in length are above the QFF background noise spectrum by up to 5 dB. As nacelle chord increases above 45.7 cm (18 in), spectral peaks shift to lower frequencies, where the nacelle trailing edge noise signatures do not peak above background noise levels (i.e., nacelle trailing edge noise would not be measurable). Similarly, nacelle chords less than 10.2 cm (4 in) fail to peak above background noise levels. Thus good signal-to-noise for swirling cases is assumed for nacelle chords between 15.2 cm (6 in) and 29.2 cm (11.5 in) in length, marked by the dashed blue and solid black curves in Figure 3.7.

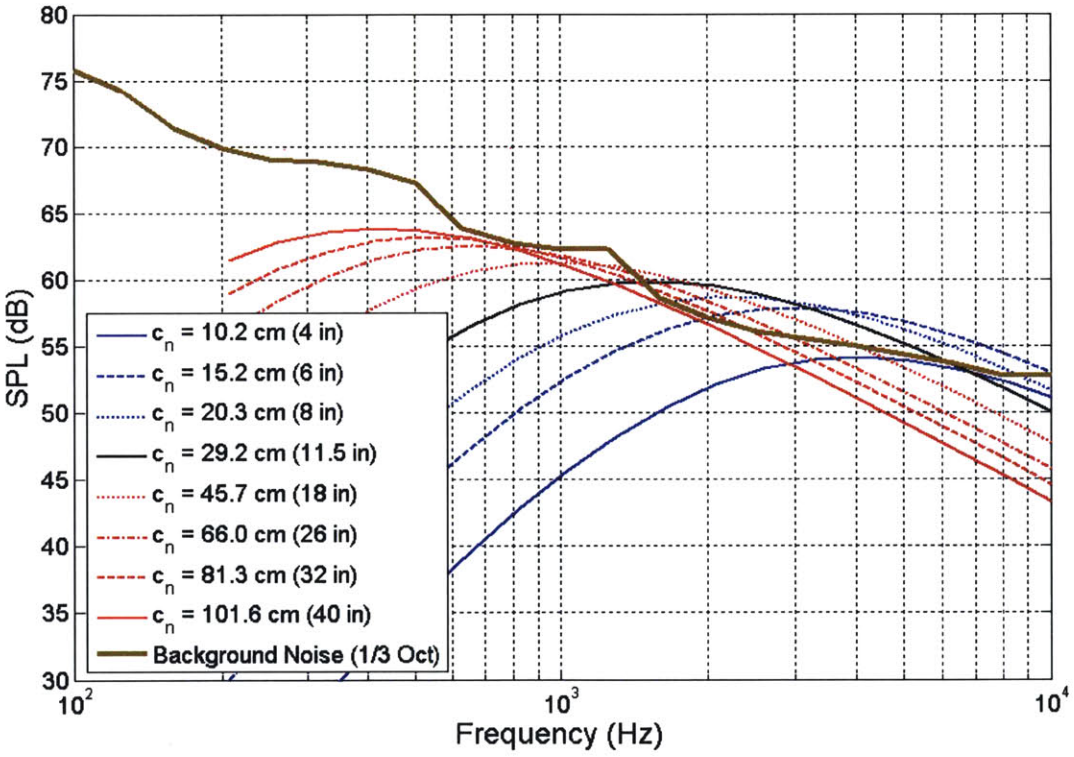

Figure 3.7. Computed spectra of nacelle profiles of various chord lengths relative to QFF background noise. Good signal-to-noise for swirling cases is assumed for nacelle chords between 15.24 cm (6 in) and 29.2 cm (11.5 in) in length since these cases yield spectral peaks above background noise level.

Fabrication limitations restricted the minimum sizing of the swirl tube. The stereolithography process, used to fabricate the visks and detailed later in Section 3.4.1, imposes a minimum wall thickness of 0.05 cm (0.02 in), thus setting the minimum dimension of the swirl tube model, the vane trailing edges. By appropriately scaling the model given the vane trailing edge dimension set by tolerance restriction, the minimum swirl tube diameter was determined to be 20.3 cm (8

in), equal to the maximum diameter required by QFF potential core considerations determined at the beginning of this section.

Taking into account sizing requirements imposed by QFF potential core restrictions, QFF signal-to-noise, and fabrication tolerances, the test model was sized 29.2 cm (11.5 in) in length and 20.3 cm (8 in) in maximum diameter. Figure 3.8 shows a three-view dimensioned layout of the final design of the swirl tube.

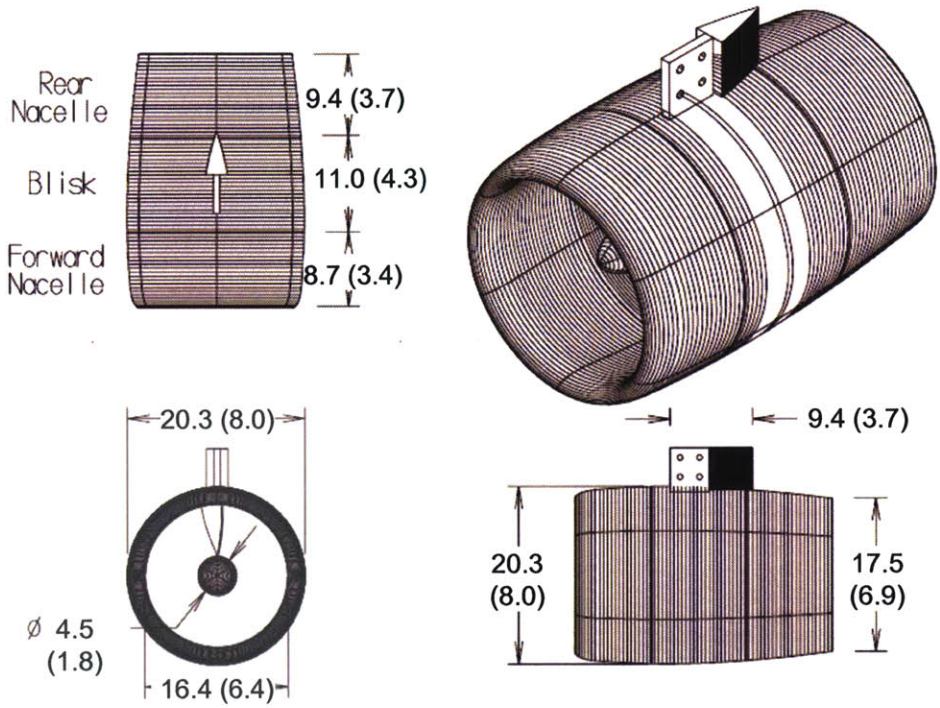

Figure 3.8. Dimensioned three-view layout of swirl tube test model. Primary dimensions are given in centimeters outside parenthesis with inch equivalents inside parenthesis.

3.4 Part Fabrication

The selections of appropriate materials and fabrication options for the swirl tube parts were determined by material strength and manufacturability. Choosing materials with yield strengths incapable of supporting the aerodynamic and structural loads on the model could result in structural failure of the swirl tube during wind tunnel testing. Appropriate selection of the fabrication method is equally important. For example, fabrication processes that are limited by part complexity or fine tolerances could not be used to manufacture visks, parts which are highly complicated in terms of geometric detail. This section describes the selections of materials and fabrication methods for all swirl tube parts and accessories.

3.4.1 Material Selection and Fabrication Method of Visks

Fabrication of the visks required a process able to produce numerous high-quality parts with highly complex, unique geometries. Precision of the process required thickness of walls as small as 0.05 cm (0.02 in) to create adequately rounded, clean vane trailing edges. For its quality of finish, detailed precision, and consistency in creating large quantities of identical parts, stereolithography, or SLA (StereoLithography Apparatus), was chosen as the method of visk fabrication.

Stereolithography begins with a detailed three-dimensional CAD part design, which is computationally "sliced" into layers approximately 0.13 mm (0.005 in) thick in a particular direction (the stacking direction). Beginning with the bottom layer, a thin laser beam traces the geometry of the layer in a vat of liquid plastic photopolymer ~0.13 mm (0.005 in) thick, solidifying the liquid plastic it traces. Once a layer is completed, the machine bed holding the newly hardened layer descends by a layer thickness, allowing more liquid to gather above. The laser traces the next layer, which hardens and welds onto the first. The process repeats until the full part is formed, after which a number of surface smoothing finishes can be applied.

The visks were fabricated via SLA methods by Solid Concepts, Inc. (Valencia, CA). A strong, lightweight ABS-type plastic, SOMOS 11120, was selected as the building material for its high yield stress of 47 MPa (6,831 psi) and its low density of 1,191 kg/m^3 (2.31 slugs/ft^3), as given in Table 3.2. The structural analysis described in Section 3.5 confirmed that this material is strong enough to accommodate the structural loads of the experiment.

Material	Material Type	Used To Fabricate	Yield Stress, σ_{yield}	Density
SOMOS 11120	ABS Thermoplastic Polymer	Visks	47 MPa (6,831 psi)	1,191 kg/m^3 (2.31 slugs/ft^3)
Aluminum Alloy	Alloy T6061	Nacelles, Centerbodies, Pylons	241 MPa (35,000 psi)	2,701 kg/m^3 (5.24 slugs/ft^3)
Stainless Steel	Austenitic Ferrous Metal	Mechanical Fasteners	552 MPa (80,000 psi)	7,468 kg/m^3 (14.49 slugs/ft^3)

Table 3.2. Material properties of various swirl tube components.

3.4.2 Material Selection and Fabrication Method of Nacelles, Center Bodies, and Pylons

For its high yield strength of 241 MPa (35,000 psi), standard aluminum alloy T6061 was used in the fabrication of the forward and rear nacelle and center body pieces, support pylons, and

variation accessories (see Table 3.2). A photo of the metalwork equipment is shown in Figure 3.9.

The forward and rear nacelle and center body pieces were turned on CNC (computer numerically controlled) lathes at the MIT Central Machine Shop to tolerances within 0.13 mm (0.005 in). Three sets of center bodies were manufactured, one set of which was drilled through to provide a 9.5 mm (0.375 in) through-hole. This through-hole center body was utilized as a means of anchoring accessory parts, such as inlet distortion screens used for simulating upstream flow non-uniformity entering the swirl tube. Two inlet distortion accessory plates were fabricated at the NASA Langley QFF: a blade wake simulator disk and a perforated distortion wedge. Both of these accessories attached to the periphery of the nacelle inlet and were secured in place by means of a threaded support rod connected to the through-flow center body assembly. More discussion on the purpose, implementation, and results of swirl tube configurations with inlet distortion screens is detailed in Chapters 4 and 5.

The MIT Central Machine Shop also fabricated the QFF pylon by means of automated 3-axis CNC milling. Fabrication of the WBWT pylon was conducted in house and kept simple, utilizing pre-sized 10.2 cm x 1.9 cm (4 in x 0.75 in) bar stock and 11.4 cm (4.5 in) rounds to provide adequate support to the model. Aerodynamically shaped bass wood moldings provided clean leading and trailing edges to the pylon.

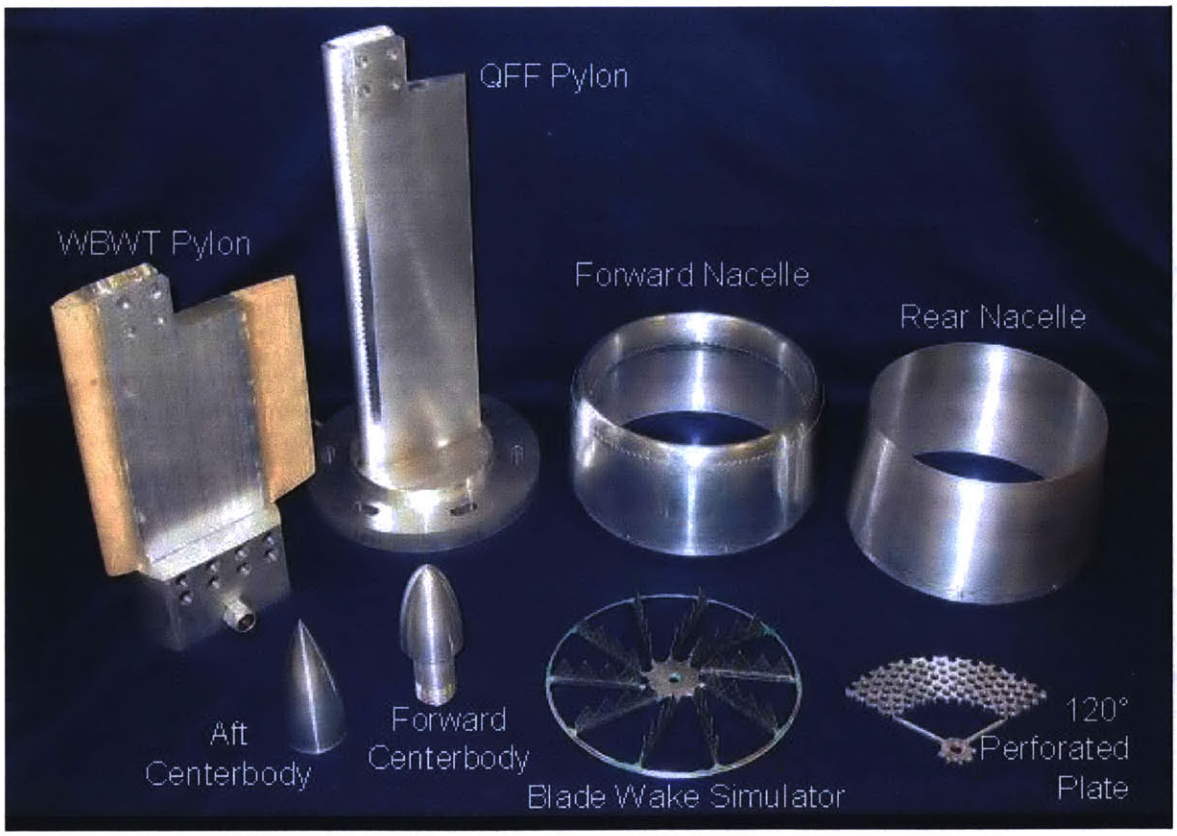

Figure 3.9. Nacelle, centerbody, support pylons, and accessory swirl tube equipment. Parts shown are fabricated from aluminum alloy T6061 via CNC lathe, CNC mill, or conventional metal machining methods.

3.5 Structural Integrity of Test Model

The final step in the mechanical design of the swirl tube test model was to conduct a full structural analysis to ensure the model's ability to safety carry the aerodynamic and structural loads during all phases of testing without danger of structural failure. Structural deformation leading to material failure occurs when local loads exceed the yield strength of the material through which the loads are transmitted. To prevent failure, safety factors are introduced, defined as the ratio of the material yield stress to the maximum allowable stress.

$$SF = \frac{\sigma_{yield}}{\sigma_{allowable}} \tag{3.1}$$

The structural analysis outlined below utilizes fundamental structures theory, including bending moment and shear force analyses, plate and beam theories, and consideration of stress concentrations. The goal of the analysis is to calculate all forces and moments acting on the swirl tube model and supports, identify critical structural locations, calculate local stresses and/or stress concentrations at these critical locations, and validate that these stresses are less than maximum allowable stresses as defined by material yield stresses and safety factors. As confirmed by the following analysis and validated by wind-tunnel testing of the swirl tube test model, the swirl tube test model design is structurally sound with safety factors greater than or equal to 1.5.

3.5.1 Forces and Moments

The structural analysis considered the maximum loading conditions: free stream flow with Mach number, M, equal to 0.2. Figure 3.10 shows loading diagrams of the model loaded in both test facility installation orientations, and includes the swirl tube drag force, D, the pylon drag force, D_{py}, the swirl tube weight, W_{st}, and the pylon weight, W_{py}. The drag force on and the weight of the pylon are modeled as distributed loads given the long, slender, beam-like geometry of the part. Using a simplified control volume momentum analysis with no swirl, the net swirl tube drag is equal to the difference between the drag force, D, and an inlet suction force, F_s, induced by streamline curvature, as given by:

$$C_D = \frac{D - F_S}{\frac{1}{2}\rho u_\infty^2 A} = \left[1 - \left(\frac{u_1}{u_\infty}\right)^2\right] - \left(1 - \frac{u_1}{u_\infty}\right)^2, \tag{3.2}$$

where the first term on the right side represents the total swirl tube drag coefficient, the last term on the right hand side represents the inlet suction drag coefficient, u_∞ and u_1 are velocities in the free stream and at the turning vane leading edges, respectively, and A is the drag reference area, here equal to the swirl tube frontal area (0.03 m^2, 0.35 ft^2) [13]. The inlet suction drag coefficient, $C_{D,Fs}$, is found to equal one-quarter the drag coefficient of the swirl tube, C_D, by taking the ratio of the last two terms on the right side of Equation 3.2 and assuming a velocity ratio u_1/ u_∞ of 0.6 from the predicted Mach number distribution shown in Figure 1.4a for the stable 47° swirl.

In order for the device to yield a maximum net drag coefficient of 1.31 (highest estimated by Shah for visks fabricated for these experiments [29]), the difference of the swirl tube and inlet suction drag coefficients must be equal to 1.31. Thus, the swirl tube drag coefficient, equal to the sum of the net swirl tube drag coefficient and the inlet suction drag coefficient, is found to be 1.75.

$$\begin{aligned} C_D - C_{D_{Fs}} &= C_{D_{NET}} \\ C_D - 0.25C_D &= 1.31 \\ C_D &= 1.75 \end{aligned} \tag{3.3}$$

At $M = 0.2$, the swirl tube experiences a drag force of 160.2 N (36.02 lbs), calculated using the definition of drag coefficient given in Equation 3.4,

$$D = \frac{1}{2}\rho_\infty u_\infty^2 C_D A, \tag{3.4}$$

where ρ_∞ is the free stream air density, u_∞ is the free stream flow velocity, and A is the drag reference area, here equal to the swirl tube frontal area (0.03 m^2, 0.35 ft^2). The inlet suction force, F_s, is thus equal to 40.1 N (9.01 lbs).

The loading diagrams in Figure 3.10 also show swirl moment, M_s: the torque imposed on the swirl tube caused by turning the flow. The moment M_s is defined in Equation 3.5 as the integrated product of angular momentum, rv_θ, and mass flow rate, $\dot{m} = \rho v_x A$.

$$M_S = \int r v_\theta d\dot{m} = \int \rho r v_x v_\theta dA, \tag{3.5}$$

Results from Shah's 2-D streamline curvature analysis of a high swirl case include normalized axial and tangential velocity radial profiles, v_z/v_∞ and v_θ/v_∞ as well as the normalized local density radial profile, ρ/ρ_∞. The density radial profile is important to include given the presence of compressibility effects in the core region ($r \sim 0$), since Mach numbers in the core can reach close to 0.4. The product of these normalized quantities, multiplied together with the quantity r/R, is plotted in Figure 3.11, which shows the normalized radial swirl moment distribution to have an upper bound at 0.52. Thus for simplicity, the quantity $\rho r v_x v_\theta$ in the Equation 3.5 can be replaced with the conservative estimate $0.52\rho_\infty R v_\infty^2$. Substituting this conservative estimate into Equation 3.5 yields

$$M_S = 0.52\rho_\infty v_\infty^2 R \int dA. \tag{3.6}$$

Integrating over the turning vane annular area defined in θ from 0 to 2π and in r from $0.25R$ to R, the swirl moment M_s is calculated to be 6.18 N-m (4.56 ft-lbs).

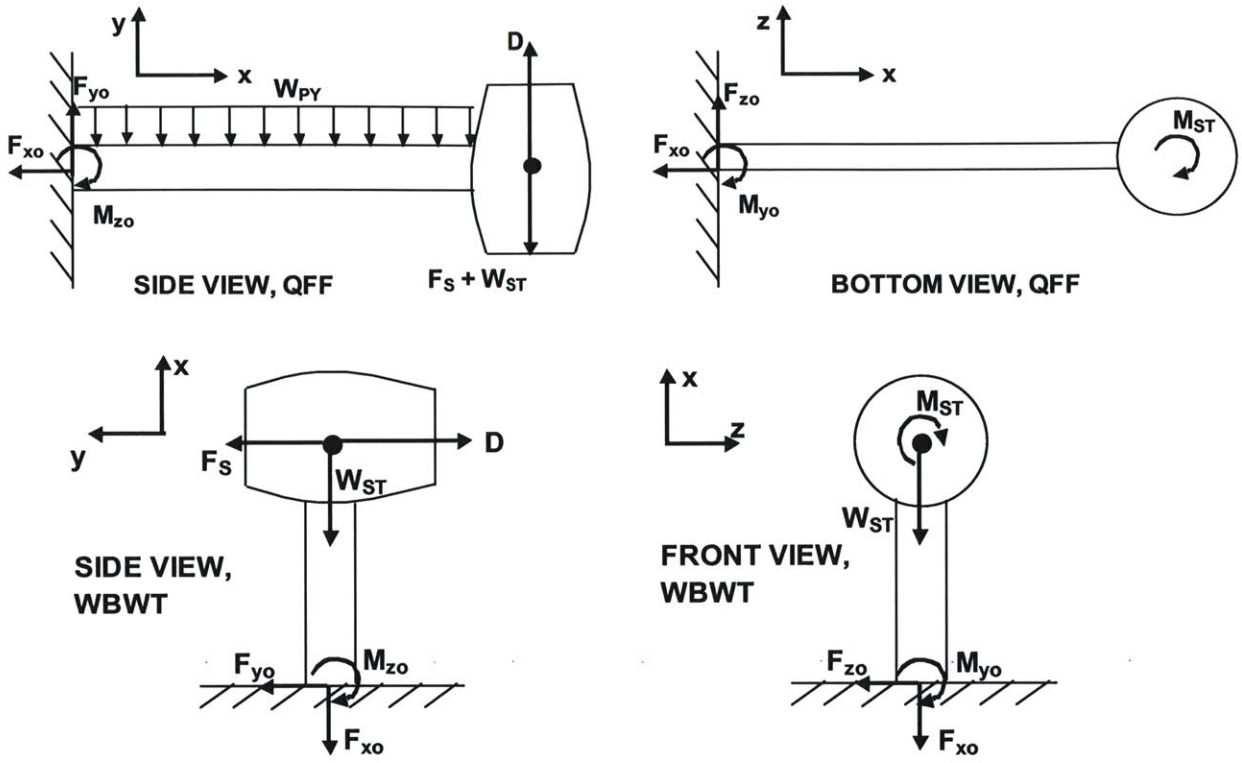

Figure 3.10. Loading diagrams and reaction forces and moments for the swirl tube mounted in QFF (top left and right) and WBWT (bottom left and right). Pylon drag, negligible in both cases, is not included in the figures.

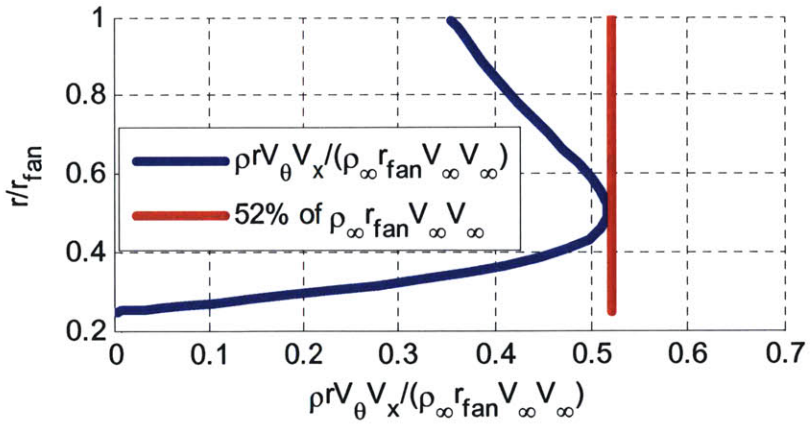

Figure 3.11. Normalized radial loading distribution (blue) and constant loading distribution (red) on a single swirl vane. Swirl moment, M_S, is calculated using the constant loading distribution (red) for simplicity.

3.5.2 Critical Structural Locations with Stress Concentrations

Having calculated all the forces and moments on the swirl tube in $M = 0.2$ free stream flow, the next step in the structural analysis is the identification of structural locations with critical stress

concentrations. Critical structural locations are defined as portions of the swirl tube model where the local structural stresses are increased. Assuming all parts are made of homogenous materials, locations are likely to be structurally critical where cross-sectional area is small, where sharp corners giving rise to stress concentrations exist, and where part joints occur. Considering these conditions for likely critical structural locations, four critical structural locations were identified: the turning vane-shroud junctions, nacelle-visk joints, the pylon tab, and the pylon-wall junction. Local stresses and safety factors imposed at each of these critical structural locations are summarized in Table 3.3.

Critical Structural Location	**Fillet Radius,** r_{fillet}	**Maximum Nominal Stress,** $\sigma_{nominal}$	$\sigma_{nominal} / \sigma_{yield}$	**Imposed Safety Factor**
Turning Vane Hubs	1.3 mm (0.05 in)	10.5 MPa (1,526 psi)	0.22	1.5
Nacelle-Visk Joints: Hole Compression	--	0.65 MPa (94.1 psi)	0.01	4.0
Nacelle-Visk Joints: Screw Shear	--	0.95 MPa (137.8 psi)	1.2×10^{-5}	4.0
Pylon Tab Stresses	7.6 mm (0.3 in)	37.4 MPa (5,431 psi)	0.80	4.0
Pylon Tab: Screw Compression	--	2.4 MPa (348.5 psi)	4.4×10^{-3}	4.0
Pylon Tab: Screw Shear	--	1.9 MPa (275.2 psi)	3.4×10^{-3}	4.0
Pylon-Wall Junction	--	8.1 MPa (1,177 psi)	0.03	4.0

Table 3.3. Fillet radii, nominal stresses, and safety factors of critical structural locations. Minimum QFF-required safety factor of 4.0 is met at all critical structural locations with the exception of turning vane hubs. Nominal stresses at all critical locations are well below material yield stresses.

3.5.2.1 Stress Analyses at Turning Vane-Shroud Junctions

The swirl moment, M_S, is transmitted to the swirl tube structure via load distributions per turning vane, q. The load distribution is assumed constant across the vane span, equal to a load value greater than the maximum of the actual load distribution, and was found to be 93.8 N/m (6.43 lbs/ft) using a conservative estimate of normalized profile quantities similar to that used to calculate the swirl moment, M_S. A detailed description of these calculations is found in Appendix A. As depicted in the vane loading free body diagram of Figure 3.12a, the load distribution, q, can be used to calculate the reaction moments, M_{rxn}, at the vane hub and tip. To solve the statically indeterminate problem, the method of superposition is employed, which utilizes the sum of solutions to three simpler beam loading scenarios to solve the initial, more complicated problem. Here, the complete vane loading shown in Figure 3.12a is modeled as a combination of simpler cantilevered beam problems, which each achieve static determinacy under simple, single applied load conditions. Figures 3.12b, 3.12c, and 3.12d show the three different cantilevered beam problems: the first with the distributed load only, the second with the tip force only, and the third with the tip moment only. On its own, each of these sub-scenarios would yield a tip deflection, δ, on the right end due to the loads on the beam (vane). For the solutions of the three cantilevered sub-cases to sum to a clamped-clamped case solution, the sum of the individual deflections must equal zero.

$$\delta_b + \delta_c + \delta_d = 0 \tag{3.7}$$

The solutions for the individual tip deflections δ_b, δ_c, and δ_d are common solutions to standard cantilevered beam deflection problems using second-, third-, and fourth-order deflection curve differential equations. Gere [10] obtains the following solutions using these methods.

$$\delta_1 = \frac{-qL^4}{8EI}, \quad \delta_2 = \frac{FL^3}{6EI}, \quad \delta_3 = \frac{-M_{rxn}L^2}{2EI} \tag{3.8}$$

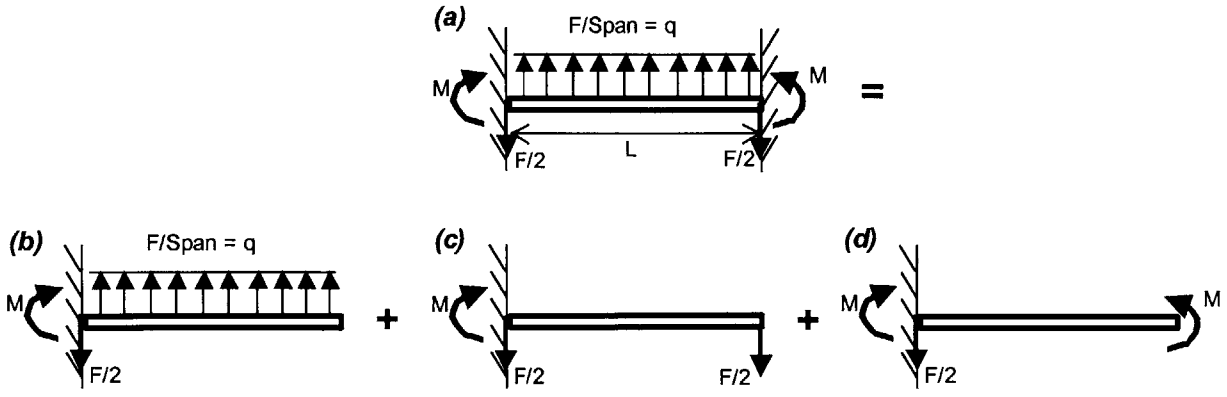

Figure 3.12. Subdivision of loads on a statically indeterminate turning vane (a) through the method of superposition of cantilevered beams with (b) a distributed load, (c) a tip load, and (d) a tip moment. Solutions to the three cantilevered cases sum to represent that of the original clamped-clamped case (a) by setting the sum of tip deflections for cases (b), (c), and (d) equal to zero.

Combining these solutions and solving for the reaction moment, it follows that

$$M_{rxn} = \frac{qL^2}{6} = 0.07 \textbf{ N-m } (0.59 \textbf{ in-lbs}). \tag{3.9}$$

Reaction moments occur at both the hub and tip of each turning vane. These moments give rise to stresses, as determined by the structural flexure formula given in Equation 3.10,

$$\sigma_{c/s} = -\frac{M_{rxn} \cdot t_{c/s}}{I_{c/s}} \tag{3.10}$$

where the subscript *c/s* denotes "cross section" of the vane hub or tip, $t_{c/s}$ is the thickness of cross section *c/s*, and $I_{c/s}$ is the moment of inertia of cross section *c/s*. From Equation 3.10, the stresses at the hub and tip were found to be 7.01 MPa (1,017 psi) and 0.52 MPa (75 psi), respectively; thus, the location of concern is the vane hub. With the local stress computed at the vane hub, one would typically calculate the safety factor based on material yield stress: e.g for SLA, σ_{yield} = 47 MPa (6,831 psi), so SF = 6.71. In this situation, however, the calculated stresses of the vane hub and tip occur near sharp corners where the vanes join the outer shroud and inner center body connector at right angles. These sharp geometric transitions give rise to local stress concentrations, which can be significantly larger than the nominal stresses calculated and thus must be carefully considered before computing an accurate safety factor. The stress concentration factor, *K*, is defined as the ratio of the actual stress to the nominal stress.

$$K = \frac{\sigma_{actual}}{\sigma_{nominal}} \tag{3.11}$$

Since the actual material stress cannot exceed the material yield stress, K_{max} is defined as the ratio of the material yield stress to the nominal stress.

$$K_{\max} = \frac{\sigma_{yield}}{\sigma_{nominal}} \tag{3.12}$$

Fillets, material added to sharp inside corners to smooth the geometric transition from one wall to an adjacent wall, help to alleviate stress concentrations by eliminating the sharp corners at which stress concentrations proliferate. The size of the fillet, namely the fillet's radius, determines the degree to which the stress concentrations are reduced. Fillet radii are frequently estimated by empirical methods using local geometry and acceptable stress limits. Roark and Young [32] use empirically derived, third order polynomials to approximate the stress concentration factor, *K*, the procedure for which is described in more detail in Appendix B. The fillet radius is appropriately sized to subdue the local stress concentrations if the stress concentration factor *K* is less than its maximum allowable value, K_{max}. For example, a fillet radius of 1.3 mm (0.05 in) applied to the geometry of the vane hub given in Figure 3.13 yields an estimated stress concentration *K* = 4.471. To consider this fillet radius of 1.3 mm (0.05 in) appropriately sized, the maximum allowable stress concentration, K_{max}, must be greater than *K* =

4.471. Given this constraint on K_{max}, the maximum nominal stress, $\sigma_{nominal}$, can be computed using Equation 3.12. Computing this value to be 10.5 MPa (1,526 psi) establishes a vane hub stress safety factor of 1.5. Raising this safety factor further by increasing the fillet radius is limited by the small quarter-inch spacing between turning vanes at the hubs; fillet radii that are too large would significantly reduce the flow area of the vane passages at the hub. While small as compared to other safety factors determined in this structural analysis, this safety factor still provides a sufficient buffer between the stresses experienced at the vane hubs and the material yield stress of SOMOS 11120.

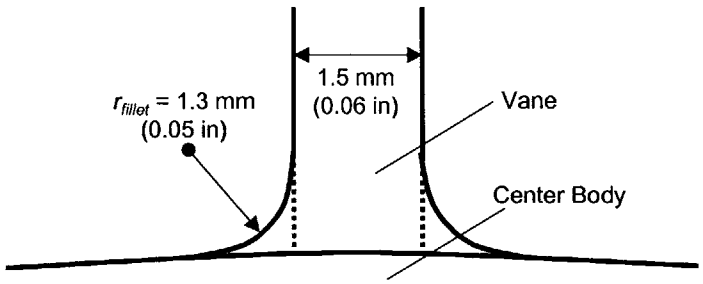

Figure 3.13. Turning vane hub fillet geometry. Increasing the fillet radius further would significantly reduce the flow area of the vane passages at the hub, thus limiting the vane hub stress concentration safety factor to 1.5.

3.5.2.2 Stress Analyses at Visk-Nacelle Joints

The next critical structural locations considered in this analysis are the circumferential lap joints where the visk joins both the forward and rear nacelle pieces. Eight screws secure each of these lap joints radially and are spaced evenly around the circumference of the joints. In the QFF (swirl tube positioned vertically), these fasteners transmit the weight of the forward nacelle as well as the inlet suction force to the visk. This creates compressive and shear stresses on the screws, forward nacelle holes, and visk holes, as depicted in Figure 3.14. Since the compression forces on the screws, forward nacelle holes, and visk holes are identical, the compression stress analysis need only be concerned with stresses on the visk, the material yield of which is one order of magnitude smaller than that of aluminum alloy T6061, shown in Table 3.2. Given that the forward nacelle weight, W_{FN}, and the inlet suction force, F_s, are acting on the forward nacelle, the compressive stress on the visk hole is defined as

$$\sigma_{comp} = \frac{W_{FN} + F_s}{A_{comp}}, \tag{3.13}$$

where A_{comp} is the projected rectangular area of compression, which is equal to the product of the screw diameter and the nacelle lip thickness. With a safety factor of 4.0, employed to meet safety factor requirements set by the QFF, this compressive stress has a value of 0.65 MPa (94.14 psi) per hole, two orders of magnitude smaller than the material yield stress of the visk SLA material. Similarly, the shear stress on the fastener resulting from the forward nacelle weight and inlet suction force is expressed by

$$\tau_{shear} = \frac{W_{FN} + F_s}{A_{shear}}, \tag{3.14}$$

where A_{shear} is the cross-sectional area of the screw. A screw diameter of 6.4 mm (0.25 in), large enough for easy handling and repeated wear during use, yields a shear stress of 0.95 MPa (137.84 psi) with a safety factor of 4.0, two orders of magnitude smaller than the material yield stress of the stainless steel nacelle screws as shown in Table 3.3. It is clear from the analysis of the nacelle-visk joints that the local compressive and shear stresses pose no risk to the structural integrity of the swirl tube.

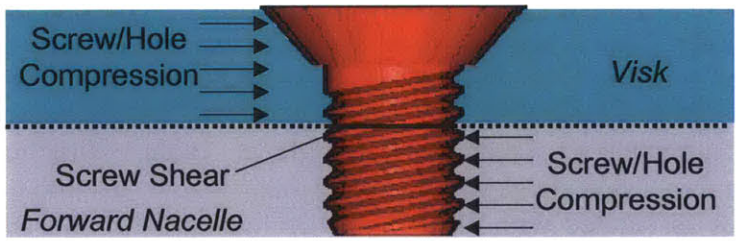

Figure 3.14. Shear and compression forces acting at forward nacelle-visk lap joint.

3.5.2.3 Stress Analyses at Pylon Tab

The third critical structural location in this analysis is the pylon tab: the slender, 1.75" protrusion on the outer shroud of each visk that connects the entire swirl tube assembly to the support pylon. The pylon tab and the four screws used to fasten it to the support pylon transmit all loads experienced by the swirl tube during testing to the support pylon. Figure 3.15 shows the loads acting on the swirl tube, contributing to reaction moments at the pylon tab in the y- and z-directions, M_y (-6.18 N-m, -4.56 ft-lbs) and M_z (11.14 N-m, 8.22 ft-lbs), as well as a shear force, V_y (-76.5 N, -17.2 lbs), acting in the y-direction. These reaction moments and forces, shown in three-dimensions in Figure 3.16, stress the pylon tab as both a beam-like and plate-like structure. Thus, both fundamental beam and plate theories are applied to the pylon tab to compute maximum stresses, the effects of which are superimposed to solve for total stresses.

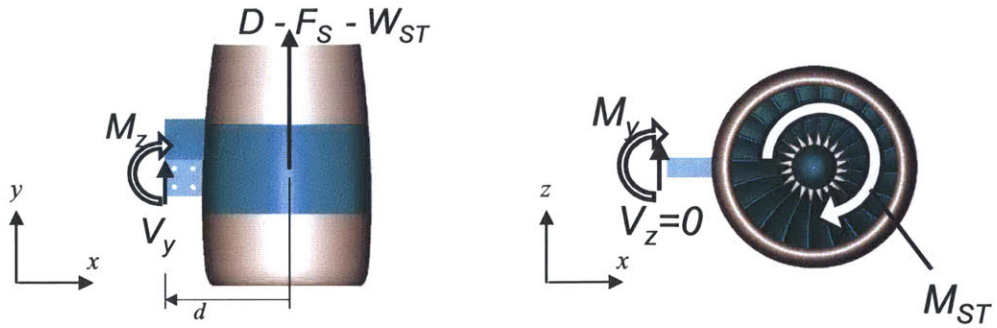

Figure 3.15. Aerodynamic and structural loads contributing to reaction moments and shear forces at pylon tab.

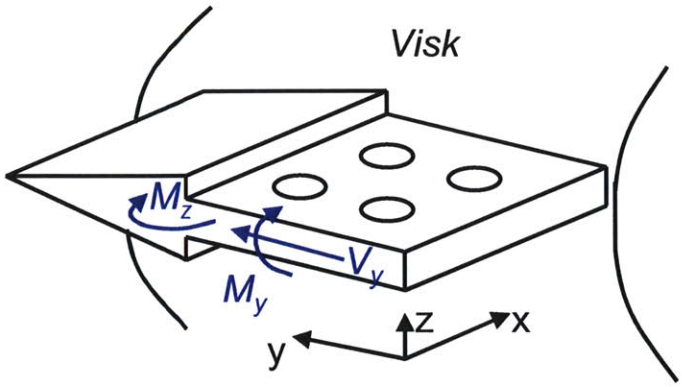

Figure 3.16. 3-D view of bending moments and shear forces acting on pylon tab. Moments M_y and M_z along with shear force V_y stress the pylon tab as both a beam-like and plate-like structure.

Moment M_y creates a tendency for the pylon tab to deflect in the z-direction, the direction of the pylon tab's smallest dimension (thickness, t). Plate theory can be used to describe the tensile and compressive stresses associated with plate-like deflection of the pylon tab given the following assumptions [30].

1. The normal to the middle surface, defined as the surface located at distance $t/2$ in the z-direction from the top or bottom surfaces, remains normal after deformation.

2. There is no strain on the middle surface.

3. The normal stress in the z-direction is negligible.

Solecki and Conant [30] provide an in-depth discussion of plate theory, similar to simple beam theories, from which the maximum stress due to moment M_y can be calculated:

$$\max \sigma_{PL} = \frac{6M_y}{y_{PT} \cdot t_{PT}^2}, \tag{3.15}$$

where y_{PT} is the length of the pylon tab in the y-direction and t_{PT} is its area-averaged thickness in the z-direction. From Equation 3.15, the maximum plate stress on the pylon tab is found to be ±4.89 MPa (±709 psi), the sign of which depends on which surface, the top or bottom, is being analyzed.

Similarly, fundamental beam theory can be applied to the pylon tab as it bends in the x-y plane given the following assumptions [10].

1. The beam axis is straight prior to deformation.

2. Displacements due to deformation are small.

3. Material is linearly elastic and homogeneous over any given cross-section.

The flexure formula given in Equation 3.9 is rewritten in Equation 3.16, giving the stress from beam-like bending of the pylon tab in terms of the moment M_z.

$$\sigma_{x,BM} = -\frac{M_z}{I_{z,PT}} \cdot y \tag{3.16}$$

The locations on the y-axis of the pylon tab at which the bending stress is maximized are the points furthest from the centroid as shown in Figure 3.17: y = 4.9 cm (1.93 in) and y = -4.5 cm (-1.76 in). These yield respective bending stresses of –4.4 MPa (–638 psi) and 3.7 MPa (532 psi), the larger of which is summed with the maximum plate stress calculated above to produce the total bending stress on the pylon tab. The total bending stress is thus –9.3 MPa (–1,347 psi).

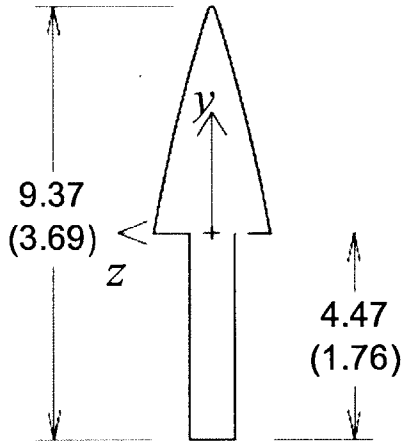

Figure 3.17. Dimensioned cross section of pylon tab. Centroid is located at axis origin. Primary dimensions are given in centimeters outside parenthesis with inch equivalents inside parenthesis.

Approximating the pylon tab to have roughly a rectangular cross-section, the shear formula for prismatic beams, given in Equation 3.17, can be used to compute the maximum shear stress in the pylon tab using the first moment of area with respect to z, Q_z.

$$\tau_{xy,BM} = \frac{V_y \cdot Q_z}{I_{z,PT} \cdot t_{PT}} \tag{3.17}$$

This maximum shear stress, calculated to be 0.7 MPa (97.8 psi), is used in tandem with the total bending stress of –9.3 MPa (–1,347 psi) to construct Mohr's circle, from which the principle stresses on the pylon tab are found. Mohr's circle plots the exchange, or stress transformation, between bending stress and shear stress as the orientation of the stressed element changes with respect to the orientation of principle axes. Construction of Mohr's circle, given in Figure 3.18,

shows principle stresses σ_1 and σ_2 to equal 0.05 MPa (7.06 psi) and –9.34 MPa (–1354.2 psi), respectively. These principle stresses are used to compute the total magnitude of stress on the pylon tab given its multi-directional stresses. Equation 3.18 gives the expression for the total magnitude stress, known commonly as the 2-D Von Mises stress.

$$\sigma_{VonMises} = \sqrt{\sigma_1^2 - \sigma_1\sigma_1 + \sigma_2^2} \tag{3.18}$$

The QFF-required safety factor of 4.0 is applied to the Von Mises stress of 9.4 MPa (1,358 psi) to yield an allowable pylon tab stress of 37.4 MPa (5,431 psi), 80% of the yield strength of the SLA visk material as tabulated in Table 3.3. This indicates that the pylon tab is sufficiently sized to accommodate the loads experienced by the model during testing.

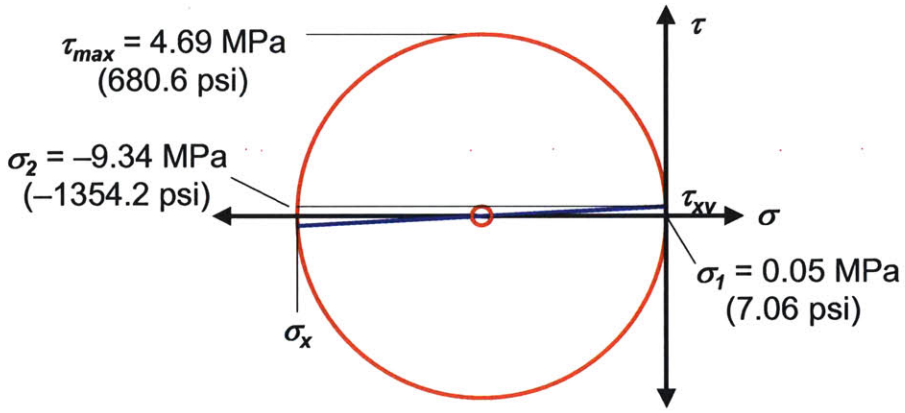

Figure 3.18. Mohr's circle for pylon tab stresses. Total bending stress, σ_x, and maximum shear stress, τ_{xy}, are used to construct the circle, from which the principle stresses σ_1, and σ_2 are found.

Like the turning vanes-shroud junctures, the pylon tab meets the visk outer shroud at right angles, once again producing sharp corners with the tendency to produce high stress concentrations. An appropriate fillet radius was applied to reduce local stress concentrations, computed by the same empirical methods of Roark and Young [32] discussed in Section 3.5.2.1 and Appendix B. Here, the maximum stress concentration factor, K_{max}, was found to be 1.26, which, given the geometry of the pylon tab, was a satisfactory upper bound for stress concentration using a fillet radius of 7.6 mm (0.3 in).

Lastly, the mechanical fasteners, used to secure the pylon tab (i.e. swirl tube assembly) to the support pylon, and the holes in the pylon tab through which the screws pass are subjected to compressive and shear stresses due to aerodynamic and structural loads. The net force on the swirl tube, shown in Figure 3.15 as $D - F_{ST} - W_{ST}$, compresses the pylon tab screws and pylon tab screw holes while shearing the screw at both interfaces where the visk (pylon tab) meets the pylon (see Figure 3.19). Equations 3.19 and 3.20 give the compressive and shear stresses, respectively. Note that the factor of two in the denominator of Equation 3.20 accounts for the dual locations (areas) at which the fastener is sheared.

$$\sigma_{comp} = \frac{D - F_s - W_{ST}}{A_{comp}}, \tag{3.19}$$

$$\tau_{shear} = \frac{D - F_s - W_{ST}}{2A_{shear}}, \tag{3.20}$$

As with the case of the nacelle screws and shroud holes, the compressive and shear stresses on the pylon tab and pylon tab holes, 2.4 MPa (348.54) psi and 1.9 MPa (275.19 psi) using a safety factor of 4.0, respectively, are small compared to the material yield stresses of the visk SLA material, the aluminum alloy of the pylon, and the stainless steel of the screws. This stress assessment shows that the pylon tab and its associated fasteners are sized appropriately to safely accommodate the maximum structural loads experienced during wind tunnel testing of the swirl tube.

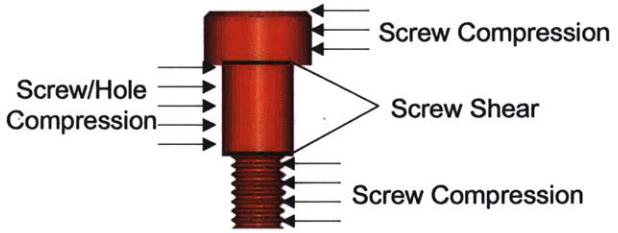

Figure 3.19. Shear and compression forces acting on pylon tab screw. Because screw passes through pylon tab completely, shearing occurs at two locations (pylon-pylon tab interfaces).

3.5.2.4 Stress Analyses at Pylon-Wall Junction

The final critical structural location in this analysis is the junction of the support pylon and the (QFF) wind-tunnel wall. Analysis of this the pylon involves confirming the root (pylon-wall junction) of the pylon is the cross section of maximum stress, determining the exact point of maximum stress within this cross section, and calculating the total local stress of this critical point.

Maximum stresses in a beam occur in the cross section at which the local bending moment is maximized. To compute the bending moment distribution across the span of the pylon, the loads and subsequent reaction forces and moments must first be calculated. The QFF pylon, a 35.56 cm-long (14 in), slender support of constant cross-section, acts like a cantilevered beam with a tip moment in the x-z plane equal to the swirl moment M_{ST}, a tip load equal to the net loading on the swirl tube ($D - F_{ST} - W_{ST}$), and a distributed load across the span equal to the pylon weight and the drag force on the pylon. Using the viscous subsonic airfoil design tool XFOIL (M. Drela, MIT), the drag coefficient, and subsequently the drag force, on the pylon was found to be approximately 0.011, negligible compared to the estimated minimum and maximum swirl tube net drag coefficients of 0.4 and 1.31, respectively. Figure 3.20 shows the loading scheme of the pylon with its reaction forces, F_{x0}, F_{y0}, and F_{z0}, and its reaction moments, M_{x0}, M_{y0}, and M_{z0}, at the pylon root. From simple observation, it is evident that F_{x0}, F_{z0}, and M_{x0} (not pictured) are all

zero, since they have no forces or moments in their given directions to counteract. Summing forces and moments, the remaining three forces and moments were found: F_{y0} = -61.2 N (-13.75 lbs), M_{y0} = -6.18 N-m (-4.56 ft-lbs), M_{z0} = 32.20 N-m (23.75 ft-lbs). Due to the distributed loads on the pylon, the bending moment and shear force vary over the pylon span. These quantities, as functions of spanwise direction x, are computed by cutting the beam at various x locations and replacing the cut portion with a tip force, SF, and tip moment, BM, representing the local shear force and bending moment, respectively. Doing so yields Equation 3.21 for shear force distribution and Equation 3.22 for bending moment distribution, both plotted in Figure 3.21.

$$SF(x) = F_{y0} - W_{PY}x \tag{3.21}$$

$$BM(x) = F_{y0}x - W_{PY}\frac{x^2}{2} + M_{z0} \tag{3.22}$$

It is clear from Figure 3.21 that the parabolic bending moment distribution reaches its maximum value of 32.20 N-m (23.75 ft-lbs) at the root (x = 0") location, thus the maximum local stresses occur within this cross section.

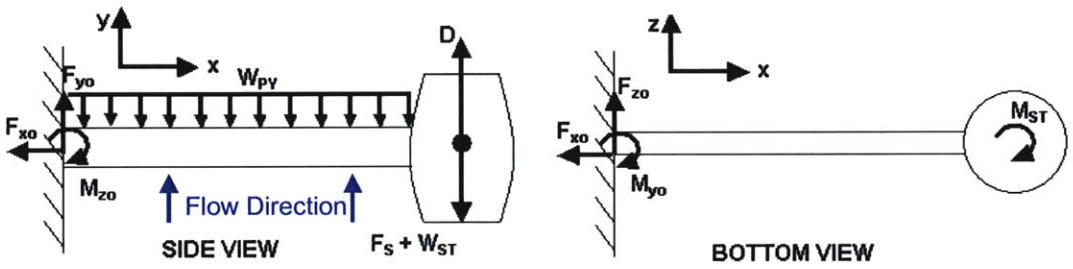

Figure 3.20. Swirl tube load diagrams for QFF test with pylon-wall junction reaction forces and moments. Moment M_{xo}, not shown, is equal to zero since there is no applied moment in the x-direction to counteract.

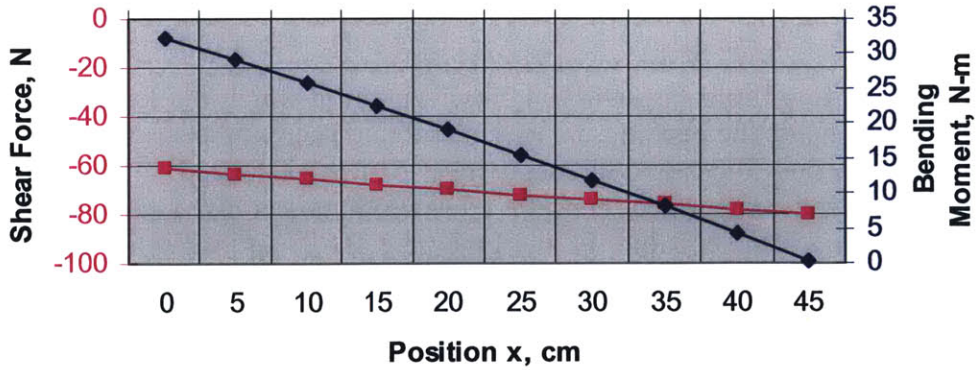

Figure 3.21. Bending moment (dark blue) and shear force (magenta) diagram for QFF pylon in bending. Maximum bending moment occurs at x = 0 cm, indicating the cross section at the pylon-wall junction contains the point of maximum bending stress.

Given that two orthogonal moments, M_y and M_z, are acting on the pylon, the precise location of maximum stress is not initially obvious. First, properties of the pylon's NACA 0022 cross section, including centroid and moments of inertia, were calculated using computational geometric analysis tools common to standard 2-D and 3-D CAD software packages. Figure 3.22 gives basic dimensions of the cross section, the centroid of which is located at the axis origin as shown, 4.55 cm (1.79 in) above the bottom most point of the cross section along the axis of symmetry. Using these cross-sectional properties, the bending stress due to orthogonal moments M_y and M_z can be expressed as a function of location (y,z) within the cross section and yields

$$\sigma_x = \frac{M_y}{I_y} \cdot z - \frac{M_z}{I_z} \cdot y \,. \tag{3.23}$$

This demonstrates that the maximum bending stress will occur somewhere on the edge of the cross section, since the edge points comprise the set of points (y,z) which are furthest from the centroid. With the (y,z) point geometry of the cross section contour (NACA 0022) known, the stress, σ_x, is evaluated over the edge contour. A maximum bending stress of 2.02 MPa (293.6 psi) was found to occur at the point (y,z) = (9.68 mm, -33.04 mm) (0.381 in, -1.301 in), in the lower right-hand quadrant of the cross section as pictured in Figure 3.22. The local shear stress at this location, τ_{xy}, is found to be 0.09 MPa (13.05 psi) using the shear formula for prismatic beams in bending, given in Equation 3.17. The principle stresses are found by constructing Mohr's circle in the same means in which it was constructed for the pylon tab stresses in Section 3.5.2.3. For the pylon-wall junction, Mohr's circle is given in Figure 3.23, yielding principle stresses of σ_1 = 2.03 MPa (294.2 psi) and σ_2 = -3.99 kPa (–0.578 psi). The total maximum stress on the cross section at this critical location is given by the 2-D Von Mises stress, calculated using Equation 3.18. Employing the standard safety factor of 4.0, the maximum normal stress on the pylon is 8.12 MPa (1,177 psi), well below the material yield stress of aluminum alloy T6061 as shown in Table 3.3.

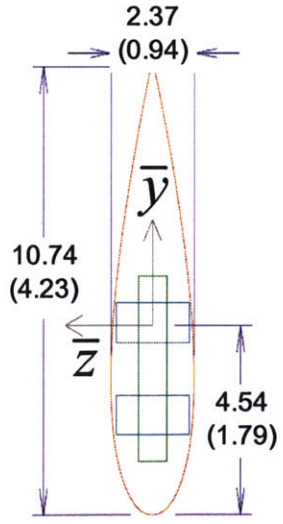

Figure 3.22. Dimensioned cross section of QFF pylon. Centroid is located at axis origin. Primary dimensions are given in centimeters outside parenthesis with inch equivalents inside parenthesis. Locations of pylon tab and pylon tab screws are indicated by green and light blue boxes, respectively.

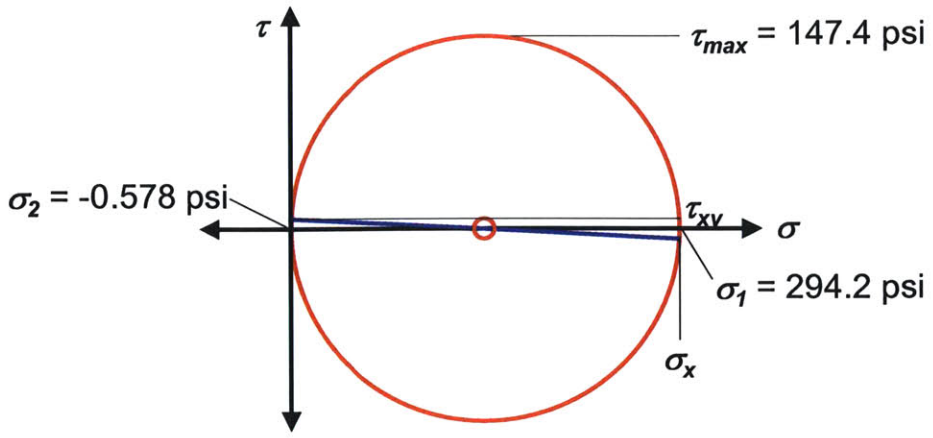

Figure 3.23. Mohr's circle for QFF pylon stresses. Total bending stress, σ_x, and maximum shear stress, τ_{xy}, are used to construct the circle, from which the principle stresses σ_1, and σ_2 are found.

From this analysis, it can be concluded that the maximum stress levels in the pylon, like at the other critical structural locations previously analyzed, are well below material yield stresses, ensuring that the swirl tube test model can safely accommodate the aerodynamic and structural loads of the aerodynamic and aero-acoustic wind-tunnel tests.

3.6 Boundary Layer Trip

All flow surfaces of the swirl tube, including the pressure and suction sides of the turning vanes and nacelle, were treated with boundary layer trip tape, used to transition the flow to turbulent to best instate similarity between the flows encountered by the scaled swirl tube model and a full-scale device. The degree of dynamic similarity between flows can be assessed by comparing Reynolds numbers, defined as the ratio of inertial forces to viscous forces,

$$\mathrm{Re}_L = \frac{V_\infty L}{\nu}, \tag{3.24}$$

where L is the characteristic length and ν is the kinematic viscosity of air. The swirl tube test article, as designed, has an inlet diameter that is approximately $1/7^{th}$-scale of inlet diameters common to standard mid-weight commercial aircraft engines, likely locations for swirl tube installations on aircraft (see Chapter 5). Given the $1/7^{th}$ scaling of the model, a full-scale turning vane would have an average chord of 44.5 cm (17.5 in), the Reynolds number for which at free stream M = 0.17 is 1.76×10^6. This Reynolds number indicates the flow over the vane would clearly be turbulent, since the onset of turbulence occurs for Reynolds numbers greater than $2.3 \times 10^3 - 4.0 \times 10^4$. Reynolds numbers for model-scale turning vanes, averaging 6.35 cm (2.5 in) in chord length, range from 4.44×10^4 to 2.51×10^5 for Mach numbers between 0.03 and 0.17, close to the laminar-turbulent transition regime. If model scale flows are not turbulent, the ensuing laminar flows could cause separation bubbles to occur in or behind the turning vane passages, potentially detrimental to proper flow turning and, consequently, swirl tube drag and

noise performance. Thus, to ensure model scale flows will be fully turbulent as they would be in full-scale devices, boundary layer trip is applied to all flow surfaces (i.e. the flow is "tripped"). The boundary layer trip used in this series of experiments was forward serrated rubber or aluminum tape adhered to the pressure and suction sides of the turning vanes and nacelle at precise chord-wise distances. This method of tripping the boundary layer was taken from results of boundary layer trip experiments conducted by Andreou et al. [1], tested the shape, position, thickness, and orientation of various trip materials. The study found that boundary layer trips were most effective when using 0.5 mm – 1.0 mm (0.02 in – 0.04 in) thick material with forward-facing serrations located rearward of the leading edge by either 9% of the chord length if on the airfoil pressure side or 3% of the chord length if on the airfoil suction side. These guidelines for trip usage were followed, employing electrical rubber or aluminum tapes on all vane and nacelle pressure and suction surfaces. Actively "listening" to the boundary layers over the nacelle and vanes using a small boundary layer digital stethoscope confirmed that the applied strips successfully tripped the boundary layer. Though the strips were changed from electrical rubber to aluminum tape for improved adhesion to the nacelle and visk surfaces, no difference in aerodynamic or acoustic performance was observed.

3.7 Summary of Swirl Tube Mechanical Design

The outcome of the mechanical design presented in this chapter is a $1/7^{th}$ scale test model. The model's modular design employs interchangeable visks to vary the swirl vane angle setting. Visks were fabricated for swirl angle setting from 0° to 64° to include both stable swirling flows and swirling flows with vortex breakdown, previously predicted to occur at swirl angles exceeding ~50°. The model was sized for testing in two wind-tunnel test facilities, the WBWT and QFF, according to test facility dimensions, including the potential core of the QFF free jet. A structural analysis of the model under maximum loading conditions was performed to identify critical structural locations and the corresponding nominal stresses and/or stress concentrations at these points. The analysis showed that stresses at critical locations are well below material yield stresses with safety factors of at least 1.5 employed to eliminate the risk of structural failure of the swirl tube model. For similarity between the model-scale and full-scale swirl tube flows, boundary layer trips were applied to all vane and nacelle surfaces to ensure flows through the device were turbulent. Though wind-tunnel test conditions provided Mach number similarity, the scale of the swirl tube test model was such that Reynolds number similarity was not achieved.

Chapter 4

Experimental Aerodynamic and Aero-Acoustic Assessment of Swirling Exhaust Flows

4.1 Overview of Swirling Flow Aerodynamics and Aero-acoustics

Chapter 4 presents an assessment of swirling flow aerodynamics and aero-acoustics based on wind tunnel testing of the swirl tube at the WBWT and QFF facilities. Figure 4.1 captures the key result: highly swirling exhaust flows are capable of generating quiet drag. Swirl vane angle settings near 50° yield full-scale drag coefficients of ~0.8 ±0.04 with a full-scale overall sound pressure level (OASPL) of 42 dBA ± 2 dBA.

Analyses of both aerodynamic and aero-acoustic test results, described in more depth in the following sections and briefly summarized here, validate the hypotheses stated in Chapter 1. The key result mentioned above validates the first hypothesis that steady swirling flows are quiet means of generating pressure drag. It was also hypothesized that there exists an upper stability limit for swirl at which point the steady streamwise vortex breaks down, diminishing both drag generation and noise reduction capabilities. As predicted by Shah [29], the upper stability limit for swirl was qualitatively and quantitatively identified to occur between 47° and 53° swirl vane angle settings, where drag capacity decreases and noise level increases sharply due to vortex breakdown. Quadrupole- and turbulent scattering-type noise sources were identified in stable swirling flow cases, radiating from the downstream exhaust core and nacelle trailing edge regions, respectively. Vortex breakdown cases (swirl angle > 50°) were found to be 10 to 15 dB louder than stable swirling cases at all frequencies, attributable to the increased scattering noise due to the turbulence of the burst vortex near the rear nacelle surfaces and edges.

Stable swirl cases and those exhibiting vortex breakdown present two distinctly different flow features in terms of both aerodynamic performance and acoustic behavior. The focus of this chapter is the assessment and comparison of these two flow features to best quantify the aero-acoustic capabilities and limitations of swirling flows for quiet drag purposes.

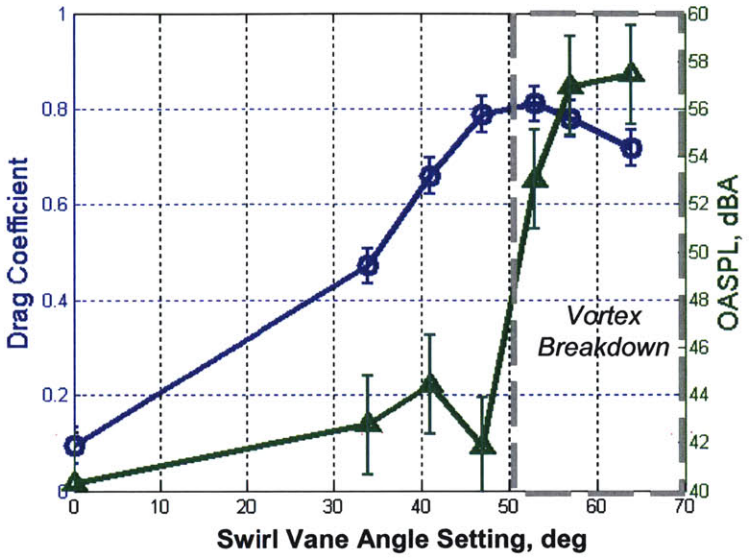

Figure 4.1. Full-scale (D = 1.2 m) drag coefficient and OASPL for swirling flows of various swirl vane angle settings. Stable swirling flows (white background) are capable of generating drag coefficients over 0.8 ± 0.04 at full scale OASPL less than 42 dBA ±2 dBA. For swirl angles exceeding ~50° (gray box), breakdown of the steady vortex causes drag generation to decrease while scattering noise from turbulent eddies of the burst vortex structure near sharp nacelle edges leads to a distinct increase in noise level.

4.2 Aerodynamic Assessment of Swirling Exhaust Flows

The aerodynamic performance of swirling flows was assessed in terms of drag capability and exhaust flow field characteristics, such as velocity and swirl angle profiles. All aerodynamic assessments, including drag performance, wake characteristics, and swirl stability limits, were in agreement with the CFD predictions by Shah [29]. The following subsections describe the drag and flow field characteristics of swirling exhaust flows, distinctly different between stable swirling cases and cases exhibiting vortex breakdown.

4.2.1 Characteristics of Stable Swirling Flows

The swirl tube aerodynamic design is validated by comparing experimentally measured exhaust flow field characteristics, including velocity and swirl angle profiles, to the previously obtained CFD predictions. Figure 4.2 shows free stream-normalized axial velocity, free stream-normalized tangential velocity, and swirl angle radial profiles at downstream locations $z/D = 0.5$ and 1.0 for the stable, 34° swirl case. The experimental results obtained by hotwire traverse measurements (blue circles) match corresponding profiles estimated by CFD computations

(black crosses) well, accurately capturing the high-velocity axial core region at $r/r_{duct} < 0.2$ and outer swirling annulus at r/r_{duct} between 0.2 and 1.0. Upon closer examination, the circumferential velocity and swirl angle profiles measured experimentally indicate a slight overturning as compared to CFD predictions, suggesting higher measured drag levels as compared to drag estimated by CFD. This agrees with the drag analysis discussed later in this section.

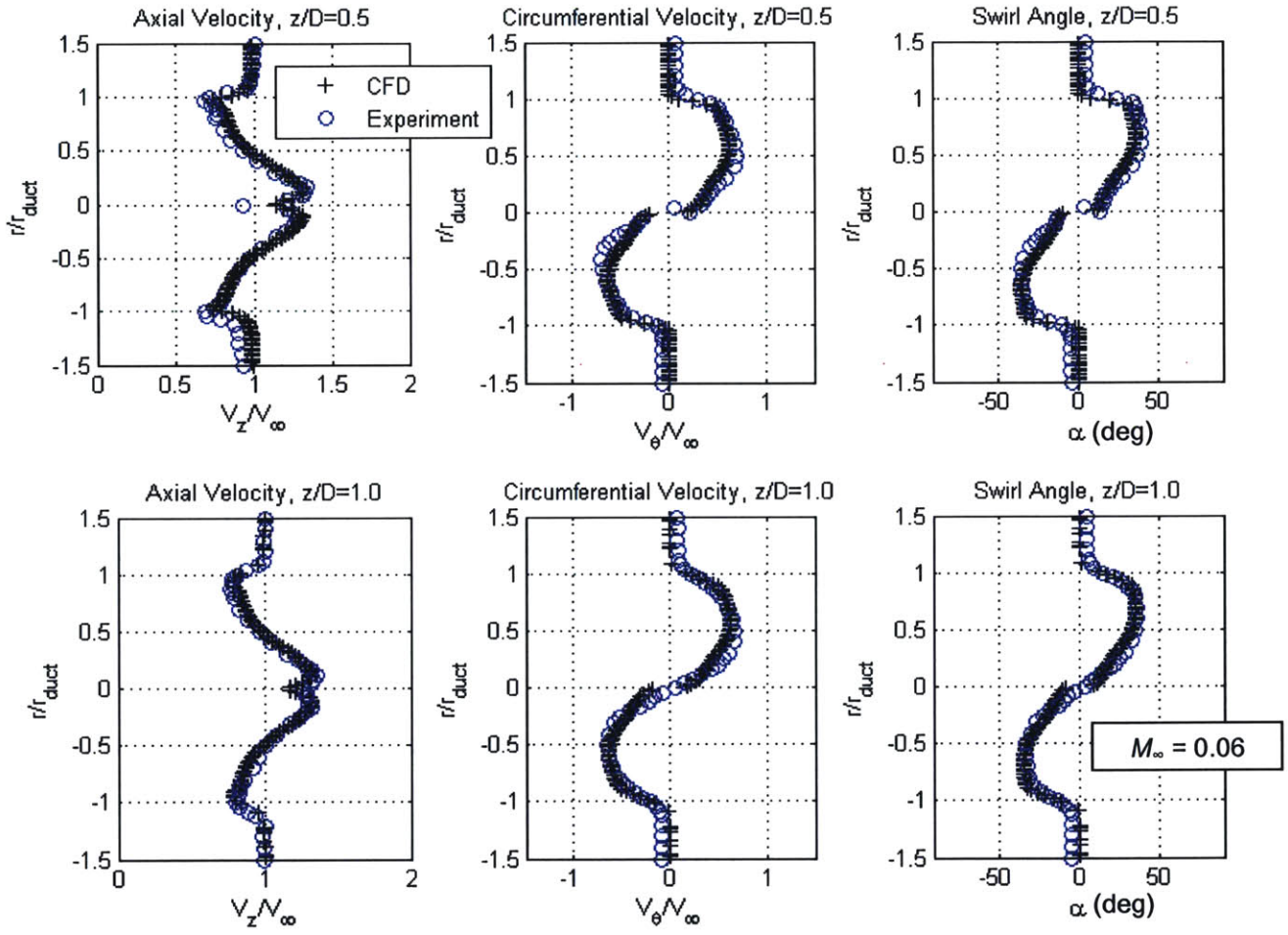

Figure 4.2. Axial velocity, tangential velocity, and swirl angle radial profiles for 34° swirl case at various locations downstream of nacelle exit. Good agreement is observed between experimental measurements and CFD predictions while slight overturning in experimental data suggests higher drag levels compared to CFD [29].

The main aerodynamic performance objective is to generate a maximum model-scale drag coefficient greater than 0.8 as predicted by high-fidelity calculations. Figure 4.1 shows that stable swirling flow of the 47° swirl case achieves a model-scale drag coefficient of 0.83, exceeding the target drag coefficient. The drag coefficients are comprised of a viscous drag component, generated by viscous forces acting on the nacelle and vane surfaces, and a pressure drag component, generated by the swirl-induced low-pressure core region,

$$C_{D_{Model}} = C_{D_{pressure}} + C_{D_{viscous}} . \tag{4.1}$$

Drag measurements of the 0° straight vane configuration provided an estimate for swirl tube viscous drag from the nacelle and vane surfaces: $C_{D,viscous} = 0.14$. Since the swirl tube is a pressure drag device, it is expected that the viscous drag is small compared to the pressure drag component.

To compare the measurements with Shah's full-scale device drag predictions, the model-scale drag coefficients must first be scaled to the full-scale device of 1.2 m (3.9 ft) diameter. For this, Reynolds number effects[5] must be considered for the viscous drag component. Given by Equation 4.1, the equivalent full-scale drag coefficient becomes

$$C_{D_{Full}} = C_{D_{pressure}} + C_{D_{viscous}} \cdot \left(\frac{\mathrm{Re}_{Model}}{\mathrm{Re}_{Full}} \right)^{1/5} . \tag{4.2}$$

Table 4.1 presents experimentally measured model-scale and full-scale drag coefficients as well as full-scale drag coefficients previously predicted by Shah [29]. Though the predicted and measured full-scale drag coefficients for the 34° swirl case bear a discrepancy of 0.08, the predicted full-scale drag coefficient of 0.75 for the 47° swirl case agrees well with the measured value of 0.78. These discrepancies arise from slight overturning of flow in the stable swirl cases, as observed in the velocity and swirl angle profiles of Figure 4.2. The drag levels predicted for stable swirling cases, though slightly below the experimental values, are in agreement, validating the swirl tube aerodynamic design for drag capability.

Swirl Angle	Vortex Breakdown	Experimental C_D, Model Scale	Experimental C_D, Full Scale	CFD-Predicted C_D, Full Scale
34°	No	0.52	**0.47**	**0.39**
47°	No	0.83	**0.78**	**0.75**
57°	Yes	0.82	**0.77**	--
64°	Yes	0.76	**0.71**	--

Table 4.1. Experimentally measured and CFD predicted model-scale and full-scale swirl tube drag coefficients for various swirl angles.

[5] Based on turbulent flat plate skin friction coefficient, C_f, where $C_f \propto \mathrm{Re}^{1/5}$ [27].

4.2.2 Swirling Flow Stability Limit and Vortex Breakdown

In addition to achieving model-scale drag coefficients greater than 0.8 from stable swirling flow, a second critical objective was the identification of the swirl stability limit. This limit is marked by the breakdown of the stable, streamwise vortex, hypothesized by Shah to occur between 47° and 57° swirl vane angle settings [29]. Experimental results show that transition from stable swirling flow to vortex breakdown occurs between swirl vane angle settings of 47° and 53°. The smoke visualization images of flows exiting the swirl tube in Figure 4.3 qualitatively confirm this upper stability limit. Each of the stable swirling cases pictured in Figure 4.3 (34°, 41°, and 47°) clearly shows a central core streak of low-pressure, high-velocity flow surrounded by the helical motion of particles in the streamwise vortex. Viscous effects are dominant at the bounds of the central core streak, where turbulent mixing occurs between the high-velocity core stream and the surrounding swirling annular flow. The motion of flow particles in the swirling annulus is apparent in the wave-like helix of smoke trails, the wavelength of which decreases with increasing swirl vane angle. This decrease in wavelength is due to the decrease in axial velocity of flow in the outer annulus as tangential velocity, and thus swirl, is increased by higher vane angle settings. For example, the wavelengths of the helical motion of particles in the 34° and 47° swirl cases in Figure 4.3 have an approximate ratio of 1.3-to-1, comparable to the ratio of approximate axial velocity components, $\cos(34^\circ)/\cos(47^\circ) = 1.22$.

Sufficient helical swirling flow exists in the extreme outer annulus in the vortex breakdown cases such that they are capable of generating drag coefficients greater than 0.7. It is apparent, however, in the vortex breakdown images of Figure 4.3 (57°, 64°) that the central viscous low-pressure region common to the stable swirl cases is absent. Instead, the burst vortex manifests itself as a turbulent separation bubble centered on the core axis just aft of the nacelle exit. This turbulent bubble supplants the high-velocity, low-pressure core responsible for the generation of pressure drag, accounting for the lower drag levels of swirl cases exhibiting vortex breakdown compared to highly swirling stable cases (see Figure 4.1 and Table 4.1).

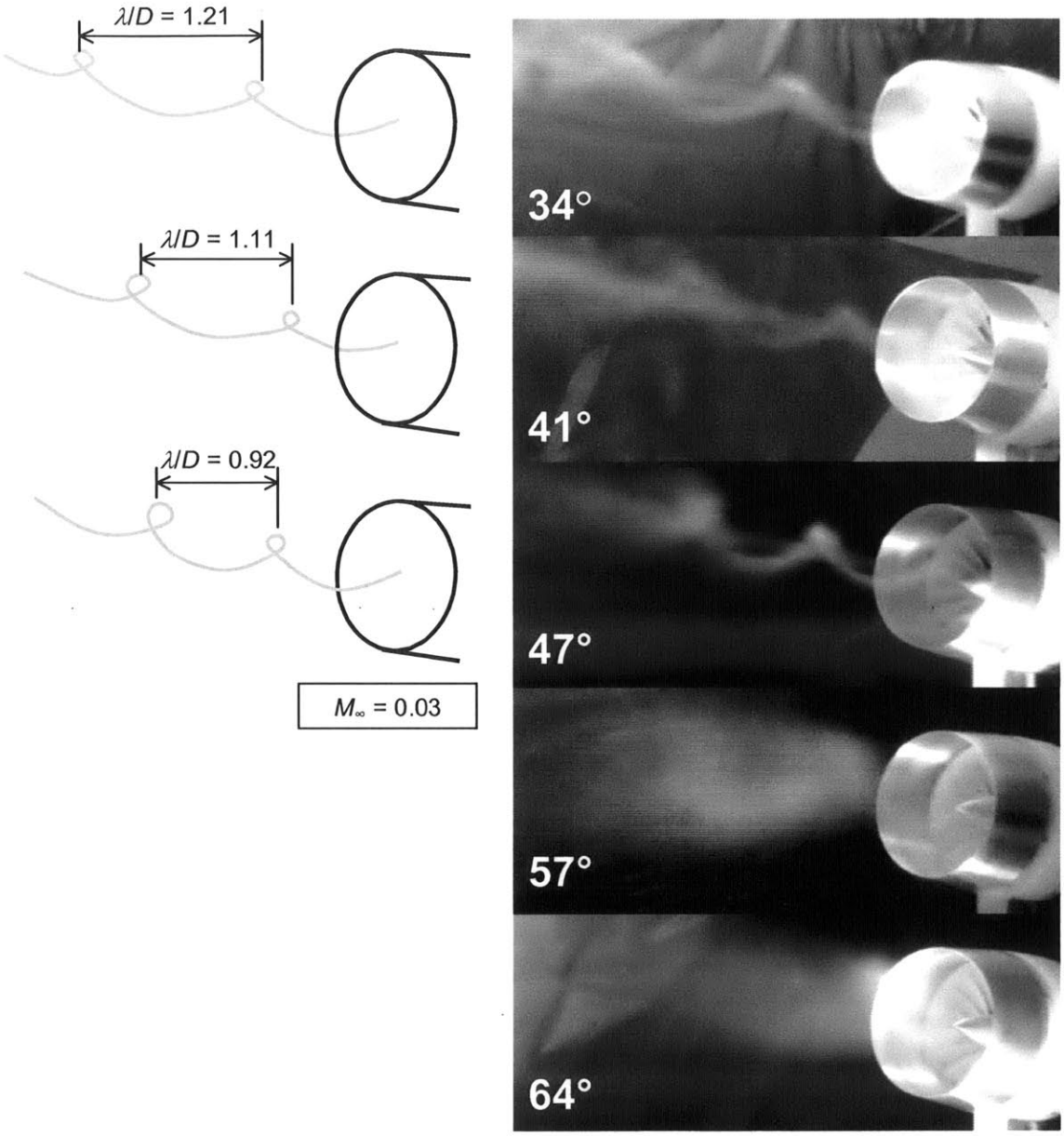

Figure 4.3. Smoke visualization of swirling exhaust flows for various swirl angle settings with sketches of helical wavelengths. Swirl cases less than or equal to 47° each show a stable streamwise vortex with a clear, low-pressure, high-velocity axial core, which generates pressure drag. Smoke visualization of swirl cases greater than or equal to 53° show a turbulent separation bubble on the core close to the nacelle exit associated with the vortex breakdown.

The core-region flow phenomena can be verified as turbulence within a separation bubble by examining unsteady velocity power spectra of the swirl cases exhibiting vortex breakdown. Figure 4.4 shows the power spectral density of the unsteady z and θ velocities. Components were measured on the centerline one-half nacelle exit diameter downstream of the swirl tube exit for the (a) 47° stable swirl configuration and (b) the 57° swirl configuration with vortex breakdown. Unsteady measurements of axial velocity and circumferential velocity were conducted in the z- and θ-directions, respectively. The stable 47° swirl configuration spectra of

Figure 4.4a show distinct peaks at 1.3 kHz in the z-direction and at 2.0 and 4.5 kHz in the θ-direction. Given that these measurements were conducted on the core centerline directly aft of the centerbody, it is suggested that these spectral peaks are attributable to the unsteady flow structures shed into the centerbody wake and convected in the central viscous core of the steady streamwise vortex. The frequencies and magnitudes of these peaks are distinctly different from one another, indicating the presence of distinct axial velocity perturbations and tangential velocity perturbations in the core stream. In contrast to this, the spectra of the 57° vortex breakdown configuration of Figure 4.4b are identical to one another, exhibiting the same roll-off in magnitude with increasing frequency. The collapse of the z-direction and θ-direction spectra in the 57° swirl case suggests directionally independent flow features. From this, it is inferred that the velocity perturbations on the centerline for the vortex breakdown cases are not unique to any direction, implying the presence of a turbulent separation bubble characteristic of vortex breakdown.

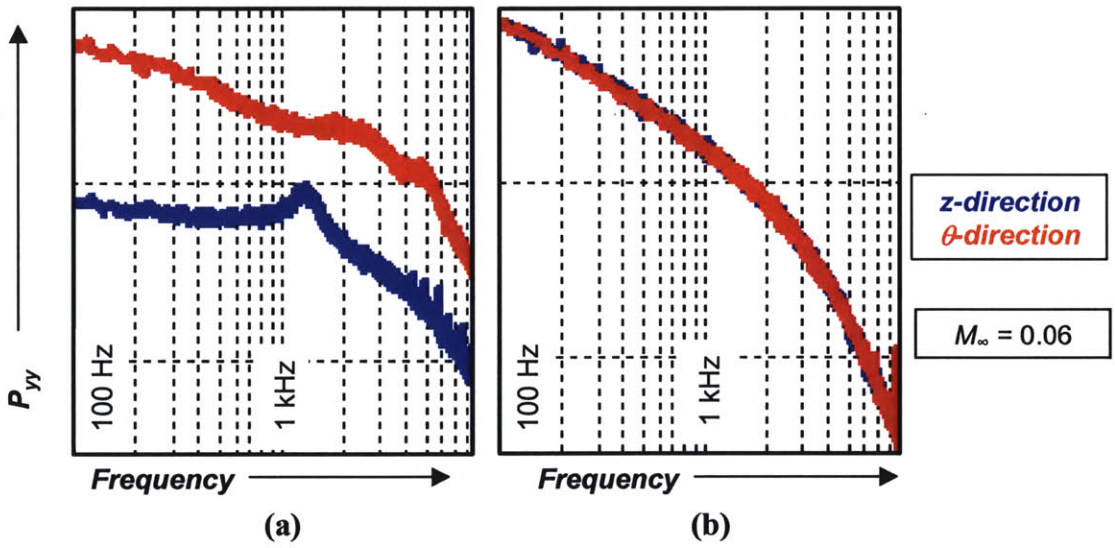

Figure 4.4. Power spectral density of unsteady axial (z) and circumferential (θ) velocities for (a) stable 47° swirl case and (b) 57° swirl case exhibiting vortex breakdown measured on centerline at downstream location $z/D = 0.5$. Collapse of broadband spectra for 57° swirl case indicates separation bubble characteristic of vortex breakdown.

The differences between stable swirling exhaust flows and flows exhibiting vortex breakdown are also quantitatively evident in the velocity and swirl profiles downstream of the nacelle exit. As shown in Figure 4.5, the low-pressure, high-velocity core common to stable swirling cases is clearly absent from the axial velocity profile for the 57° swirl case at downstream location z/D = 1.0. In place of a steady core, the minimal velocities observed between –0.5 and 0.5 r/r_{duct} in both the axial and tangential directions of the 57° case indicate the same directionally independent flow features discussed above, again suggesting the presence of a turbulent bubble, seen qualitatively in the smoke visualization images of Figure 4.3. Discrepancies between the CFD predictions (black crosses) and hotwire measurements (blue circles) are more pronounced in the separation bubble region of the 57° swirl case since the hotwire probe is unable to measure negative velocities. As explained in Chapter 2, the element of the hotwire probe is a variable

resistor in a Wheatstone bridge circuit and quantifies changes in flow velocity by responding to the amount of heat convected from the element. The hotwire probe cannot distinguish between heat convected in different directions and thus cannot distinguish between positive and negative velocities. This implies that while the hotwire probe measurements are sufficient to suggest vortex breakdown as discussed above, they cannot accurately capture the direction of the velocity perturbations within the separation bubble.

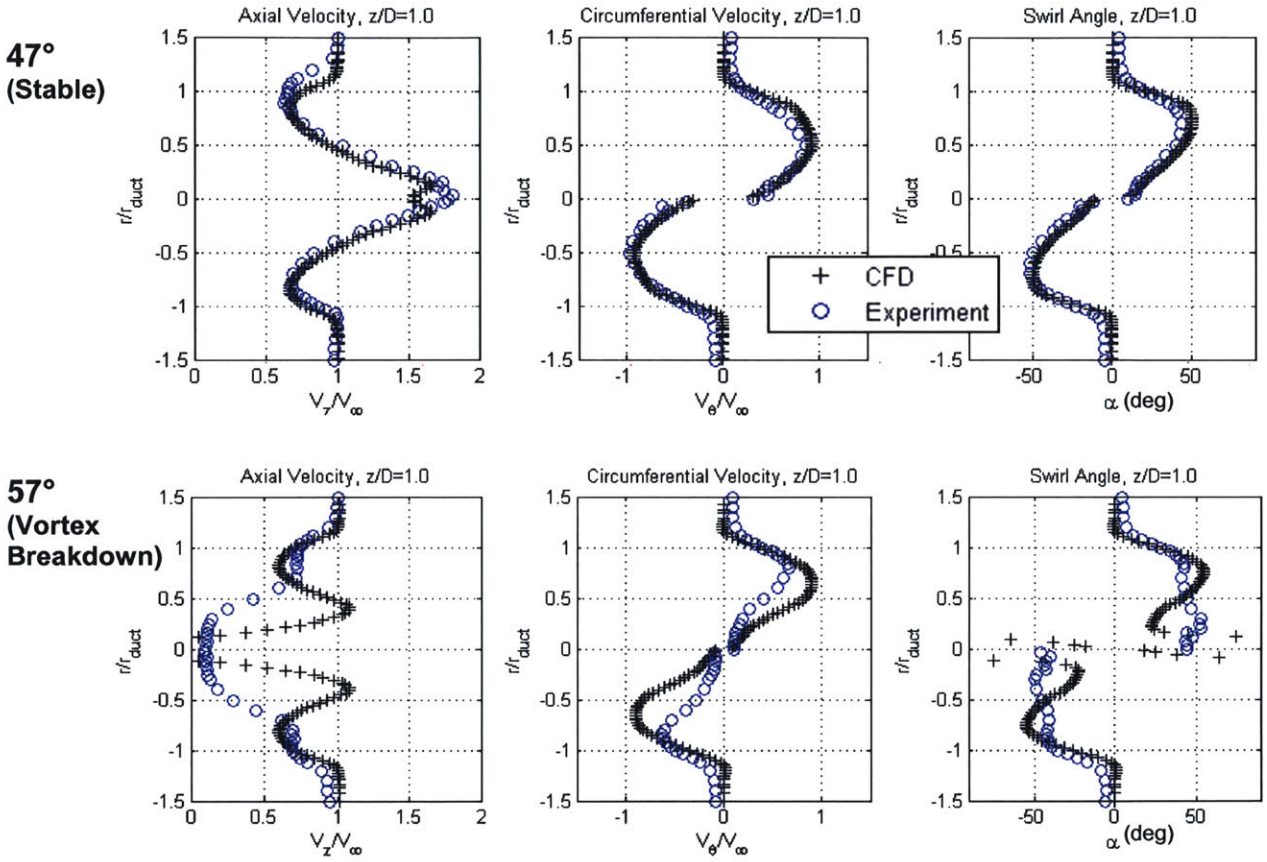

Figure 4.5. Axial velocity, tangential velocity, and swirl angle radial profiles for 47° and 57° swirl cases at $z/D = 1.0$ downstream of nacelle exit. Radial profiles of 57° case indicate presence of turbulent bubble of burst vortex with diameter roughly equal to nacelle exit diameter.

The hotwire traverse measurements also capture the streamwise evolution and mixing out of the swirling exhaust flow. Figure 4.6 shows normalized axial velocity profiles of the 34° swirl case at locations $z/D = 0.5$, 1.0, 2.0, and 4.0 downstream of the nacelle exit with CFD comparisons at the first three locations. As the swirling exhaust flow evolves downstream, the distinct vortex profile seen at $z/D = 0.5$ mixes out, approaching a near-uniform distribution with magnitude close to free stream velocity at $z/D = 4.0$.

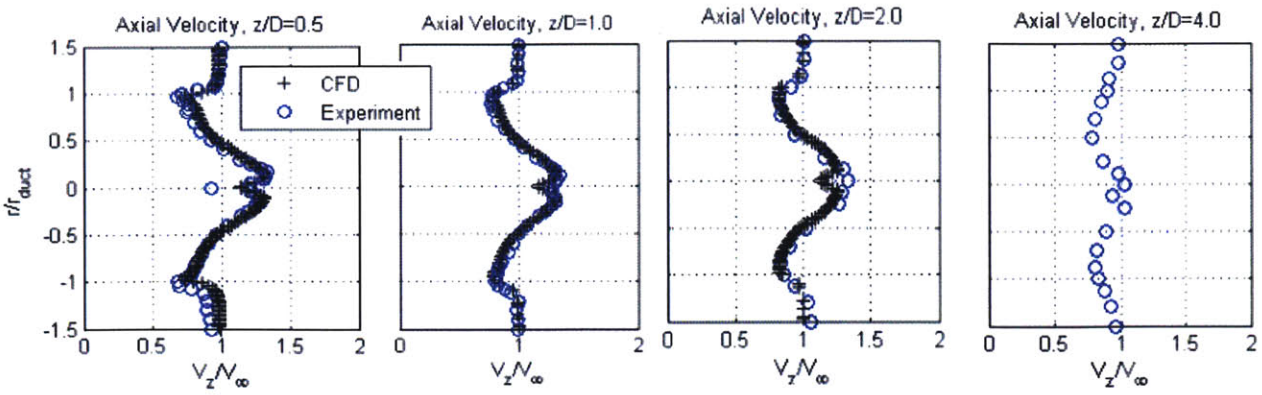

Figure 4.6. Axial velocity profiles for 34° swirl case at various *z/D* locations downstream of nacelle exit. Swirl tube exhaust flow mixes out as it moves downstream, approaching a uniform distribution equal to free stream velocity.

In summary, experimental measurements of velocity and swirl profiles show good agreement with CFD predictions. Results from the reduction of aerodynamic experimental data used to quantify model-scale and full-scale drag levels as well as experimentally validate the stability limit of swirling flows. Finally, the characteristics of vortex breakdown phenomena were assessed, revealing fundamental differences between these and stable swirling flows.

4.3 Aero-Acoustic Assessment of Swirling Exhaust Flows

Figure 4.7 shows narrowband acoustic spectra of the nine standard swirl tube configurations measured at a sideline angle of 90° (see Chapter 2) by a single microphone[6] at Mach 0.17. The figure shows three distinct groups of noise spectra: those associated with (1) non-swirling flows, (2) stable swirling flows, and (3) swirling flows exhibiting vortex breakdown. The assessment of the noise signatures of swirling flows presented in this section is thus divided into three subsections, one for each of the above-mentioned configuration groups. First, a brief synopsis of the results and overview of the following subsections are presented.

The results confirm the hypothesis that stable swirling flows are capable of generating drag quietly, establishing a drag-to-noise relationship that is more desirable than the one-to-one relationship typical of drag devices common to modern aircraft. Broadband peaks at model-scale frequencies between 6 and 15 kHz characterize the acoustic spectra of stable swirl cases in Figure 4.7. This characteristic includes the non-swirl 0° case, suggesting that the development and scattering noise of turbulent structures deriving from turning vane and nacelle end wall turbulent boundary layers cause the low frequency broadband peaks. It was shown that these spectral peaks for different swirl vane angle settings scale with core Mach number for a scaling power $n = 5.0$, resembling scattering-type noise sources. These low frequency broadband peaks coupled with the low noise levels of the spectral roll-offs at higher frequencies account for the quiet noise signature of stable swirling flows.

[6] Microphones in the MADA array are numbered 1 through 41 starting at the array center and counting counterclockwise in an outward spiral fashion. The autospectra presented in this thesis were taken by microphone 18, located on the third ring of the microphone array, based on previous experience with this array.

The results also confirm the hypothesis that the unsteadiness associated with vortex breakdown causes an increase in noise level over the quiet stable swirl cases due to the noise of turbulent flow structures from the burst vortex scattered at the sharp nacelle edges. The spectra of vortex breakdown cases are flat, generating noise relatively equally at all frequencies. At very high swirl angles such as 57° and 64°, the noise signature becomes virtually independent of swirl, as the scattering noise of the burst vortex completely overshadows changes to the acoustic field brought about by variation of swirl angle.

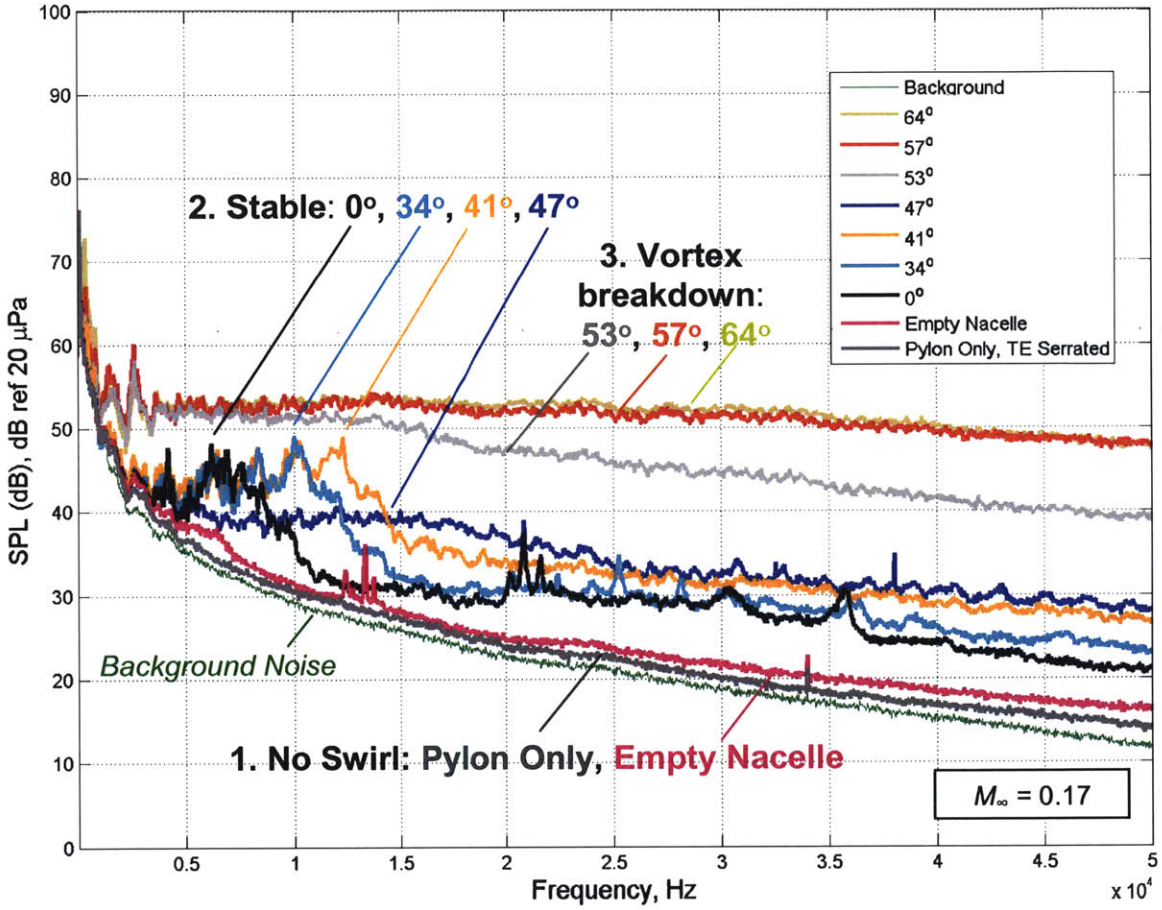

Figure 4.7. Narrowband (17.44 Hz) autospectra of standard swirl tube configurations. Three distinctly different groups of noise-generating configurations are seen: (1) trailing-edge noise-dominated non-swirl cases, (2) stable swirling cases, and (3) swirling cases exhibiting vortex breakdown.

The following subsections discuss the results stated above in further detail. Trailing edge noise, the dominant noise source in the non-swirl cases, is produced as structures from turbulent boundary layers pass over trailing edges, such as those of the nacelle and the pylon. Section 4.3.1 details the analysis of these trailing edge noise sources, comparing their acoustic signatures to similar airfoil geometries tested previously by Brooks, Pope, and Marcolini [5]. Section 4.3.2 identifies the noise mechanisms present in stable swirling cases quantifying their contributions to the observed noise signatures using scaling methods and DAMAS source mapping techniques. It

was found that scattering noise of turbulent flow structures at the nacelle trailing edge is the dominant noise mechanism of stable swirling cases, overshadowing a quadrupole-type noise source associated with the downstream mixing of the high-velocity viscous core and swirling annular flows of the streamwise vortex. Similarly, Section 4.3.3 identifies and quantifies the noise mechanisms present in cases exhibiting vortex breakdown to contrast with the distinctly different acoustic characteristics of stable swirling flows. For vortex breakdown cases, it was found that the increased turbulence associated with the burst vortex both scatters off rear swirl tube surfaces and edges as well as mixes in open flow, radiating efficiently as both scattering- and mixing-type noise mechanisms.

4.3.1 Trailing Edge Noise

Defined in the previous section, trailing edge noise is generated by turbulent boundary layer structures passing over the rear edges of airfoil geometries, such as the pylon and the swirl tube nacelle. Ffowcs Williams and Hall [9] describe the intensity of turbulent structures near an edge by

$$I \sim \rho \frac{U^5}{c^2} \frac{V^2}{r^2 \delta^2}, \tag{4.3}$$

where r is the distance from the source to observer, c is the speed of sound, and δ is the radius of the turbulent structure, assumed to be of cylindrical shape with volume V. Based on this relationship, Brooks et al. [5] rewrite this expression in terms of boundary layer thickness, δ_{BL}, as

$$\left\langle p^2 \right\rangle \propto \rho^2 \frac{U^5}{c} \frac{L\delta_{BL}}{r^2} \bar{D}, \tag{4.4}$$

where $\left\langle p^2 \right\rangle$ is the mean-square sound pressure observed at distance r, $\bar{D}$ is the directivity factor, (equal to 1 for observers normal to the surface from the edge), v' is the turbulence velocity, and $v' \propto U$ is assumed [5].

Previous acoustic estimations, such as those of Howe [16], have suggested the use of sharp trailing edge serrations to reduce trailing edge noise. For the experiments described in this thesis, 1.27 cm (0.5 in) trailing edge serrations, cut at 90° serration angles, were constructed from aluminum tape and applied to the pylon so that its noise signature would not dominate the noise due to the swirling flow. Quantified in the pylon noise spectra of Figure 4.8, the noise attenuation induced by trailing edge serration is as much as ~3 dB per Strouhal number.

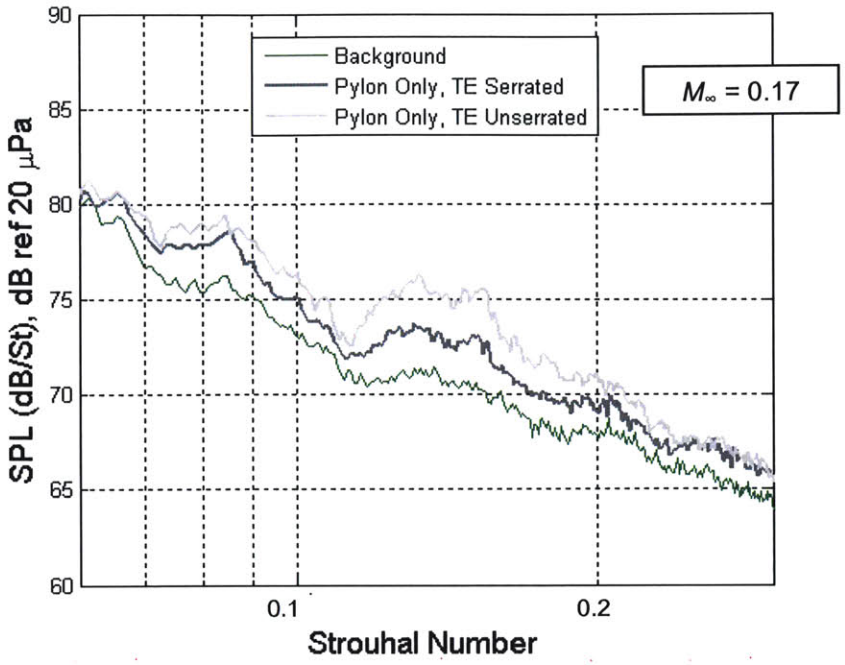

Figure 4.8. Noise spectra of pylon with and without trailing-edge serrations. Trailing edge serration 1.27 cm (0.5 in) in length attenuates trailing edge noise spectrum by as much as ~3 dB/St.

For an airfoil of constant chord, the amplitude of spectral peaks increases linearly with span, since longer spans correspond to more airfoil surface from which turbulent boundary layer structures are created and more trailing edge length over which the turbulent structures pass to generate noise. Based on Equation 4.4, the one-third octave spectra can be scaled according to

$$ScaledSPL_{1/3} = SPL_{1/3} - 10\log\left(M^5 \frac{\delta^* L}{r^2}\right), \tag{4.5}$$

where L is the span and the displacement thickness, δ^*, is $\delta_{BL}/8$ with δ_{BL} estimated by

$$\delta(x) = \frac{0.37x}{(\mathrm{Re}_x)^{1/5}} \tag{4.6}$$

from [13]. Applying this scaling to the DAMAS source integrated zonal spectra of the nacelle and pylon trailing edge regions of the empty nacelle configuration, the trailing edge noise measured experimentally is shown in Figure 4.9 with spectra of airfoils of comparable size and shape previously tested by Brooks et al. [5]. The first observation is that the pylon zonal spectra is noticeably different in scaled SPL and slope than the spectra of the comparably-sized airfoils. Note that the decreased fidelity of DAMAS processing results at frequencies below ~1.6 kHz (St < ~0.1 as shown in Figure 4.9) limits the extent of trailing edge noise analysis at low frequencies, thus accounting for the poor data correlation of the nacelle zonal spectra at Strouhal numbers of approximately 0.1. In spite of this, DAMAS source mapping of the 4 kHz one-third octave band,

a relatively low frequency band at which DAMAS results are highly reliable, in Figure 4.10 clearly displays dominant noise sources distributed along the trailing edges of the nacelle and pylon, confirming their presence at low frequencies.

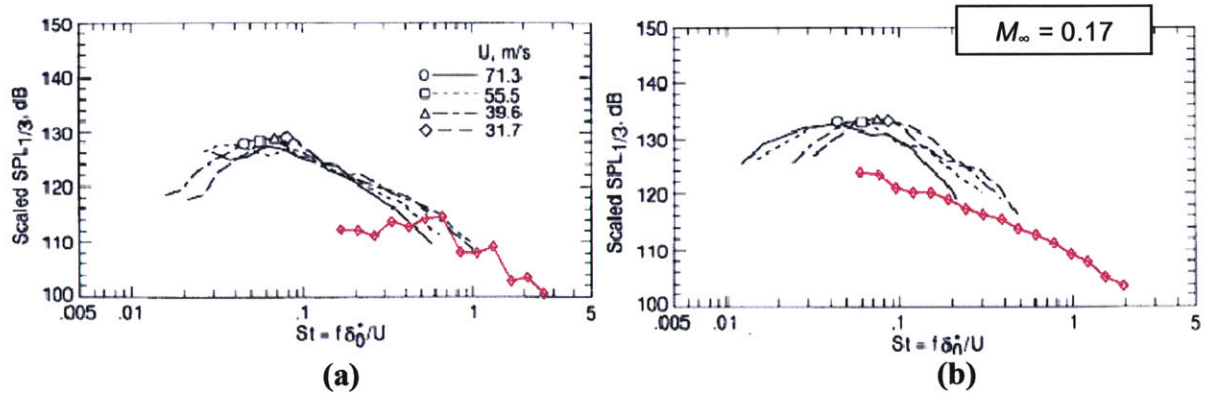

Figure 4.9. Scaled one-third octave noise spectra of (a) nacelle trailing edge and (b) pylon regions of empty nacelle configuration (magenta diamonds). For comparison, noise signatures of NACA 0012 (a) 30.48-cm-chord airfoil (12 in, approximate nacelle chord) and (b) 10.16-cm-chord airfoil (4 in, approximate pylon chord) are presented from Brooks et al. [5].

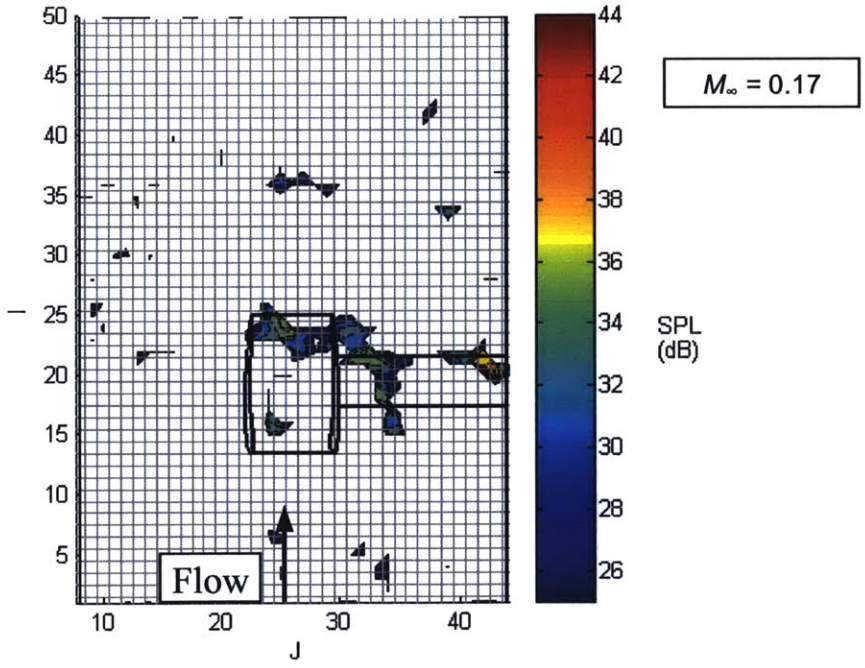

Figure 4.10. DAMAS noise source mapping of empty nacelle and pylon configuration shown for the 4 kHz one-third octave band. Central black solid lines indicate position of swirl tube and support pylon (horizontal lines to the right of the pylon). Noise sources are clearly distributed at nacelle and pylon trailing edges. Each grid box is 2.54 cm x 2.54 cm (1 in x 1 in).

4.3.2 Noise Mechanisms of Stable Swirling Flows

Before assessing the noise mechanisms of stable swirling flows, a brief background to acoustic principles is presented. Lighthill's acoustic analogy on aerodynamically generated sound is based on fundamental compressible mass and momentum conservation equations,

$$\frac{\partial \rho}{\partial t} + \frac{\partial}{\partial x_i}(\rho v_i) = 0, \tag{4.7}$$

$$\frac{\partial}{\partial t}(\rho v_i) + \frac{\partial}{\partial x_j}(\rho v_i v_j + p_{ij}) = 0, \tag{4.8}$$

where ρ is the density of the fluid, v_i is the velocity in the x_i direction, and p_{ij} is the stress tensor acting on a fluid particle in the x_i direction per unit surface area of a surface element with a normal in the x_j direction [19, 20]. To represent sound propagation due to fluctuating stresses in open flows, these equations of fluid motion are rewritten in the form

$$\frac{\partial^2 \rho}{\partial t^2} - c^2 \nabla^2 \rho = \frac{\partial^2 T_{ij}}{\partial x_i \partial x_j}, \tag{4.9}$$

where T_{ij} is Lighthill's stress tensor and c is the speed of sound. For turbulent flows, T_{ij} does not vanish, hence the turbulence gives rise to sound as a quadrupole source.

The scaling laws for open flow mixing of turbulent jets are derived by dimensional analysis. For a free stream velocity U and a jet diameter D, the characteristic time scale is D/U and the wavelength becomes

$$\lambda = c\frac{D}{U} = \frac{D}{M}. \tag{4.10}$$

For low Mach numbers, $\lambda >> D$, thus the source region is compact. Applying the free-space Green's function to the expression in Equation 4.9 yields

$$\rho'(x,t) \approx \frac{1}{4\pi c^2 |x|} \frac{\partial^2}{\partial x_i \partial x_j} \int_V T_{ij}\left(y, t - \frac{|x|}{c}\right) d^3 y, \tag{4.11}$$

where the effect of retarded time over the source region was neglected. Dimensional analysis shows that the density perturbations scale according to

$$\rho'(x,t) \sim \frac{1}{c^2 r} \frac{1}{\lambda^2} \rho_0 U^2 D^3, \tag{4.12}$$

where ρ_0 is the mean flow density and r is the distance to the observer. Using the definition for λ given in Equation 4.10, the mean square value of radiated sound is given by

$$\rho'^2_{rms} \sim \rho_0^2 M^8 \frac{\delta^2}{r^2}. \tag{4.13}$$

Thus, dimensional analysis of Lighthill's acoustic analogy demonstrates that quadrupole-type noise scales with the eighth power of velocity. The intensity of a quadrupole source is given in [9] as

$$I \sim \rho U^3 \left(\frac{U}{c}\right)^5 \frac{\delta^2}{r^2}. \tag{4.14}$$

The right hand side of Equation 4.9 can include various other acoustic noise sources, such as monopoles and dipoles, by respectively including mass injections and/or external forces in the original equations of motion, Equations 4.7 and 4.8. For a given type of noise source, a similar dimensional analysis can be used to determine the relationship between velocity and acoustic intensity using methods employed by Lighthill and Ffowcs Williams and Hall [9, 19, 20]. Comparing Equations 4.3 and 4.14, the intensity of scattering noise of turbulent eddies near edges scales with the fifth power of velocity while the intensity of quadrupole-type sources in the open field scales with the eighth power of velocity. As shown later in this section, these scaling laws are used as one means to help identify noise mechanisms of swirling flows by collapsing data taken at various Mach numbers (free stream velocities) with one of these two Mach number scaling powers.

The results presented in this section suggest that stable swirling flows as generated by a ducted set of turning vanes (i.e. swirl tube) give rise to turbulent scattering- and quadrupole-type noise sources that create a quiet "hiss" sound audible to the human ear in model scale. DAMAS source mapping techniques and the Mach number scaling methods described above were both utilized in identifying and locating these noise sources. Figure 4.11 shows one-third octave frequency DAMAS source maps of the stable 34°, 41°, and 47° swirl cases for the 20 kHz band. All three cases demonstrate the dominant turbulent scattering noise source near the nacelle exit that increases in intensity with swirl angle. For higher swirl angles, a second, quadrupole-type source downstream of the nacelle exit grows increasingly apparent, radiating at similar sound pressure levels as the turbulent scattering noise in the 47° swirl case. The following subsections analyze the scattering noise of turbulent flow structures at the nacelle trailing edge and the downstream quadrupole-type mixing noise.

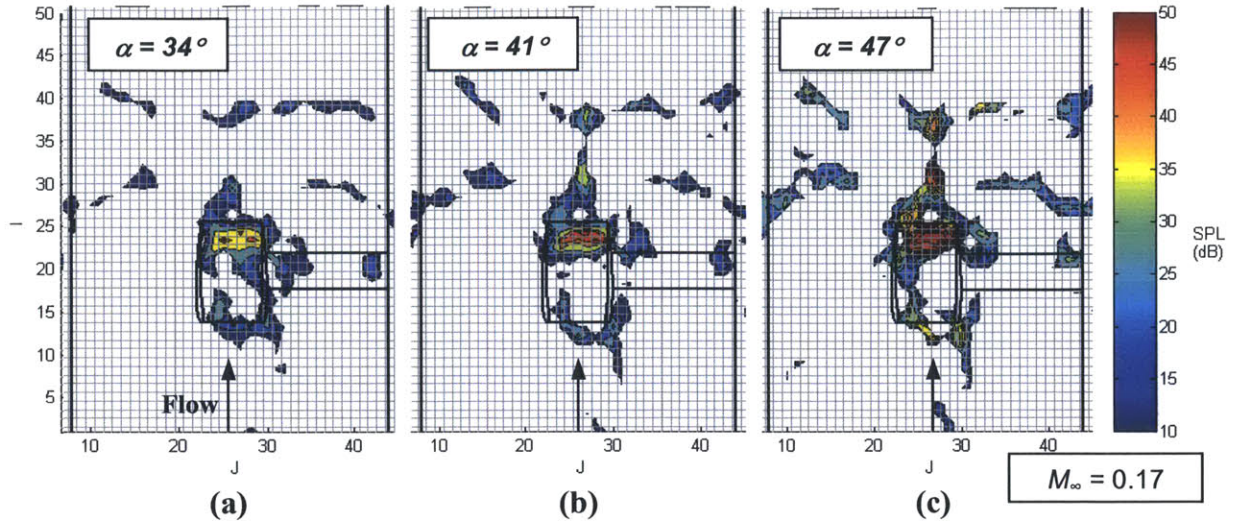

Figure 4.11. DAMAS noise source mapping of (a) 34°, (b) 41°, and (c) 47° stable swirl configurations shown for the 20 kHz one-third-octave band. Dominant noise source in all cases is turbulent scattering noise at nacelle exit. Noise level of downstream quadrupole source approaches that of the turbulent scattering source as swirl angle increases and the low-pressure core strengthens. Each grid box is 2.54 cm x 2.54 cm (1 in x 1 in).

4.3.2.1 Scattering Noise from Turbulent Eddies at Nacelle Exit

A previous study by Ffowcs Williams and Hall [9] demonstrates that noise generation is greatly increased by the presence of edges in turbulent flows at low Mach numbers. The distance between a turbulent flow structure, or eddy, and an edge of a physical body in the flow is a critical parameter in estimating the degree to which the edge will amplify sound generated by the eddy. The study showed that turbulent flow structures which satisfy

$$2kr \ll 1, \tag{4.15}$$

where k is the wave number[7] and r is the distance from the center of the turbulent structure to the edge, will have sound output increased by the factor $(kr)^{-3}$ over the sound of turbulent flow structures in open flows that do not satisfy this inequality [9]. Thus it is expected that the turbulent scattering noise of flow structures at the nacelle exit will dominate the noise of quadrupole sources in open flow far downstream of the swirl tube.

In the case of the swirl tube, scattering noise at the nacelle exit is generated from the turbulent boundary layers of the nacelle inner walls, turning vane surfaces and edges, and centerbody surfaces. Convecting downstream to the nacelle exit, they interact with the rear nacelle surfaces and edges. The scattering noise radiates with such efficiency in all directions that it is also detected at the nacelle inlet, though at lower noise levels, as shown in Figure 4.11.

[7] The wave number, k, is defined as $k = \omega/c$, where ω is the angular frequency and c is the speed of sound.

To further assess the hypothesis that turbulent scattering noise at the nacelle exit is the dominant noise source, scaling laws were applied to collapse the frequency spectra in the vicinity of the rear nacelle via DAMAS source integration methods discussed in Chapter 2. Equations 4.16 and 4.17 give expressions for scaled frequency and sound pressure level (SPL), respectively, as functions of a reference Mach number, M_{ref}, and scaling power n.

$$f_{scale} = f \cdot \left(\frac{M_{ref}}{M} \right) \tag{4.16}$$

$$SPL_{scale} = SPL + 10 \log_{10} \left(\frac{M_{ref}}{M} \right)^{n} \tag{4.17}$$

The scaling power, n, needed to collapse data based on Mach number varies by noise source according to theories by Lighthill and Ffowcs Williams and Hall [9, 19, 20]. The relationship between acoustic intensity and free stream Mach number or velocity given in Equation 4.3 suggests that turbulent scattering noise signatures will collapse to a reference Mach number using a scaling power of 5.0 while the relationship given in Equation 4.14 suggests quadrupole noise signatures collapse using a scaling power of 8.0. Table 4.2 lists various noise mechanisms and their respective scaling powers, n. Figure 4.12 shows that one-third octave spectra of noise sources integrated over the lower aft region of the 47° swirl case, indicated by the orange box in the figure inset. DAMAS processing was used to integrate noise sources in this region for cases with free stream Mach numbers ranging between 0.09 and 0.17. The figure shows that the spectra collapse well using a reference Mach number of 0.17 and a scaling power of n = 5.0, implying the presence of turbulent scattering noise at the nacelle exit.

Noise Mechanism	**Scaling Power, n**
Turbulent Scattering	5.0
Dipole	6.0
Quadrupole	8.0

Table 4.2. Scaling powers of various noise mechanisms based theories by Lighthill and Ffowcs Williams and Hall [9, 19, 20].

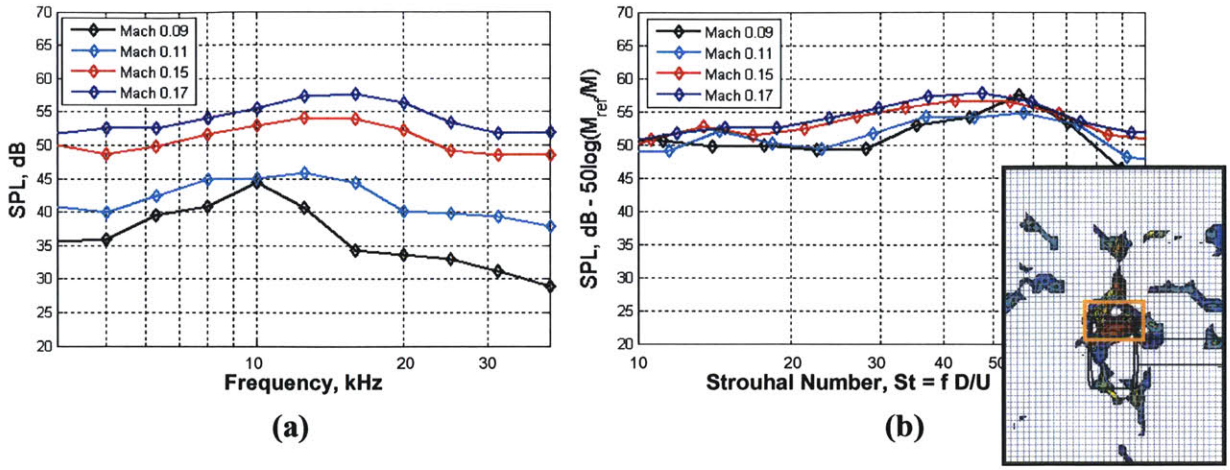

Figure 4.12. Lower aft region DAMAS noise source integrated one-third octave spectra of 47° stable swirl configuration at various free stream Mach numbers (a) without and (b) with Mach number scaling. Collapse of data in (b) using n = 5 indicates turbulent scattering. Integration region depicted by orange box in map inset.

The results also suggest that the turbulent scattering noise at the nacelle trailing edge is related to swirl angle by core Mach number, which is shown to govern SPL. This is first apparent in the narrowband spectra of Figure 4.7, where the noise spectra of the non-swirl 0° and stable 34° and 41°swirl cases share similar broadband peaks at frequencies between 6 and 13 kHz. The fact that this characteristic is present in the spectrum of the 0° non-swirl case but not in the vane-less empty nacelle configuration spectrum suggests that the spectral peaks are linked to turbulent structures shed from the turning vanes and scattered at the nacelle trailing edge. Though this presence in the 0° spectrum indicates that the characteristic is not caused by swirl, the spectra of the 34° and 41° swirl spectra clearly show that swirl of the exhaust flow does affect the nacelle trailing edge scattering noise. These spectral peaks, virtually identical in shape and peak SPL, increase in peak frequency with increasing swirl angle. To better quantify the relationship between peak frequency of these low frequency spectral peaks and swirl angle, the Strouhal number is first defined as

$$St = \frac{f \cdot L}{U}, \tag{4.18}$$

where f is frequency, U is a given flow velocity, and L is a characteristic length taken here as the swirl tube exit diameter. Thus for constant Strouhal numbers and characteristic lengths, increasing frequencies are attributable to increasing flow velocities. From CFD predictions and hotwire traverse measurements of wake velocity profiles, increasing swirl angle causes higher axial velocities in the core region of the swirl tube exhaust. Thus, using the maximum axial core velocities normalized to free stream, V_{core}/V_{∞}, for these configurations obtained from both hotwire velocity profiles and linear interpolation as listed in Table 4.3, their respective noise spectra can be collapsed in Strouhal number based on maximum core Mach number. The collapse of the low frequency spectral peaks in Figure 4.13 with $n = 5$ verifies the axial core Mach number, which increases with swirl angle, governs the turbulent scattering noise at the nacelle exit. The spectrum of the 47° swirl case was included in this analysis despite its

distinctly different shape as compared to the spectra of the 0°, 34°, and 41° configurations. Though the peak frequency of the broadband peak in the 47° spectrum approximately shares the core Mach number-based data collapse of Figure 4.13 with the 0°, 34°, and 41° cases, its smooth shape across all frequencies is implicit of the flat characteristics of vortex breakdown spectra, suggesting that the 47° swirl configuration is a potential transition case between stable and unstable swirling flows.

α	V_{core}/V_{∞}
0°	1.00
34°	1.30
41°	1.54
47°	1.75

Table 4.3. Maximum core velocities normalized to free stream of non-swirl and stable swirl configurations[8].

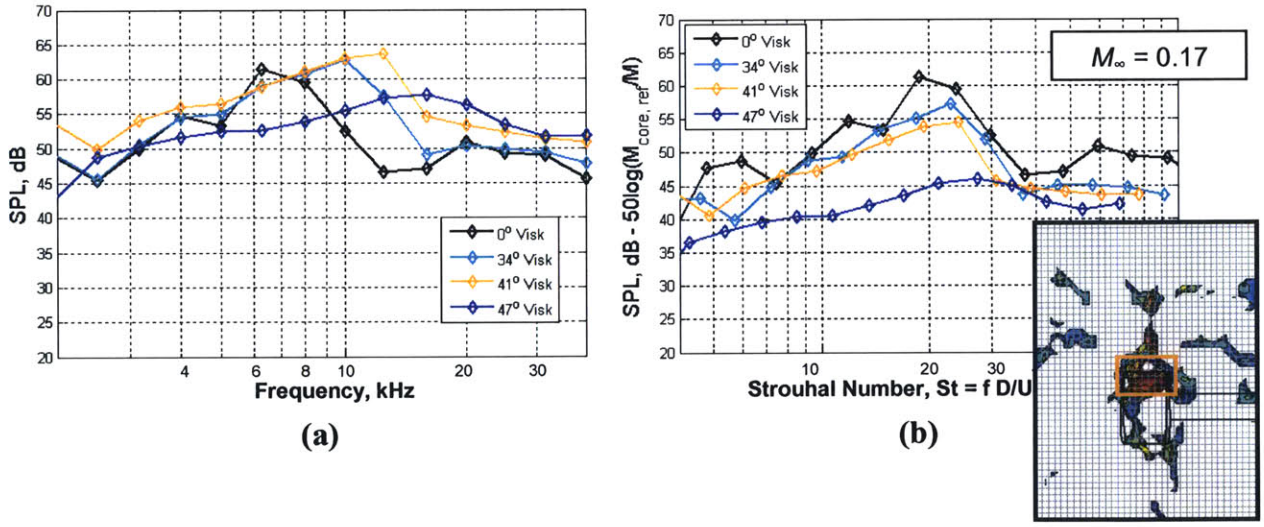

Figure 4.13. Nacelle exit region integrated one-third octave spectra of 0°, 34°, 41°, and 47° stable swirl configurations at free stream M = 0.17 (a) without and (b) with core Mach number scaling with $n = 5$. Collapse of data in (b) using core Mach numbers suggests spectral peaks are related to swirl angle via nacelle exit velocities. Source noise integration region depicted by orange box in map inset.

[8] Values for 34° and 47° cases were calculated from measured axial velocity profiles and used to linearly interpolate the normalized maximum core velocity of the 41° case. Value for the non-swirl 0° case was assumed to be 1.00 given that the relatively constant flow area through the swirl tube neither accelerates nor decelerates the exhaust flow in the absence of swirl.

4.3.2.2 Quadrupole-type Mixing Noise of Swirling Flows

The assessment of aerodynamic sound generation of turbulent flows by Ffowcs Williams and Hall mentioned in the previous subsection stresses the importance of the relationship of noise generated by a turbulent structure to its distance to an edge of a physical body in the flow. The study showed that sound generated by eddies in open flow that are sufficiently far from an edge such that

$$\sqrt{kr} \gg 1 \tag{4.19}$$

will not be significantly amplified by the edge [9]. Given this lack of amplification, it is expected that the swirl tube quadrupole sources located downstream of the nacelle exit will not be as dominant as the noise generated by turbulent scattering at the nacelle trailing edge.

The quadrupole sources downstream of the nacelle exit are consequent of the low-pressure, high-velocity core flow mixing with the swirling annular flow. This open-field turbulent mixing radiates noise far less efficiently than the scattering of turbulent flow structures at the nacelle exit and is thus less prevalent in the noise source maps of Figure 4.11. The quadrupole source strengthens in SPL output with increasing swirl angle, yielding a noise level similar to that of the turbulent scattering noise in the 47° swirl case shown in Figure 4.11c due to the increased core axial velocities generated as a consequence of highly swirling outer flow region as identified in the previous subsection. The increase in the axial velocity of the viscous core region leads to a larger difference between the high velocities of the viscous core and the lower axial velocities of the surrounding helical flow, intensifying the downstream turbulent mixing of these two flows. This intensification of downstream turbulent mixing is manifested acoustically as increased noise generated by the quadrupole.

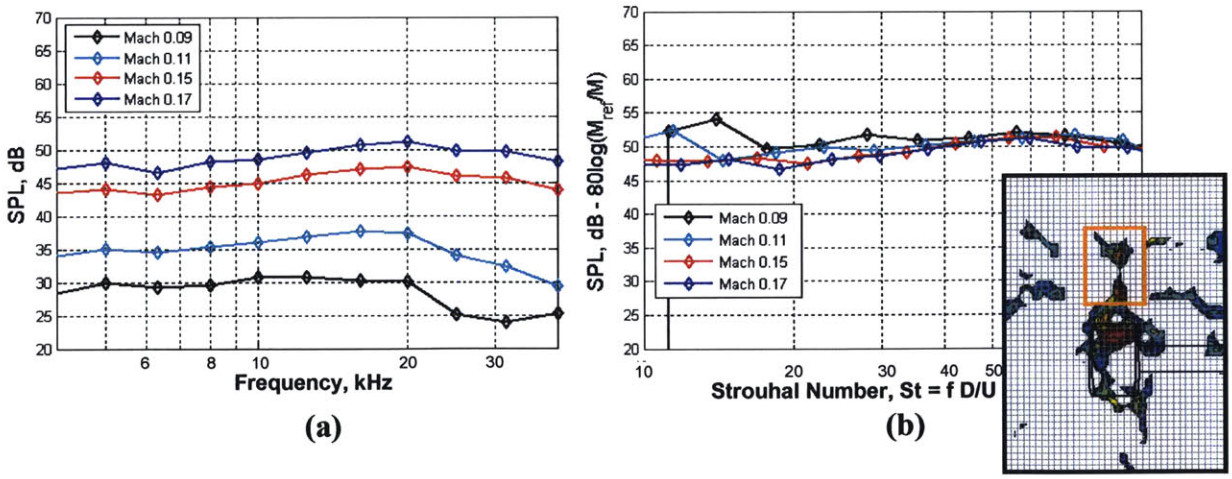

Figure 4.14. Free field source integrated one-third octave spectra of 47° stable swirl configuration at various free stream Mach numbers (a) without and (b) with Mach number scaling. Collapse of data in (b) using n = 8 indicates quadrupole-type mixing noise. Source integration region depicted by orange box in map inset.

Mach number scaling is applied to the spectra of noise sources integrated over the free field zone aft of the nacelle exit. Figure 4.14 shows that one-third octave spectra of noise sources integrated over this region for the 47° swirl case at various free stream Mach numbers collapse well with $n = 8$, typical of open-field mixing noise, corroborating the hypothesis that the downstream noise sources seen in Figure 4.11 are of quadrupole-type.

4.3.3 Acoustic Signature of Swirling Flows with Vortex Breakdown

The onset of vortex breakdown, the burst of the stable streamwise vortex, is exhibited by configurations with maximum swirl angles equal to or greater than 53° and drastically alters the aero-acoustic behavior of the swirl tube as compared to that of stable cases discussed in the previous sections. The audible, white noise-like "crackle" sound of vortex breakdown corroborates the flat noise spectra in Figure 4.7 characteristic of white noise. The burst vortex manifests itself as a turbulent bubble of unsteady flow centered within one nacelle exit diameter of the nacelle trailing edge. This location of the turbulent bubble effectively eliminates the development of the high-velocity, low-pressure core stream downstream of the nacelle exit inherent to stable swirling cases. Instead, the quadrupole sources and turbulent structures of the burst vortex scatter off nearby nacelle and centerbody surfaces and edges, radiating efficiently at the nacelle exit. The DAMAS noise source maps of Figure 4.15 confirm that the 53°, 57°, and 64° swirl cases all demonstrate noise sources concentrated at the nacelle exit, generating peak local noise levels over 10 dB higher than the noise sources of the stable configurations shown in Figure 4.11.

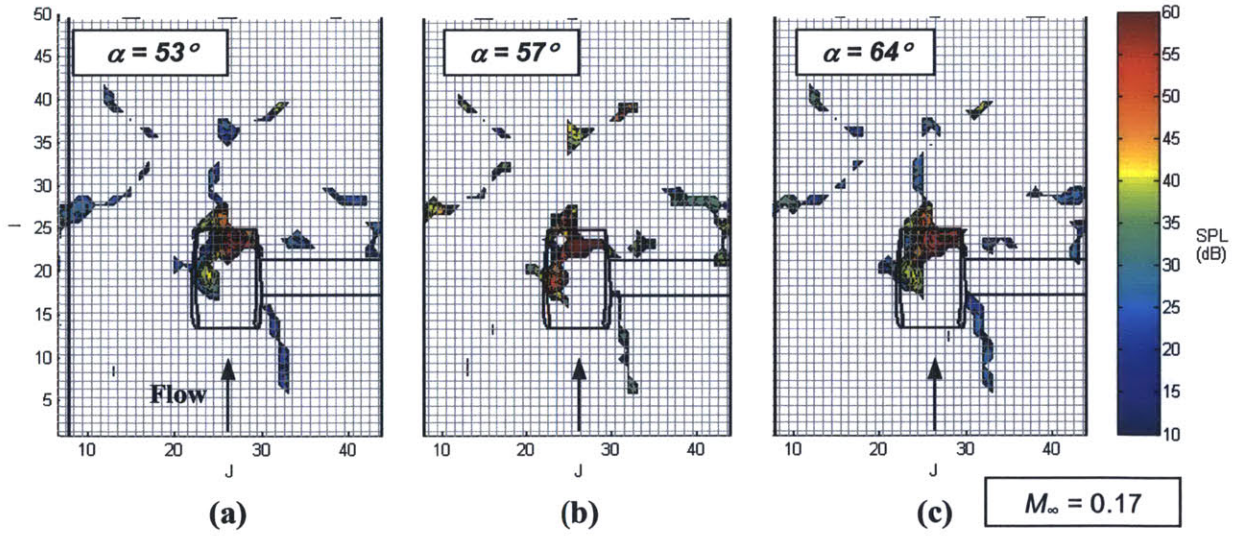

Figure 4.15. DAMAS noise source mapping of (a) 53°, (b) 57°, and (c) 64° swirl configurations with vortex breakdown shown for the 20 kHz one-third-octave band. Dominant noise source in all cases is burst vortex turbulence and quadrupole scattering noise radiating efficiently as a compact source at the nacelle exit. Each grid box is 2.54 cm x 2.54 cm (1 in x 1 in).

Mach number scaling is applied to assess the identities of the noise mechanisms associated with vortex breakdown cases. Given the hypothesized presence of both quadrupole-type and turbulent scattering noise sources near the nacelle exit, a scaling power between that of turbulent scattering ($n = 5$) and that of quadrupole sources ($n = 8$) is suggested. It is found that a scaling power of $n = 7.5$ best collapses the spectra of the 57° swirl case, shown in the one-third octave scaled spectra in Figure 4.16.

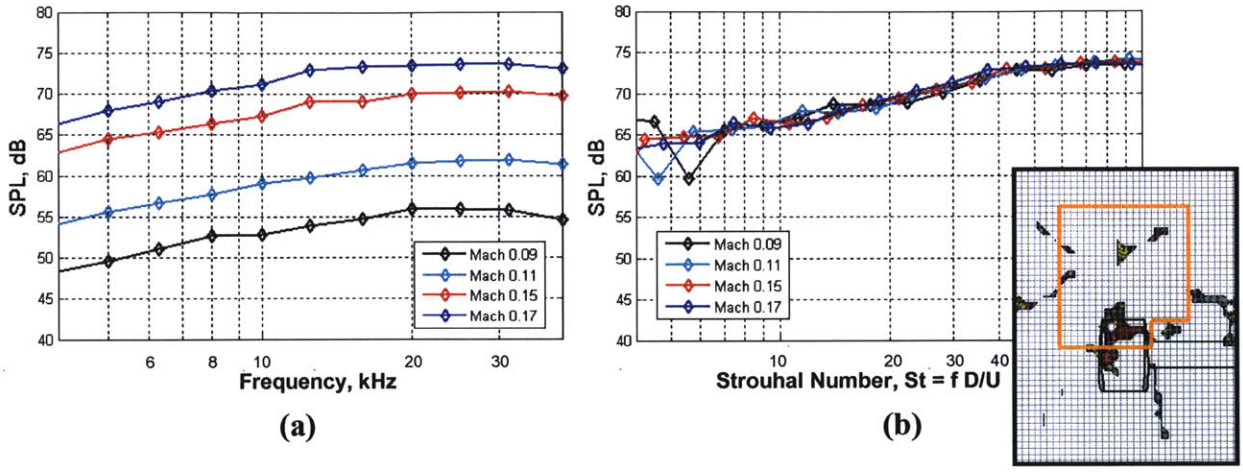

Figure 4.16. Aft region DAMAS noise source integrated one-third octave spectra of 57° swirl configuration with vortex breakdown at various Mach numbers (a) without and (b) with Mach number scaling. Collapse of data in (b) using n = 7.5 suggests presence of scattering and open-flow quadrupole-type noise mechanisms. Source integration region depicted by orange lines in map inset.

The results presented in this section suggest that vortex breakdown should be avoided in the design of swirling flow devices for quiet drag due to the additional scattering noise generated from unsteady flow structures of the burst vortex. The aircraft integration assessment in Chapter 5 thus considers practical applications of high-drag stable swirl cases without vortex breakdown.

4.4 Outcomes of Swirling Flow Aerodynamic and Aero-acoustic Assessment

The key outcome of this chapter is that stable swirling flows are quiet due to the distributed noise mechanisms, including scattering noise of turbulent structures at the nacelle trailing edge and quadrupole-type noise sources in the downstream free field. As such, the swirl tube should be designed so that a stable swirling exhaust flow is generated with the highest achievable swirl angle without encountering vortex breakdown. Avoiding vortex breakdown, as in the case of the 47° swirl configuration, maximizes drag output from the device while maintaining the low noise levels associated with the turbulent scattering noise and open field quadrupole noise sources of stable swirling flows. Crossing this threshold to vortex breakdown leads to a substantial increase in noise spectrum level of 10 to 15 dB at all frequencies due to the increased scattering noise of turbulence and open-flow quadrupole sources at the rear nacelle edges and surfaces in the presence of the burst vortex.

A second outcome of the analysis is the success of the DAMAS processing technique in quantifying and assessing the acoustic characteristics of volume sources. As mentioned in Chapter 2, the history of DAMAS applications includes the processing of mainly leading and trailing edge-type sources [3]. The swirl tube presented the QFF with a first opportunity to test the DAMAS method on volume sources. As shown, the technique proved to be an invaluable tool in measuring and quantifying the open-flow volume sources associated with swirling flows with enhanced precision and advantage over older beamforming techniques.

Chapter 5

Aircraft Integration Considerations

5.1 Requirements for Aircraft Integration

As outlined in Chapter 1, the purpose of swirl tube technology is the quiet generation of drag sufficient for mid-size aircraft during approach. The aerodynamic and aero-acoustic analyses of Chapter 4 demonstrate that quiet drag from swirling flows is achievable at model scale. Full-scale aircraft integration of swirl tube technology, however, imposes further requirements on swirl tube design and performance beyond those necessary for successful model-scale wind tunnel testing. The focus of this chapter is the identification of aircraft integration requirements for quiet drag technology and the assessment of the swirl tube as a practical quiet drag concept.

Successful swirl tube aircraft integration configurations must meet aircraft-specific approach drag and noise requirements while remaining realistically installable. That is, the swirl tube architecture for a certain installation configuration must be such that it is compatible with the aircraft's available space for quiet drag devices. Similarly, the locations of swirl tube installations must be such that aircraft performance is not significantly affected in any phase of flight. For example, integration configurations involving externally mounted swirl tubes must have the capacity to deactivate swirl tube drag generation for takeoff, climb, and cruise conditions where additional drag is not desired. Lastly, the drag-generating capability of a swirl tube must be impervious to upstream flow non-uniformities, whether introduced temporarily by a sudden change in flight condition or permanently due to installation-related obstacles.

In Section 5.2, three mounting configurations are considered to assess the full-scale drag capability, noise generation, and installation benefits and challenges of swirl tubes integrated onto the experimental silent aircraft SAX-40. The assessment shows that engine-integrated swirl tubes are the best of the three integration configurations as they are most capable in terms of effective drag generation with minimal weight cost. As a result, Section 5.3 examines

performance benefits of engine-integrated swirl tubes on conventional tube-and-wing aircraft of today. Finally, analyses of aerodynamic and aero-acoustic wind-tunnel test results assess the effects of upstream flow non-uniformities on swirl tube drag and noise performance in Section 5.4.

5.2 Full-Scale Swirl Tube Drag and Acoustic Performance

The full-scale performance capabilities of the swirl tube in terms of drag generation and noise production are evaluated by assessing installation requirements and configurations on the conceptual silent aircraft design SAX-40. Based on design objectives of the SAX-40, certain quiet approach options of the aircraft require acceptable swirl tube integration configurations to provide 100 counts of drag[9] such that the approach glide slope of the aircraft can be increased for improved noise attenuation. To comply with the SAX-40's critical noise target, an acceptable full-scale swirl tube integration configuration must generate an OASPL no greater than 63 dBA as observed from outside airport boundaries.

The configurations evaluated in this and the following sections include centerbody-mounted, winglet-mounted, and engine-integrated swirl tube installations. Discussion of each configuration addresses the balance of swirl tube full-scale drag and acoustic performance with installation concerns, such as added weight, deployment, and interference with aircraft performance. A summary of configuration properties is tabulated in Table 5.1. Of the three configuration types shown in Table 5.1, the 6-tube engine-integrated installation is suggested to be most favorable, capable of potentially providing 243 drag counts (over twice the target amount) at an estimated OASPL of 69 dBA. Though this exact configuration fails to meet the SAX-40 noise target, a similar reduced-swirl configuration could potentially reduce the OASPL below 63 dBA by sacrificing drag capability.

In evaluating swirl tube integration configurations, the following assumptions were made.

- All configurations were evaluated assuming the use of 47° aluminum alloy turning vanes. This particular vane angle was chosen based on its high-drag, low noise characteristics demonstrated by model-scale wind tunnel testing. Aluminum alloy, chosen for its high strength-to-weight, is commonly used in aeronautical applications.

- Configuration weights were estimated using material densities and full-scale turning vane volumes.

- An additional 45.4 kg (100 lbs) were added to all installations to account for the use of actuators.

- Where necessary, weights for additional ducting were estimated based on duct length using methods given in Raymer [25].

[9]One drag count is 1/10,000 of a C_D. For SAX40 drag counts, the reference area for C_D is the planform area of the aircraft, 836 m^2 (8,998 ft^2).

- Full-scale drag levels and acoustic signatures were obtained by scaling those obtained from model-scale wind-tunnel tests. Full-scale drag coefficients referenced to swirl tube area are determined using the Reynolds number correction of the model-scale viscous drag components given by Equation 4.2. Equation 5.1 converts swirl tube area-referenced drag coefficients to SAX-40 planform area-referenced drag coefficients, where N is the number of swirl tubes.

$$C_{D_{planform}} = N \cdot \frac{A_{tube}}{A_{planform}} \cdot C_{D_{tube}} \tag{5.1}$$

	Centerbody Mounted	Propulsion System Int. (1)	Propulsion System Int. (2)	Winglet (1)	Winglet (2)
Number of Swirl Tubes	6	2	6	2	2
Swirl Tube Diameter	0.8 m (2.62 ft)	1.20 m (3.93 ft)	1.20 m (3.93 ft)	1.57 m (5.15 ft)	2.0 m (6.56 ft)
Drag Counts	29	81	243	36	58
OASPL (dBA)	48.0	65.6	70.4	45.3	45.9
Additional Weight	771 kg (1,700 lbs)	351 kg (773 lbs)	1,052 kg (2,320 lbs)	674 kg (1,487 lbs)	1,297 kg (2,860 lbs)
Drag Force	4.81 kN (1,082 lb_f)	13.62 kN (3,062 lb_f)	40.86 kN (9,185 lb_f)	6.08 kN (1,366 lb_f)	9.81 kN (2,205 lb_f)
Drag to Weight	0.64	3.96	3.96	0.92	0.77
Added Advantages	No interference with cruise perf.	Integration with thrust reverser	Integration with thrust reverser	Doubles as yaw control	Doubles as yaw control
Added Concerns	Exhaust/TE interaction	Deployment, Noise	Deployment, Noise	Deployment	Deployment, Weight

Table 5.1. Calculated full-scale swirl tube properties for various SAX-40 integration configurations. For each parameter (row), best value is indicated in green; worst value is indicated in red. The propulsion system-integrated configurations are favored for their high drag to weight ratio.

5.2.1 Centerbody-Mounted Swirl Tubes

The main challenge in the integration of swirl tubes into the SAX-40 centerbody is selecting a location for the turning vanes and additional inlet and exhaust ducting. Since the swirl tubes for this configuration are embedded within the body of the aircraft, the selected location must have duct paths forward and rearward of the turning vanes that are clear of other objects, yielding a potentially substantial weight penalty. This presents difficulties in locating the swirl tubes within the central body of the aircraft, with the passenger cabin and embedded engines occupying much of the aircraft's volume near the centerline as shown in the SAX-40 planform and internal layout concept drawings of Figure 5.1b. Fuel tanks and outer engines occupy the portions of the centerbody surrounding the passenger cabin, thus limiting potential swirl tube locations in the

spanwise direction to beyond 9.14 m (29.99 ft) from the aircraft centerline. Since the minimum thickness of the wing at this location limits the swirl tube diameter to 0.8 m (2.62 ft), 3 swirl tubes can be fit side-by-side in each wing (Figure 5.1c).

Doors on the bottom and trailing edge of the wing are actuated to provide flow through the centerbody-mounted turning vanes, shown in Figure 5.1a. Though exhaust flow at the trailing edge of the wing via split exit doors could potentially interfere with the aircraft's elliptic lift distribution to generate additional induced drag on approach, the low levels of drag provided by the six small swirl tubes make this integration configuration unattractive, contributing only 29 drag counts to the total aircraft drag on approach. Considering the additional weight required for ducting comprises nearly 35% of this configuration's total weight of 771 kg (1,700 lbs), the low drag-to-weight ratio of 0.64 renders centerbody-mounted swirl tubes impractical for integration into the SAX-40 aircraft. The six swirl tubes' relatively low combined noise output of 48 dBA OASPL as observed outside airport boundaries on approach does make this configuration a potential option for supplementing the aircraft with up to 29 drag counts at minimal noise penalty as part of a larger quiet drag system.

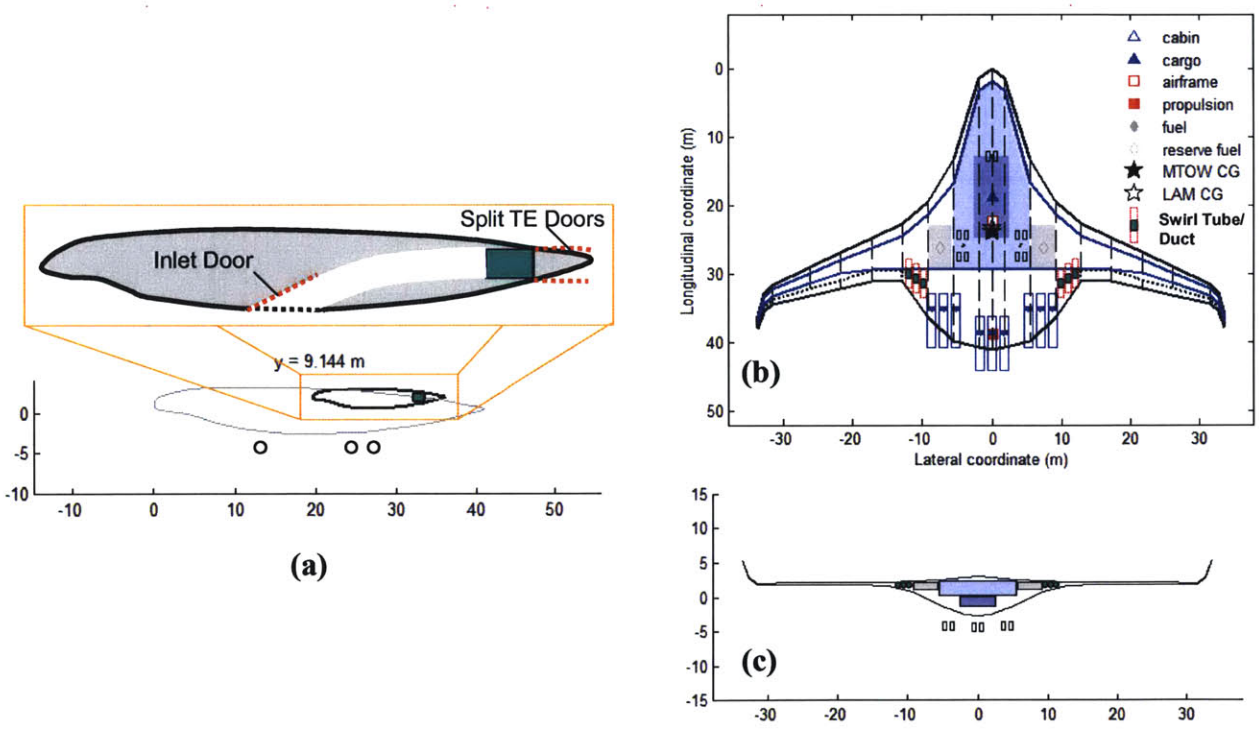

Figure 5.1. Three-view layout of SAX-40 with six centerbody-mounted swirl tubes (green). In top view (b), additional ducting for inlet and exhaust streams are shown as dashed red lines. Actuated inlet doors and split trailing edge doors for ducting are shown in (a). As seen in (c), fuel tank placement and decreasing wing thickness limit the size and number of swirl tubes for the configuration. Figures adopted from [15].

5.2.2 Winglet-Mounted Swirl Tubes

Perhaps the most unique of the three integration concepts presented in this chapter are the two variations of winglet-mounted swirl tubes. The analysis suggests these concepts to be the quietest configurations, potentially generating drag counts of 36 and 58 for respective diameters of 1.57 m (5.15 ft) and 2.00 m (6.56 ft) with OASPLs less than 46 dBA. Successful integration of winglet swirl tubes requires the actuation of turning vanes for both non-swirl and swirl modes such that the drag generated during approach from the vanes in swirl mode is not present during takeoff, climb, and cruise and the additional drag at cruise due to the presence of the swirl tube nacelles is comparable to that of the conventional winglets.

The dimensions of these two configurations were chosen to approximate the size of a winglet tube produced by rolling the proposed 4.01 m (13.16 ft) long winglet of SAX-40 into a circle. Matching the proposed swirl tube nacelle wetted area to the present winglet wetted area ensures that no additional skin friction drag is added to the aircraft. Figure 5.2 shows a front view of the SAX-40 with 1.57 m (5.15 ft, left) and 2.00 m (6.56 ft, right) diameter swirl tubes replacing the winglets. This is not the first instance of unconventional winglet concepts for aircraft; in 2001, Aviation Partners tested a Gulfstream II with looped winglets called "spiroids". The prototype spiroid winglets, seen mounted on the test aircraft in Figure 5.3, reduced the cruise fuel consumption by over 10 percent by eliminating concentrated wingtip vortices responsible for nearly half of the induced drag experienced in cruise [12]. As a closed-loop, the spiroid winglet possesses no distinct wingtip edge on which the wingtip vortex typically develops for a conventional winglet. Winglet swirl tubes could attain this type of enhanced cruise performance if given the ability to stow or straighten turning vanes for a non-swirl operation mode. As with the spiroid winglets, care must be taken in assessing the additional structural loads on the wings due to the presence of winglet swirl tubes for safe operation during all flight phases. Though this structural issue is recognized here as a potential drawback to winglet-mounted swirl tube configurations, a preliminary wing/winglet structural analysis is not presented.

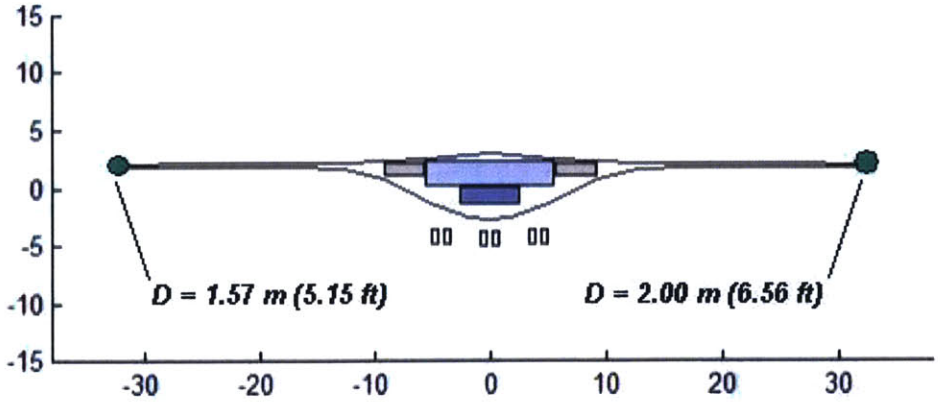

Figure 5.2. Front-view of SAX-40 with winglet-mounted swirl tubes of various diameter (green). Circumferences were approximated by "rolling" the length of the existing 4.01 m (13.16 ft) winglets.

Figure 5.3. Aviation Partners Gulfstream II test aircraft with looped "spiroid" winglets. Flight testing of spiroid winglets showed a 10 percent reduction in cruise fuel consumption, achieved by eliminating concentrated wingtip vortices responsible for nearly half of the induced drag experienced in cruise [12].

The benefits of winglet swirl tubes thus depend on the ability to actuate the devices into swirl and non-swirl modes. Switching from one mode to the other can be achieved in one of two ways: (1) changing the vane turning angles from 0° for non-swirl operation to ~47° for swirl operation via actuation of the entire vane and/or trailing edge or (2) stowing the vanes completely within the duct walls for non-swirl operation. Though keeping the vanes in the flow, straight, for non-swirl operation would add skin friction drag to the aircraft in cruise, this option is simpler to actuate mechanically than stowing the vanes completely. The skin friction coefficient of 20 straight vanes deployed during cruise is estimated using the Reynolds number-based empirical flat plate skin friction relation for turbulent boundary layers given in Equation 5.2 [13].

$$C_f = 0.455 \cdot \frac{1}{\left[\log\left(\mathrm{Re}_L\right)\right]^{2.58}} \tag{5.2}$$

The drag coefficients (and thus drag counts) of winglet swirl tubes in non-swirl mode are subsequently calculated using the ratio of swirl tube wetted area to SAX-40 planform area, similar to the expression given in Equation 5.1. Data from Table 5.2 shows that skin friction contributions from the swirl tube nacelle only (stowed turning vanes) and for the swirl tube nacelle with 20 straight vanes are not substantially higher than the 1.22 drag counts of skin friction drag calculated for the SAX-40 winglets during cruise, implying that replacing conventional winglets with winglet swirl tubes in a non-swirl mode might not significantly impact cruise performance.

	Swirl Tube Nacelle Only	Swirl Tube, 20 Straight Vanes	Additional Cruise Drag Counts above Winglet Drag
Drag Counts, D = 1.57 m (5.15 ft)	1.28	2.5	**1.28**
Drag Counts, D = 2.00 m (6.56 ft)	2.02	4.88	**3.66**

Table 5.2. Full-scale winglet swirl tube skin friction drag counts for SAX-40 cruise conditions. Data in last column presents estimated cruise skin friction of swirl tube nacelle and 20 straight vanes above that generated by the 4.01 m (13.16 ft) winglet, approximately 1.22 counts. All drag counts are shown for two devices, one on each wing tip.

5.3 Swirl Tubes as Engine Air Brakes

The analysis of engine-integrated swirl tubes, found to be the best integration option of the three assessed in terms of drag capability and weight penalty, is presented in this section for both current and future aircraft. As in the previous sections, Section 5.3.1 assesses the full-scale performance characteristics of engine-integrated swirl tubes as well as the challenges and benefits of practical installations. The concept of engine-integrated swirl tubes is introduced as an engine air brake in [28, 29] given the net thrust reduction provided by swirl vanes pumped by an upstream fan stage. Since engine-integrated swirl tubes were found to be the best integration option of those assessed, Section 5.3.2 extends the concept to mid-sized conventional tube-and-wing aircraft, the results indicating that the increase in glide slope made possible by the high levels of drag generated can yield a potential overall aircraft noise reduction of 6 dB on approach.

5.3.1 Engine Air Brakes for SAX-40 Applications

The success of the engine-integrated swirl tubes derives from the high amounts of drag, or more precisely, thrust reduction[10], generated by swirl vanes located aft of the fan rotor stage in fan ducts of a distributed propulsion system. The three Granta 3401 engine clusters of the SAX-40 are each composed of three fans driven by a single gas generator through a transmission system [15]. The outer two of the three fan stages in each engine cluster have ducting with space available for swirl vane installations. By choosing to position swirl vanes downstream of an engine fan stage, flow is "pumped" through the turning vanes, effectively increasing the swirl tube inlet capture area by increasing the mass flow through the device as well as the aerodynamic loading on the vanes. A computational study by Shah tested the effects of an upstream fan stage on the aerodynamic performance of swirling flows [29]. Results for pumped swirl tube exhaust flow for 47° turning vanes shown in Figure 5.4b indicate maximum core Mach numbers twice those of unpumped, ram pressure driven vanes shown in Figure 5.4a. Consequently, results suggest an increased net thrust reduction (effective drag coefficient) of approximately 3 for an

[10] Rather than drag generation, the term thrust reduction is used here since the engines are still producing idle-setting thrust at levels sufficient to meet emergency approach go-around requirements. Thus any drag provided by swirl vanes in a fan duct serves to reduce the overall engine level thrust.

idle fan pressure ratio of 1.08, capable of supplying the aircraft with an additional 81 or 243 drag counts for two or six engine-integrated sets of swirl vanes, respectively. This idle fan pressure ratio, though low compared to those of existing engines, assumes bypass ratios associated with next-generation turbofan engines.

Propulsion-integrated swirl vanes are also beneficial in terms of weight savings over other integration configuration. With the distributed propulsion system outer fan inlet and exhaust ducting already in place, the swirl vanes require no additional ducting or nacelle, as is required of both the centerbody- and winglet-mounted installations. This renders the engine-integrated swirl vanes most efficient in terms of weight, yielding extremely favorable drag-to-weight ratios of 3.96.

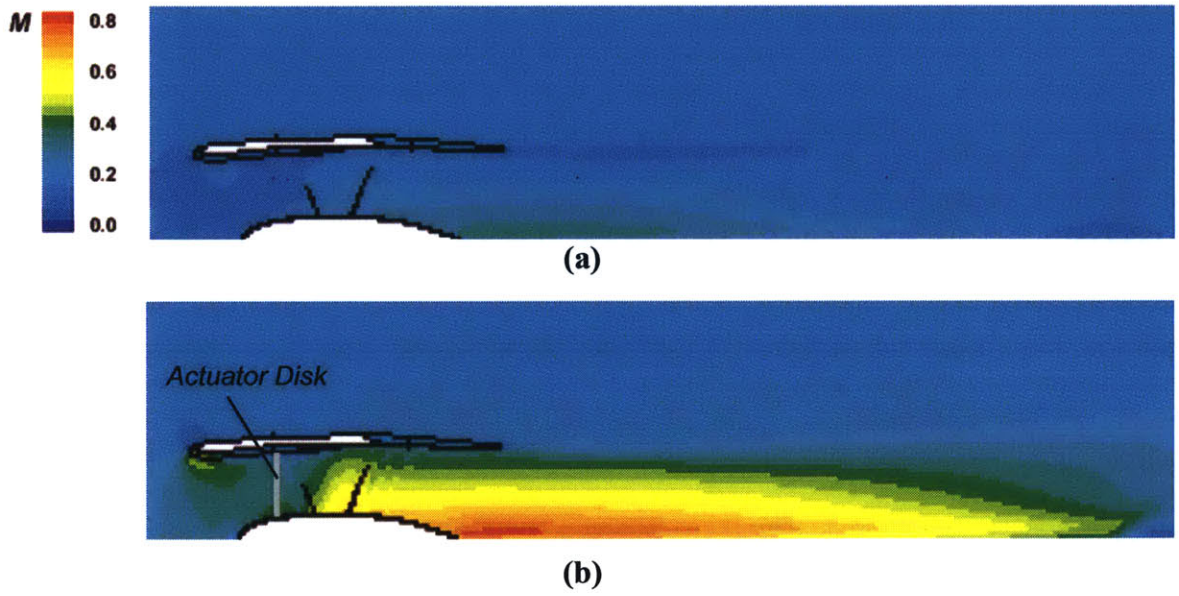

Figure 5.4. Axial Mach numbers for (a) ram pressure driven and (b) fan-stage pumped 47° swirl cases. Pumped case assumes upstream idle fan pressure ratio of 1.08. Pumping doubles maximum core Mach number, increasing both drag and noise generation [29].

Though pumping of the swirl tube provides great increases in thrust reduction, the high Mach numbers in the exhaust flow generate higher noise levels than the ram pressure driven case. Given the difficulty of acoustic estimation, the noise from pumped swirling flows would be best quantified by aero-acoustic wind-tunnel experiments, such as those described in this thesis to quantify noise mechanisms of ram-air driven swirl tubes. In lieu of these results, the noise increase due to pumping was estimated by applying Mach number scaling to the core of the unpumped 47° swirl case following the hypothesis that core Mach number governs SPL in stable swirling flows[11]. A scaling power of $n = 7.0$ was used to balance the turbulent scattering ($n = 5$-6) and quadrupole ($n = 8$) noise mechanism contributions, leading to the estimated SPL increase given by Equation 5.3.

[11] See Section 4.3.2.1.

$$SPL_{47^\circ,pumped} = SPL_{47^\circ,unpumped} + 10\log\left(\frac{M_{pumped}}{M_{unpumped}}\right)^7$$
$$SPL_{47^\circ,pumped} = SPL_{47^\circ,unpumped} + 24 \text{ dB} \tag{5.3}$$

The preliminary bias estimate of 24 dB increases the full-scale OASPL of the 2-tube and 6-tube engine integrated swirl vanes to 65.6 dBA and 70.4 dBA, respectively. Though these levels exceed the SAX-40 target noise goal of 63 dBA as observed outside an airport boundary on approach, swirl angle configurations less than 47° could be employed to reduce the pumped exhaust core Mach number, decreasing the noise production at the cost of thrust reduction

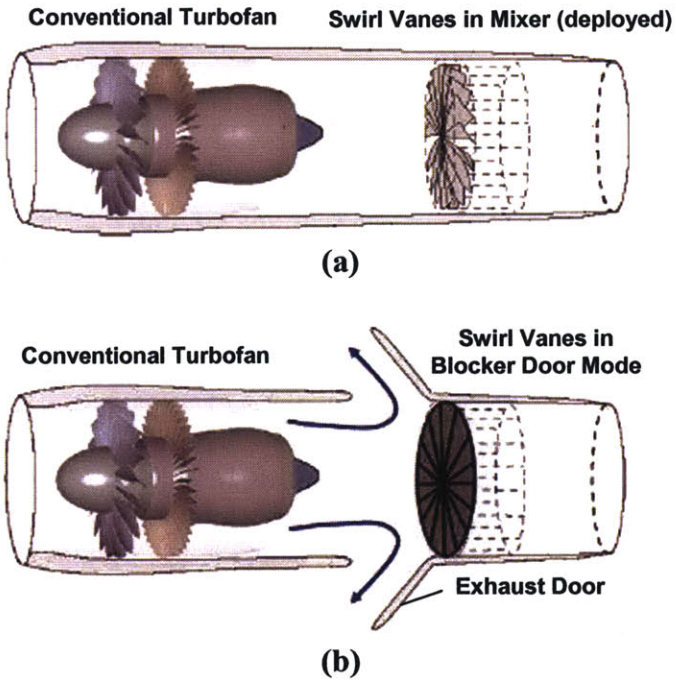

Figure 5.5. Concept drawings of swirl vanes deployed aft of turbofan engine in (a) swirl mode and (b) thrust reverser mode. In thrust reverser mode, exhaust doors open in nacelle to expel flow radially [29].

The location of the swirl vanes for the proposed engine air brake presents the possibility for integration into a thrust reverser package as well. Turning vanes with the ability to schedule from a straight, non-swirl position to an angled, swirl position could schedule to a third, fully closed position for thrust reversing. Figure 5.5 shows concept drawings of swirl vanes in swirl mode (5.5a) scheduling to fully closed blocker door thrust reverser mode (5.5b). When acting as blocker doors, the swirl vanes prevent flow from exiting rearward, forcing flow to expel radially through exhaust doors located in the engine nacelle. Integrating swirl vanes into a thrust reverser package has the potential for a substantial weight savings, since blocker doors are typically the heaviest components of a thrust reverser system. Thus, with the installation of exhaust doors in

the nacelle through which flow can be exhausted radially, the added weight of swirl vanes for an engine air brake application is largely offset by their functional duality for both quiet drag generation and thrust reversing.

5.3.2 Engine Air Brake Applications for Conventional Aircraft

As presented in the previous section, the concept of using swirl vanes as an engine air brake provides significantly greater effective drag over ram-air driven swirl vanes with the potential for substantial weight savings through functional integration into a thrust reverser package. Though this concept was initially analyzed for installation on the SAX-40 aircraft, its performance advantages are equally applicable to current conventional mid-sized aircraft. A complete analysis of noise reduction and effective drag capability for current aircraft is presented via case study in Shah et al. [28]. This section provides a synopsis of these results.

The analysis in [28] examines the net estimated noise reduction for the Boeing 737-700A, 767-300, and 777-200ER aircraft as a result of the increased glide slope angles achievable with additional thrust reduction from engine air brakes. Table 5.3, adopted from [28], summarizes the findings of this analysis. The overall approach noise, given for the aircraft at 3° glide slopes in the third column and obtained from FAA Advisory Circular 36-3H, shows all three aircraft to have an approach noise near 90 dBA. Values in this column can be compared with the noise levels of ram-air driven swirl tubes as well as the noise levels of engine air-brakes with a fan stage pressure ratio of 1.08, given in the fourth and sixth columns, respectively. For each of these cases, the noise level of the 47° swirl case is scaled both geometrically to the full-scale diameter of the respective aircraft engine as well as for aircraft approach velocity. The noise levels of the full-scale engine air brakes were estimated from these baseline figures using core Mach number scaling similar as presented in the previous section. For a conservative estimate, the increase in noise level was computed using Equation 5.3 with $n = 8.0$, yielding an increase of 27 dB for each case as tabulated in the sixth column. Comparing the fourth and sixth columns to the third column, it is shown that the full-scale noise levels of ram-air driven swirl tubes and engine air brakes are over 10 dBA lower than the overall approach noise of the respective aircraft, indicating that integration of either of these quiet drag methods would bear little impact on the overall noise level of the aircraft.

The data in the fifth and seventh columns present the change in glide slope due to the additional drag from ram-air driven swirl vanes and engine air brakes, respectively, as well as the consequent decrease in overall approach noise level. These results suggest that passive, ram-air driven swirl tubes sized to engine diameter could provide a 2.0 dB reduction in approach noise level while engine air brakes of the same size could provide an approach noise reduction of over 6.0 dB.

Aircraft	Powerplant	3° Glideslope Overall Approach Noise	Ram Air Swirl Tube Noise	Δ Glideslope (from 3°)/ Δ Noise	Engine Air-Brake Noise ($\pi = 1.08$)	Δ Glideslope (from 3°)/ Δ Noise
737-700A	CFM56-7B20	86.6 dBA	46.3 dBA	+0.8°/-2.0 dB	73.7 dBA	+3.2°/-6.3 dB
767-300	CF6-80A2	89.2 dBA	51.3 dBA	+0.9°/-2.3 dB	78.7 dBA	+3.7°/-7.0 dB
777-200ER	GE90-90B	88.8 dBA	50.1 dBA	+1.0°/-2.5 dB	77.5 dBA	+4.0°/-7.4 dB

Table 5.3. Reduction of approach noise for various civil aircraft due to integration of engine-scale ram-air swirl tubes and/or engine air brakes. Results indicate approach noise level reductions of 2+ dB and 6+ dB, respectively, for these two integration methods [28].

5.4 Swirl Tube Performance with Upstream Flow Non-Uniformity

Aerodynamic and aero-acoustic wind tunnel tests confirm that the effects of upstream flow non-uniformities on swirl tube drag and noise performance are minimal. Device functionality in the presence of inlet non-uniformities is critical to aircraft integration of the swirl tube since non-ideal inlet flows associated with real-world flight conditions are common to internal flow devices. Non-uniformities in actual inflows can derive from device angles of attack, curved inlet ducting, wake-producing support structures, etc. The analyses presented in this section demonstrate the swirl tube's ability to generate drag coefficients of ~0.7 with minimal noise penalty when subjected to circumferential inlet flow distortions, upstream blade wakes, and small angles of attack, suggesting that the concept is not sensitive to upstream flow non-uniformity.

5.4.1 Inlet Distortion

Three variations of inlet distortion were applied to the favored high-drag, low-noise 47° vane swirl tube configuration. Described in more detail in Chapter 2, perforated and solid plates created local stagnation pressure deficits in a 120° sector of the nacelle inlet area, simulating circumferential pressure non-uniformities common to curved boundary layer-ingesting inlet ducts. The third case simulated wakes from an upstream blade row, as would be the case for swirl vanes in the engine-integration configuration described in Section 5.3. Ten evenly spaced blade wakes, swept circumferentially, were generated upstream of the swirl vanes.

Figure 5.6 compares the model-scale drag coefficients of the 47° vanes subjected to both uniform and distorted inlet flows. Each of the three inlet distortions presents two competing effects–drag is increased due to the presence of an added physical body in the flow but is also decreased due to the interference with the formation of the drag-generating steady streamwise vortex. In two cases, the 120° perforated plate and blade wake simulator, the net effect is a slight increase in drag over that of the baseline 47° swirl case, suggesting that minor asymmetric and/or symmetric inlet non-uniformities do not significantly impact the creation of the steady streamwise vortex.

Figure 5.7 shows the 17.44 Hz narrowband spectra of the 47° vanes with various inlet distortions compared to the baseline spectrum (blue). It is evident from the figure that both the shape and magnitude of the spectra are relatively unchanged given the introduction of inlet distortion, with the exception of the sharp edge tone detected in the 120° perforated plate case. This tone at 24 kHz is due to the effects of the sharp edges of the holes and is consistent with the spectral tones near 20 kHz observed in the perforated plate spectra from aero-acoustic experiments by Sakaliyski et al. [26]. The perforated plate case is also the only inlet distortion that causes increased noise levels at high frequencies, attributable to the small scale flow structures that drive high-frequency turbulent mixing noise.

Given the small dimensions of the blade wake simulator spokes (2.54 cm, 1 in chord, 3.2 mm, 0.13 in thickness), the wakes of the spokes mix out while traveling the 7.62 cm (3 in) distance between the nacelle inlet and the vane leading edges, reducing the impact of the flow non-uniformity on the development of the streamwise vortex, evident in the drag results. The 120° solid plate, however, is detrimental to the drag of the baseline 47° swirl case, decreasing the drag coefficient by 17 percent to 0.69. In this case, the larger scale and asymmetric distribution of the associated turbulent flow structures impede the development of the steady streamwise vortex, causing the decrease in drag generation. Though the interference with the symmetry of the inlet flow is substantial in this case, the swirl tube is still capable of producing a drag coefficient of ~0.7.

All three distortion cases show increased noise levels below 15 kHz, tracking the spectrum of the baseline case relatively well at higher frequencies. Overall, the noise signature of the 47° vanes is unaltered by upstream distortions. Considering also the minimal effects on drag performance, the swirl tube demonstrates a low sensitivity to inlet distortions.

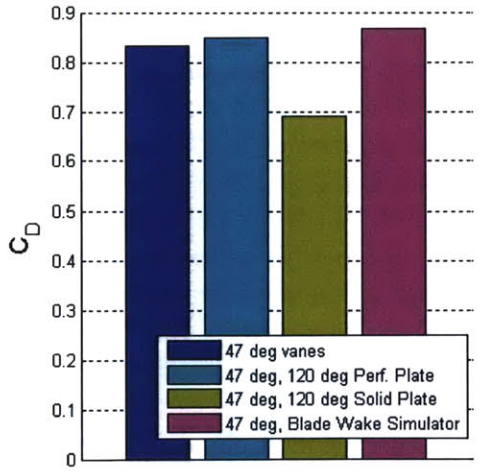

Figure 5.6. Measured drag coefficient of swirl tube with 47° vanes with various inlet distortions. Under the most significant inlet distortion, the 120° solid plate, the swirl tube is still capable of generating a drag coefficient of ~0.7.

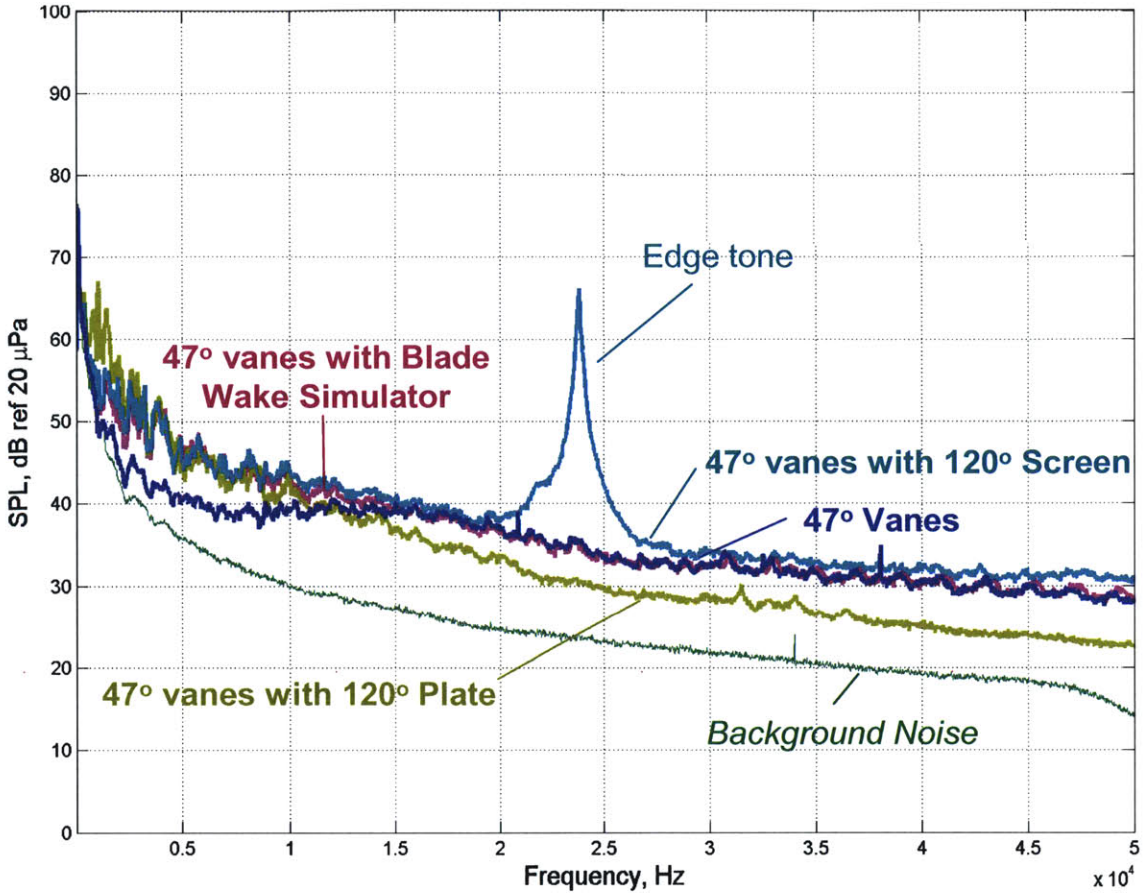

Figure 5.7. Narrowband (17.44 Hz) noise spectra of swirl tube with 47° vanes and various inlet distortions. Overall, baseline case is relatively unaltered by inlet distortion. Strong edge tone in 120° screen case is due to sharp plate hole edges.

5.4.2 Angle of Attack

Similar to the inlet distortion cases described above, small angles of attack cause virtually no change to the acoustic signature of the baseline 47° swirl case. The swirl tube was placed at angle of attack by rotating the pylon screws through arc-shaped slots in the pylon base, designed to provide 10° of rotational freedom with which to angle the swirl tube. The slotted design also provided a means for leveling the swirl tube prior to each test. The leveled 47° swirl case permitted a maximum rotation of approximately 4.5° in either direction, thus setting the angle of attack for the acoustic measurements. Figure 5.8 presents sideline noise spectra for the 47° swirl tube at –4.44°, 0° (baseline) and +4.46° angle of attack, the three curves for which are nearly identical. The –4.44° and +4.46° angled cases yield noise spectra increased and decreased by ~1 dB or less, respectively, as compared to the baseline case. These discrepancies are due solely to the angle of the swirl tube exit, the location of dominant noise sources, relative to the MADA position of the microphone array; –4.44° points the swirl tube aft toward the array while +4.46° points the swirl tube aft away from the array. Again, the unaltered baseline spectrum supports the conclusion that the swirl tube demonstrates a low sensitivity to upstream flow non-uniformities.

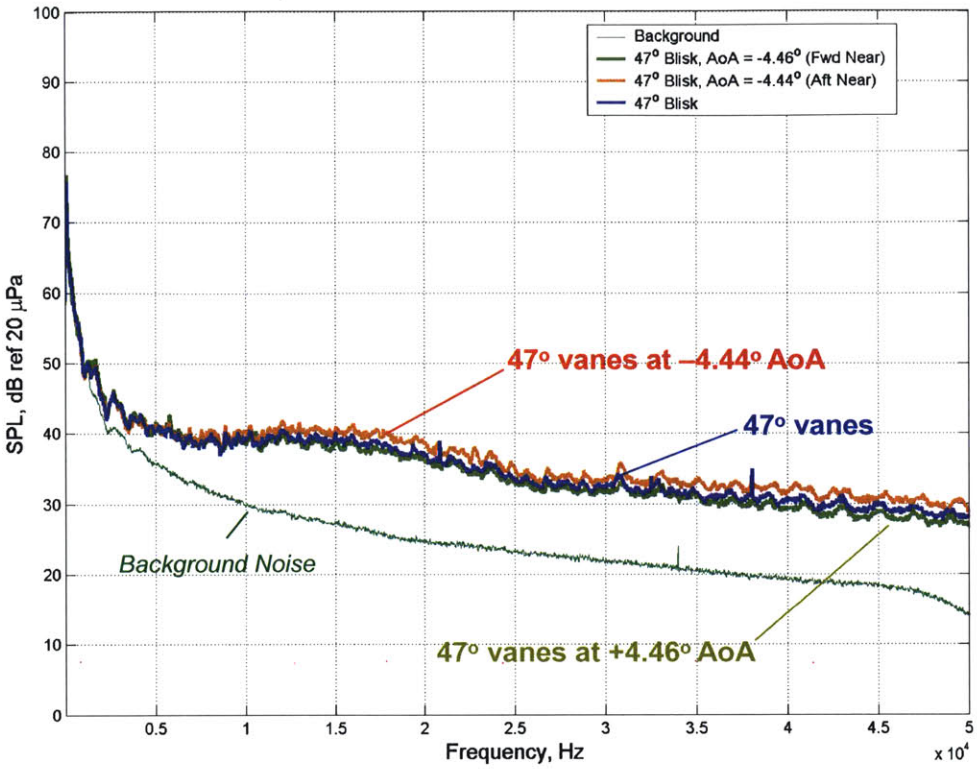

Figure 5.8. Narrowband (17.44 Hz) noise spectra of swirl tube with 47° vanes at small angles of attack. Small angles of attack have little influence on the noise spectrum.

5.5 Quiet Drag Solution

The assessment of swirl tube integration configurations discussed in Sections 5.2 and 5.3 suggest that engine-integrated swirl tubes, so called engine "air brakes", are potentially capable of effectively generating drag with minimal weight cost. The engine air-brake concept takes advantage of fan-stage pumping of flow through the swirl vanes, calculated to yield effective drag coefficients of approximately 3.0. When integrated into current conventional midsize aircraft, full-scale engine air brakes supply drag levels sufficient to increase approach glide slopes to yield a potential aircraft approach noise reduction of over 6.0 dB. The final analysis confirms that swirl tubes are insensitive to non-uniform inlet flows, still capable of generating drag coefficients of ~0.7 with minimal noise penalty under substantial inlet distortion conditions. This assessment indicates that the device might be applied to real-world flight conditions.

Chapter 6

Conclusions and Recommendations for Future Work

6.1 Summary and Conclusions

The research discussed in this thesis demonstrated that swirling exhaust flows provide a low-noise means of generating high levels of drag for quiet drag applications. A model scale test device was designed on a modular basis and implemented to experimentally assess the aerodynamic and aero-acoustic behavior of stable swirling flows and flows with vortex breakdown. The noise mechanisms of these flows were identified and characterized, verifying that the scattering noise of the turbulence associated with vortex breakdown of swirl vane angle cases exceeding 50° accounts for their distinctly higher noise signature. Investigations for practical integration of the low-noise, high-drag stable swirling flows for current and future aircraft design suggested potential performance benefits of engine air brakes, corroborating that swirling exhaust flows are capable of generating drag for quiet transport aircraft.

A modular design was chosen for the 1:7 scale wind-tunnel test model such that the wind-tunnel testing of different swirl angles required changing of a single device component. Turning vanes at swirl angles ranging from 0° to 64° were fabricated to include both stable swirling configurations and cases exhibiting vortex breakdown, the latter of which was predicted to occur at swirl angles exceeding 50°. The scale model was also designed for testing in two wind-tunnel test facilities, the WBWT and QFF. This required appropriate sizing of the swirl tube model relative to the test facility dimensions as well as the design of structural members such as pylons necessary to support the model during testing. Proper selection of test model materials coupled with a structural analysis of the model under critical loading conditions factored into the mechanical design to remove any risk of structural failure of the swirl tube model in either wind-tunnel facility.

Analyses of both aerodynamic and aero-acoustic test results indicate that highly swirling stable flows obtain maximum drag coefficients greater than 0.8 ± 0.04 with full-scale overall sound pressure level (OASPL) of 42 dBA ± 2 dBA. The upper stability limit for swirl was qualitatively and quantitatively identified to occur between 47° and 53° swirl vane angle settings, as predicted by Shah [29]. Exceeding this stability limit causes vortex breakdown, yielding both a decrease in drag generation and a sharp increase in noise level due to additional scattering noise of the burst vortex. DAMAS processing, an advanced beamforming technique developed at the QFF, made accurate noise source location and quantification possible. Using this method, quadrupole- and turbulent scattering-type noise sources were identified in stable swirling flow cases, radiating from the downstream exhaust core and nacelle trailing edge regions, respectively. The spatial distribution of these noise mechanisms coupled with the relatively low Mach number of the flow account for the quiet noise signature of stable swirling flows. Scaling of stable swirl case acoustic spectra confirmed that the core flow Mach number, which increases with swirl angle and free stream velocity, govern the noise level of trailing edge scattering. Vortex breakdown cases (swirl angle > 50°) demonstrate distinctly different noise signatures, found to be 10 to 15 dB louder than stable swirling cases at all frequencies. This is attributable to the increased efficiency with which the burst vortex radiates near the rear nacelle surfaces and edges. A key outcome of the aero-acoustic analysis of swirling flows is the design implication that vortex breakdown phenomena should be avoided for quiet drag devices.

The final research focus regarded practical integration of swirl tubes into aircraft design to meet specific approach drag and noise requirements. The conceptual silent aircraft design SAX-40 provided the basis of assessing three installation configuration concepts: centerbody-mounted, winglet-mounted, and engine-integrated swirl tubes. Of the three concepts, the engine-integrated swirl vanes were most capable in generating effective drag at minimal weight cost while presenting the possibility for integration into the engine thrust reverser package. The increased mass flow through the device from upstream pumping is shown in [29] to yield an effective drag coefficient of ~3 based on a fan pressure ratio of 1.08 for next generation high-bypass ratio engines. Applying the swirl tube concept to conventional midsize aircraft demonstrates the potential for a 6+ dB overall reduction in approach noise. Finally, swirl tube performance was shown to be insensitive to the effects of non-uniform inlet flow. The swirl tube is capable of generating drag coefficients greater than 0.7 with significant inlet distortion with minimal noise penalty, further validating the swirl tube concept for quiet drag applications.

6.2 Recommendations for Future Work

The focus of this research was the assessment of the simplest concept of a drag-generating swirling exhaust flow, the swirl tube. To further investigate the swirl tube as a practical quiet drag solution, it is recommended that future research integrate feasible aircraft installation considerations into next generation swirl tube design. More precisely, further research should be conducted to experimentally assess the behavior of pumped swirl tube performance and to evaluate practical vane designs for aircraft engine integration.

More specifically, the analysis of engine-integrated swirl tube configurations in Chapter 5 described the large increases in thrust reduction generated by swirl vanes pumped by an

upstream fan stage. Though these drag generation capabilities should also be experimentally verified, it is critical that the acoustic behavior of pumped swirl vanes be experimentally assessed, given the complexity and challenge involved in current computations and theoretical approaches. In Chapter 5, assumptions based on core Mach number were made to give a preliminary estimate of pumped swirl noise levels. Aero-acoustic wind-tunnel tests of pumped swirl tubes would be able to establish how upstream pumping changes the noise mechanisms characteristic of unpumped swirl cases, more accurately determining the feasibility of engine-integrated swirl tubes.

The viability of engine-integrated and winglet-mounted swirl tube installation concepts both rely on swirl vane actuation from straight to angled or the complete stowage of turning vanes within nacelle walls for swirl and non-swirl modes. This presents a mechanical challenge given the highly complex geometries of turning vanes designed for the series of experiments described in this thesis. The turning vanes, shown in figures of Chapters 2 and 3, are twisted from hub to tip such that the root sections are symmetric and straight while outer sections are highly cambered. For easy actuation from straight to angled positions or complete stowage, the vanes must be essentially flat, perhaps with a hinged rear chord section for turning angle variation, similar to a vertical tail and rudder on conventional aircraft. While this type of simplified vane design would be far more appropriate for aircraft integration concepts, it is uncertain how such a design would affect the swirl tube drag and noise performance. It is thus recommended that next-generation swirl vane designs take into account aircraft integration operability concerns.

Finally, though the analyses in Chapter 5 suggest that engine-integrated swirl vanes, so-called engine air brakes, are the best means of aircraft integration, it is uncertain if the presence of swirl vanes will adversely effect engine performance. For example, deployment of the swirl vanes into swirl mode could induce back pressuring of the upstream fan stage, potentially reducing the stable operating range of the fan. Experimental quantification of these effects as well as the performance and installation concerns expressed above would provide the next step toward actual aircraft integration of the swirl tube.

Appendix A

Approximation of Turning Vane Load Distribution

Section 3.5.2.1 details the nominal stress and inducted stress concentration analysis of the turning vanes and their junctions with the outer shroud at the vane tips and centerbody at the vane hubs. For simplicity, the load distributions per turning vane, q, due to swirl moment M_S are assumed constant across the vane spans, equal to a load value greater than the maximum of the actual load distribution, q_{act}. This appendix describes the calculations used to obtain the approximated constant load distribution on the turning vanes, q.

The actual load distribution, q_{act}, is determined by first considering a circumferential element of infinitesimal thickness, shown local to a single turning vane in Figure A.1. Tangential vane loading causes the load on the infinitesimal element due to the change in angular momentum imparted on flow passing through the turning vanes. This change in angular momentum $d\tau$ is given by

$$d\tau = \frac{(rv_\theta)d\dot{m}}{n} = \frac{(rv_\theta)(\rho v_x)dA}{n}, \tag{A.1}$$

where n is the number of vanes. The area of the circumferential element is $dA = 2\pi r dr$, thus

$$d\tau = (rv_\theta)(\rho v_x)\frac{2\pi r}{n}dr. \tag{A.2}$$

The local tangential blade force, dF_θ, is defined as the change in angular momentum divided by the moment arm, r,

$$dF_\theta = \frac{d\tau}{r} = v_\theta (\rho v_x) \frac{2\pi r}{n} dr . \tag{A.3}$$

Using this expression for the local tangential blade force, the actual load distribution per vane, q_{act}, is given as

$$q_{act} = \frac{dF_\theta}{dr} = \frac{2\pi r}{n} \rho v_x v_\theta . \tag{A.4}$$

This actual load distribution can be normalized with the same quantities used normalize the expression for swirl moment, M_S, in Section 3.5.1. These quantities, taken from results from Shah's 2-D streamline curvature analysis of a high swirl case [29] include normalized axial and tangential velocity radial profiles, v_z/v_∞ and v_θ/v_∞ as well as the normalized radial distance, r/R, and normalized local density radial profile, ρ/ρ_∞. Again, it is important to include the density radial profile given the presence of compressibility effects in the core region ($r \sim 0$). Similar to the approximation of swirl moment, M_S, the product of these normalized quantities can be plotted to show that the normalized loading distribution on each vane has an upper bound at 0.52 (see Figure 3.10). Thus q, the constant load distribution per vane approximated by taking the maximum value of the normalized actual load distribution, is calculated as

$$q = 0.52 \left(\frac{2\pi R}{n} \rho_\infty v_\infty^2 \right) = 93.8 \text{ N/m} \, (6.43 \text{ lb/ft}) . \tag{A.5}$$

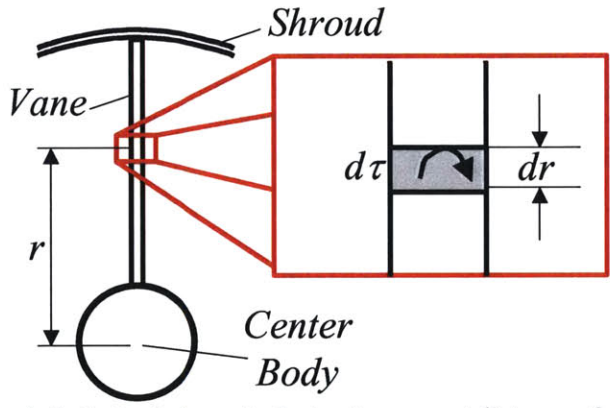

Figure A.1. Loading on an infinitesimal element of a turning vane at distance r from the swirl tube axis of symmetry. Loading is caused by the change in angular momentum of flow through the vane passages due to turning.

Appendix B

Sizing of Fillet Radii for Local Stress Concentrations

As discussed in Sections 3.5.2.1 and 3.5.2.3, fillets were sized to accommodate the high stress concentrations at the sharp corners of the turning vane-shroud junctions and at the base of the pylon tab, respectively. The empirical method for estimating appropriate fillet radii, described in this appendix, is borrowed from *Roark's Formulas for Stress and Strain* [32].

The governing empirically derived equation for the stress concentration factor is based on three geometric parameters of the structure. Figure B.1 defines these geometric parameters: D is the width/diameter of the main structural body, h is the distance between the appendage edge and the tangent of the main body that is parallel to this edge, and r_{fillet} is the fillet radius.

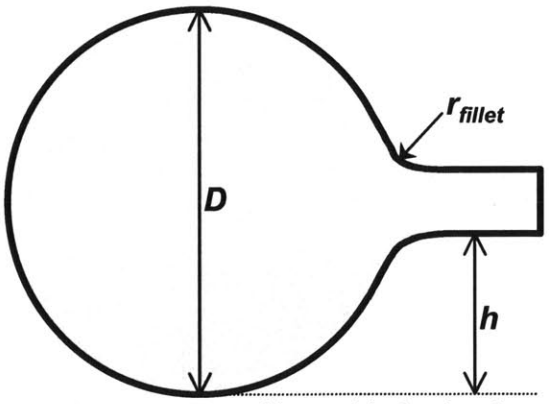

Figure B.1. Definition of geometric parameters used in empirical estimation of fillet sizing for local stress concentrations. Note: figure is not to scale.

Using these geometric parameters, the governing equation for the stress concentration factor due to bending is a third order polynomial of the form

$$K = K_1 + K_2\left(\frac{2h}{D}\right) + K_3\left(\frac{2h}{D}\right)^2 + K_4\left(\frac{2h}{D}\right)^3, \tag{B.1}$$

where K_1, K_2, K_3, and K_4 are empirically defined constants. For a structure with $2.0 \le h/r \le 20.0$, as is the case for both the turning vane-shroud and pylon tab geometries, these constants are defined as

$$K_1 = 1.042 + 0.982\sqrt{\frac{h}{r}} - 0.036\frac{h}{r}, \tag{B.2}$$

$$K_2 = -3.599 + 1.619\sqrt{\frac{h}{r}} - 0.431\frac{h}{r}, \tag{B.3}$$

$$K_3 = 6.084 - 5.607\sqrt{\frac{h}{r}} + 1.158\frac{h}{r}, \tag{B.4}$$

and

$$K_4 = -2.527 + 3.006\sqrt{\frac{h}{r}} - 0.691\frac{h}{r}. \tag{B.5}$$

A fillet radius is sized sufficiently if the consequent stress concentration factor, K, given by equation B.1, is less than the maximum stress concentration factor, K_{max}, defined originally in Equation 3.12 and restated here for convenience.

$$K_{\max} = \frac{\sigma_{yield}}{\sigma_{nominal}} \tag{B.6}$$

Bibliography

[1] Andreou, C., W. R. Graham, and H.-C. Shin. Aeroacoustic Study of Airfoil Leading Edge High-Lift Devices. *AIAA-2006-2515, 12th AIAA/CEAS Aeroacoustics Conference, Cambridge, Massachusetts, USA, May 8-10*, 2006.

[2] Brooks, T. F. and M. A. Marcolini. Airfoil Tip Vortex Formation Noise. *AIAA Journal*, 1986.

[3] Brooks, T. F. and W. M. Humphreys Jr. A Deconvolution Approach for the Mapping of Acoustic Sources (DAMAS) Determined from Phased Microphone Arrays. *Journal of Sound and Vibration*, 2006.

[4] Brooks, T. F. and W. M. Humphreys Jr. Flap-Edge Aeroacoustic Measurements and Predictions. *Journal of Sound and Vibration*, 2003.

[5] Brooks, T. F., D. S. Pope, and M. A. Marcolini. Airfoil Self-Noise and Prediction. Reference Publication 1218, NASA, Hampton, VA, 1989.

[6] Brüel and Kjær. 1/8" Pressure-field Microphone – Type 4138. Product Data Sheet. *http://www.bksv.com*, January 2007.

[7] Dantec Dynamics. Single-sensor Miniature Wire Probes. Product Technical Data Page. *http://www.dantecdynamics.com/Default.aspx?ID=754*, January 2007.

[8] Drela, M. A User's Guide to MTFLOW 1.2 – Multi-passage throughFLOW Design/Analysis Program. November 1997.

[9] Ffowcs Williams, J. E. and L. H. Hall. Aerodynamic Sound Generation by Turbulent Flow in the Vicinity of a Scattering Half Plane. *Journal of Fluid Mechanics, Volume 40, Part 4, pp. 657-670*, 1970.

[10] Gere, J. *Mechanics of Materials*. Brooks/Cole Publishing Company, Pacific Grove, CA, 2001.

[11] Goldstein, M. E. *Aeroacoustics*. McGraw-Hill, New York, NY, 1976.

[12] Goold, Ian. Technology Reshaping Aviation Partners' Winglets. *EBACE Convention News, Aviation International News, May 3*, 2006.

[13] Greitzer, E. M., C. S. Tan, and M. B. Graf. *Internal Flow Concepts and Applications*. Cambridge University Press, Cambridge, UK, 2004.

[14] Hileman, J. Airfoil Self-Noise Prediction. Silent Aircraft Initiative, March, 7, 2005.

[15] Hileman, J., Z. Spakovszky, M. Drela, and M. Sargeant. Airframe Design for "Silent Aircraft". *AIAA-2007-0453, 45th AIAA Aerospace Sciences Meeting and Exhibit, Reno, Nevada, January,* 2007.

[16] Howe, M. S. Noise Produced by a Sawtooth Trailing Edge. The Journal of the Acoustical Society of America, Volume 90, Issue 1, July 1991.

[17] Hutcheson, F. V. and T. F. Brooks. Noise Radiation from Single and Multiple Rod Configurations. *AIAA-2006-2629, 12th AIAA/CEAS Aeroacoustics Conference, Cambridge, Massachusetts, USA. May 8-10,* 2006.

[18] Information for Use by Industry. Wright Brothers Wind Tunnel Information Booklet. MIT, July 2002.

[19] Lighthill, M. J. On Sound Generated Aerodynamically I. General Theory. *Proceedings of the Royal Society of London A*, 1952.

[20] Lighthill, M. J. On Sound Generated Aerodynamically II. Turbulence as a Source of Sound. *Proceedings of the Royal Society of London A*, 1953.

[21] Lockard, D. P. and G. M. Lilley. The Airframe Noise Reduction Challenge. Reference Publication 213013, NASA, Hampton, VA, 2004.

[22] Meadows, K. R., T. F. Brooks, W. M. Humphreys Jr., W. W. Hunter, and C. H. Gerhold. Aeroacoustic Measurements of a Wing-Flap Configuration. *AIAA-1997-1595, 3rd AIAA/CEAS Aeroacoustics Conference, Atlanta, Georgia, USA, May,* 1997.

[23] Mendoza, J. M., T. F. Brooks, and W. M. Humphreys Jr. Aeroacoustics Measurements of a Leading Edge Slat Configuration. *International Journal of Aeroacoustics*, 1(3):241-274, 2002.

[24] Mendoza, J. M., T. F. Brooks, and W. M. Humphreys Jr. Aeroacoustics Measurements of a Wing-Slat Model. *AIAA-2002-2604, 8th AIAA/CEAS Aeroacoustics Conference, Breckenridge, Colorado, USA, June 17-19,* 2002.

[25] Raymer, D. P. *Aircraft Design: A Conceptual Approach.* AIAA Educational Series, Reston, VA, 1999.

[26] Sakaliyski, K. D., J. I. Hileman, and Z. S. Spakovszky. Aero-Acoustics of Perforated Drag Plates for Quiet Transport Aircraft. *AIAA-2007-1032, 45th AIAA Aerospace Sciences Meeting and Exhibit, Reno, Nevada, January,* 2007.

[27] Schlichting, A. H. *Boundary Layer Theory.* McGraw Hill, New York, 1987.

[28] Shah, P., D. Mobed, and Z. Spakovszky. Engine Air-Brakes for Quiet Air Transport. *AIAA-2007-1033, 45th AIAA Aerospace Sciences Meeting and Exhibit, Reno, Nevada, January,* 2007.

[29] Shah, P. Novel Turbomachinery Concepts for Highly Integrated Airframe/Propulsion System. Doctoral Thesis, MIT, February, 2007.

[30] Solecki, R. and R. J. Conant. *Advanced Mechanics of Materials.* Oxford University Press, USA, 2003.

[31] Webster, C. A. G. A Note on the Sensitivity of Yaw of a Hotwire Anemometer. *Journal of Fluid Mechanics, Volume 13, pp. 307-312*, 1962.

[32] Young, W. C. *Roark's Formulas for Stress and Strain.* McGraw-Hill, New York, 1989.